UNIVERSITÀ
DEGLI STUDI
DI PADOVA

Sede Amministrativa: Università degli Studi di Padova

Dipartimento di Neuroscienze

CORSO DI DOTTORATO DI RICERCA IN: Medicina Specialistica Traslazionale “G. B. Morgagni”
CURRICOLO: Neuroscienze Cliniche e Traslazionali
CICLO XXXVI

Mouse models for the study of mitochondrial disorders

Coordinatore: Ch.mo Prof. Dario Gregori
Supervisore: Prof. Elena Pegoraro
Co-Supervisore: Prof. Carlo Viscomi

Dottorando: Dott. Raffaele Cerutti

Contents

Summary of the thesis

Leigh syndrome (LS), or subacute necrotizing encephalomyelopathy, is the most common mitochondrial disease in infancy. Both neurological signs and pathological lesions of Leigh disease are mimicked by the ablation of the mouse mitochondrial respiratory chain subunit NDUFS4, which is crucial for normal CI activity and assembly, particularly in the brain. Currently, no curative therapy for LS is available. In this thesis, I exploited a new, self-complementary adeno-associated viral 9 vector (scAAV9) to deliver the human NDUFS4 gene product in *Ndufs4*$^{-/-}$ mice. Either single intra-vascular (i.v.) or double i.v. and intra-cerebro-ventricular (i.c.v.) injections were performed at post-natal day 1 (P1). The first strategy doubled the lifespan of the *Ndufs4*$^{-/-}$ mice from 45 to ≈100 days after birth, when the mice developed rapidly progressive neurological failure. However, the double i.v. and i.c.v. administration of the scAAV9-h*NDUFS4* prolonged healthy lifespan up to 9 months of age. These mice were well and active at euthanization performed to investigate the brain and other organs post-mortem. Robust expression of hNDUFS4 was detected in different cerebral areas preserving normal morphology and restoring Complex I activity and assembly. These data warrant further investigations to fully assess translatability of the scAAV9-h*NDUFS4*-based therapy to the patients by investigating its effectiveness during the prodromal phase of the disease in mice and eventually humans.

Mutations in the *POLG* gene, coding for POLγA, are a common cause of human disease leading to a spectrum of disorders characterized by mtDNA instability, that compromise the mitochondrial function. Despite being relatively frequent, the molecular pathogenesis of POLG-related diseases is poorly understood, and efficient treatments are missing, partly due to the lack of relevant in vivo models. In the second part of my dissertation, I discuss the *in vivo* and *in vitro* characterization of the POLγA Y933C mutation, which reproduces the Y955C change, the most common human dominant mutation

of *POLG*. The phenotypic characterization of POLG Y933C mice revealed disrupted mendelian distribution of offspring, indicating that the Y933C mutation is lethal when in homozygosity. However, the heterozygous mice did not display exercise intolerance or impaired motor coordination when compared to the WT littermates. Histological analysis of tissues from *Polg*$^{+/Y933C}$ showed no obvious morphological alterations in the brain, kidney, and heart at 5 months of age. However, at 24 months of age, the brain exhibited vacuolation and presence of activated microglial cells, indicating ongoing inflammation and neurodegeneration. Molecular analysis revealed that the Y933C mutation did not cause a significant reduction in mtDNA copy number in any of the tissues analyzed. However, in *vitro* characterization of the mutant recombinant POLγA protein demonstrated severely impaired DNA synthesis for both mouse and human mutant proteins. Moreover, both mouse and human mutant proteins displayed a dominant negative effect on the replisome and could not support DNA synthesis on dsDNA templates.

Riassunto della tesi

La sindrome di Leigh, o encefalomielopatia necrotizzante subacuta, rappresenta la più comune malattia mitocondriale nell'infanzia. I segni neurologici e le lesioni patologiche caratteristiche di questa malattia sono replicate nei topi dall'ablazione della subunità NDUFS4, essenziale per l'assemblaggio e l'attività del complesso I della catena respiratoria mitocondriale, soprattutto nel cervello. Attualmente non esiste una terapia. Nel mio progetto di dottorato, ho utilizzato un vettore virale adeno-associato di tipo 9 autocomplementare (scAAV9) per indurre l'espressione della proteina NDUFS4 umana nei topi *Ndufs4*$^{-/-}$. Il giorno dopo la nascita (P1), è stata eseguita un'iniezione intavascolare (i.v.) o una doppia iniezione intravascolare e intracerebroventricolare (i.c.v.) nei topi. La singola iniezione virale ha esteso la sopravvivenza dei topi *Ndufs4*$^{-/-}$ da 45 giorni a circa 100 giorni dopo la nascita, quando hanno iniziato a sviluppare un'insufficienza neurologica a progressione rapida. Tuttavia, la doppia iniezione i.v. e i.c.v. del vettore virale scAAV9-h*NDUFS4* ha prolungato la sopravvivenza dei topi fino a 9 mesi d'età. Al momento dell'eutanasia, eseguita per analizzare il cervello e gli altri organi, i topi stavano bene ed erano attivi. La proteina NDUFS4 era espressa in diverse aree cerebrali, che mostravano una morfologia normale, e in cui l'assemblaggio e l'attività del Complesso I erano ripristinati. Questi dati incoraggiano ulteriori analisi sulla possibile applicazione della terapia genica basata su scAAV9-h*NDUFS4* nella fase prodromica della malattia e, potenzialmente, negli esseri umani.

Le mutazioni del gene *POLG*, che codifica per POLγA, sono causa comune di malattie caratterizzate da instabilità del DNA mitocondriale. Nonostante siano relativamente frequenti, la patogenesi molecolare delle malattie dovute a *POLG* è poco nota, e mancano trattamenti efficaci, in parte a causa della mancanza di pertinenti modelli *in vivo*. Nella seconda parte della mia tesi discuto la caratterizzazione *in vitro* e *in vivo* della mutazione Y933C in POLγA, che riproduce la mutazione Y955C, la mutazione dominante umana più comune di *POLG*. L'analisi fenotipica dei topi *POLG* Y993C ha rivelato un'alterata distribuzione mendeliana della prole, che indica che la mutazione è embrioletale in omozigosi. I topi eterozigoti non mostrano intolleranza all'esercizio o un'alterata coordinazione motoria rispetto ai fratelli WT. L'analisi istologica dei tessuti dei topi *Polg*$^{+/Y933C}$ non mostra ovvie alterazioni in cervello, rene e cuore a 5 mesi d'età. Tuttavia, a 24 mesi d'età, il cervello mostra vacuolizzazione e presenza di cellule microgliali attivate, indicanti un processo infiammatorio in corso e neurodegenerazione. L'analisi molecolare rivela che la mutazione Y933C non causa deplezione del DNA mitocondriale in nessuno dei tessuti analizzati. L'analisi *in vitro* della proteina POLγA mutante dimostra un'alterata sintesi di DNA su stampi di DNA a singola catena. Inoltre, sia la proteina mutante umana che quella murina, mostrano un effetto dominante negativo sul replisoma e non sono grado di effettuare la sintesi di DNA su stampi a doppia catena.

Abbreviations

2D-AGE	Neutral two-dimensional agarose gel electrophoresis
AAP	Assembly activating protein
AAV	Adeno-associated virus
ADOA	Autosomal dominant optic atrophy
ADP	Adenosine diphosphate
adPEO	Autosomal dominant progressive external ophthalmoplegia
AHS	Alpers-Huttenlocher Syndrome
ANS	Ataxia neuropathy spectrum
arPEO	Autosomal recessive progressive external ophthalmoplegia
ATP	Adenosine triphosphate
BBB	Blood-brain barrier
BNGE	Blue native PAGE
BSA	Bovine serum albumin
CD68	Cluster of differentiation 68
cDNA	Complementary DNA
CI	Mitochondrial complex I
CII	Mitochondrial complex II
CIII	Mitochondrial complex III
CIV	Mitochondrial complex IV
CNS	Central nervous system
CoA	Coenzyme A
CoQ	Coenzyme Q
COX	Cytochrome c oxidase
CPEO	Chronic progressive external ophthalmoplegia
CSBs	Conserved sequence blocks
Ct	Cycle threshold
CV	Mitochondrial complex V
D-loop	Displacement loop
DAB	Diaminobenzidine
dNTPs	Deoxyribonucleotide triphosphates
dsDNA	double-stranded DNA
DTNB	5-dithio-bis-(2)-nitrobenzoic acid
EDTA	Ethylenediaminetetraacetic acid
EE	Ethylmalonic encephalopathy
EMSA	Electrophoretic mobility shift assay
ES	Embryonic stem
ETC	Electron transport chain
FAD	Flavine adenine dinucleotide (oxidized form)
$FADH_2$	Flavine adenine dinucleotide (reduced form)
FBSN	Familial bilateral striatal necrosis

Fe/S	Heme and iron-sulphur (clusters)
FFPE	Formalin-fixed paraffin embedded
Fw	Forward
GFAP	Glial fibrillary acidic protein
gRNA	Guide RNA
H&E	Haematoxylin and eosin
HDR	Homology directed repair
HIER	Heat-induced epitope retrieval
HSP	H-strand promoter
i.c.v.	Intracerebroventricular
i.v.	Intravascular
IGA	In-gel activity
IHC	Immunohistochemistry
IMM	Inner mitochondrial membrane
IMS	Intermembrane space
ITRs	Inverted terminal repeats
KO	Knockout
LHON	Leber's hereditary optic neuropathy
LS	Leigh syndrome
LSP	L-strand promoter
LY6A	Lymphocyte antigen 6 complex, locus A
MCHS	Childhood myocerebrohepatopathy spectrum
MELAS	Mitochondrial encephalomyopathy, lactic acidosis, and stroke-like episodes
MEMSA	Myoclonic epilepsy myopathy sensory ataxia
MERRF	Myoclonus epilepsy and ragged-red fibers
MILS	Maternally inherited Leigh syndrome
MIRAS	Mitochondrial recessive ataxia syndrome
miRNA	MicroRNA
MNGIE	Mitochondrial neuro-gastro-intestinal leukoencephalopathy
MRC	Mitochondrial respiratory chain
mtDNA	Mitochondrial DNA
MTERF1	Mitochondrial termination factor 1
mTOR	Mechanistic target of rapamycin
mTORC1	mTOR complex I
MTS	Mitochondrial targeting sequence
mtSSB	Mitochondrial single-stranded DNA-binding protein
NAD^+	Nicotinamide adenine dinucleotide (oxidized form)
NADH	Nicotinamide adenine dinucleotide (reduced form)
NARP	Neuropathy, ataxia, retinitis pigmentosa
NBF	Neutral buffered formalin
NBT	Nitroblue tetrazolium
NCR	Non-coding region (in the mitochondrial DNA)
nDNA	Nuclear DNA

Ndufs4	NADH dehydrogenase ubiquinone iron-sulphur protein 4
NHPs	Non-human primates
NRTI	Nucleoside reverse transcriptase inhibitor
NTE	N-terminal extension
O.C.T.	Optimal cutting temperature compound
O_H	H-strand replication
O_L	L-strand replication
OMM	Outer mitochondrial membrane
OXPHOS	Oxidative phosphorylation
P1	Postnatal day 1
PBS	Phosphate-buffered saline
PCR	Polymerase chain reaction
PEO	Progressive external ophthalmoplegia
PMF	Proton-motive force
PMS	Phenazine methosulfate
POLRMT	Mitochondrial DNA-dependent RNA polymerase
POLγ	DNA polymerase γ
qPCR	Quantitative PCR
rAAV	Recombinant AAV
ROS	Reactive oxygen species
rRNAs	Ribosomal RNAs
RT	Room temperature
Rv	Reverse
SANDO	Sensory ataxia neuropathy dysarthria and Ophthalmoplegia
scAAV9	self-complementary AAV9
SCAE	spinocerebellar ataxia with epilepsy
SD	Standard deviation
SDH	Succinate dehydrogenase
SDS-PAGE	Sodium Dodecyl Sulfate Polyacrylamide Gel Electrophoresis
SEM	Standard error of mean
SKM	Skeletal muscle
ssAAV9	Single-stranded AAV9
ssDNA	Single-stranded DNA
T-TBS	Tris-buffered saline with tween-20
TAS	Termination-associated sequences
TBE	Tris/borate/EDTA
TCA	Tricarboxylic acid cycle
TEFM	Mitochondrial transcription elongation factor
TFAM	Mitochondrial transcription factor A
TFB2M	Mitochondrial transcription factor B2
TIM	Translocase of the inner membrane
T_m	Melting temperature

TOM	Translocase of the outer membrane
tRNAs	Transfer RNAs
UCP	Uncoupling protein
v/v	volume/volume
VDAC	Voltage-dependent anion channel
vg	Viral genomes
w/v	Weight/volume
WB	Western blot
WES	Whole exome sequencing
WT	Wild-type
$\Delta\psi$m	Mitochondrial membrane potential

Chapter 1

Introduction

1. Introduction

Mitochondria, which are present in nearly all eukaryotic cells, are highly dynamic organelles that play vital roles in energy production, the synthesis of cellular components, and cellular signaling pathways. They primarily generate cellular energy through a process called oxidative phosphorylation (OXPHOS), which is central to ATP production (Wallace, 1999).

Throughout the course of evolution, human mitochondria have retained their unique genome, known as mitochondrial DNA (mtDNA). MtDNA encodes 13 polypeptides that are essential components of the OXPHOS system, along with the 12S and 16S ribosomal RNAs (rRNAs) and 22 transfer RNAs (tRNAs) required for translating these polypeptides. However, considering that mtDNA only codes for 13 out of over 1000 proteins found in mitochondria, most of mitochondrial proteins are encoded by nuclear DNA (nDNA). These nuclear-encoded proteins are actively transported into mitochondria to assemble a functional organelle (Neupert and Herrmann, 2007). This arrangement places mitochondrial homeostasis under the dual genetic control of both nDNA and mtDNA. Consequently, any detrimental mutations occurring in genes responsible for encoding mitochondrial proteins can lead to mitochondrial dysfunction and, consequently, various diseases. This group of disorders is collectively referred to as mitochondrial diseases.

1.1. Mitochondria

1.1.1. Origin of mitochondria

Mitochondria trace their evolutionary origins back to an α-proteobacterium (Yang et al., 1985; Andersson et al., 1998). Around 1.5 to 2 billion years ago, this bacterium formed a symbiotic relationship with an archaeal cell (Sicheritz-Pontén et al., 1998). The traditionally held view, known as the endosymbiotic theory, suggests that an early eukaryotic cell that lacked mitochondria engulfed an α-proteobacterium with the ability to process oxygen. Rather than being digested, this bacterium established a beneficial partnership with its host as the atmosphere became more oxygen-rich (Sagan, 1967; Cavalier-Smith, 1987; Lane and Martin, 2010).

However, recent comparative genomics and geochemical evidence instead suggest that the driving force for eukaryogenesis was in fact the beneficial exchange of hydrogen from an α-proteobacterial facultative anaerobe, which synthesised hydrogen by fermentation and could also respire aerobically in the presence of oxygen, to a hydrogen-dependent archaeal (prokaryotic) host cell. This hydrogen hypothesis offers an explanation for several critical aspects that the conventional endosymbiotic theory fails to address. These aspects include the observation that mitochondria, traditionally believed to have evolved from symbiotic bacteria, actually share the majority of their genes with hydrogenosomes, which are organelles similar to mitochondria that produce hydrogen gas as a byproduct during ATP synthesis in certain anaerobic eukaryotic species (Embley and Martin, 2006).

As time progressed, the engulfed bacterium, which evolved into the mitochondrion, transferred most of its genes to the host's nuclear genome. This genetic integration solidified their interdependent relationship. By doing so, it paved the way for organisms with higher complexity. Yet, by preserving some vital genes, mitochondria can adjust rapidly to the cell's energy needs, essentially behaving as energy regulators. Their ability to do this is linked with the coordinated actions of the proteins encoded by the cell nucleus (Amiott and Jaehning, 2006; Richter-Dennerlein et al., 2016).

1.1.2. Structure and dynamics of mitochondria

Mitochondria have two distinct membranes that serve different functions: the outer mitochondrial membrane (OMM) and the inner mitochondrial membrane (IMM) (Frey and Mannella, 2015). The OMM acts as the outer boundary separating the cytoplasm from the interior of the mitochondria. In contrast, the IMM serves as an inner barrier, surrounding the mitochondrial matrix and featuring numerous inwards folds called cristae. The aqueous region between the OMM and IMM is referred to as the intermembrane space (IMS) (Figure 1.1)

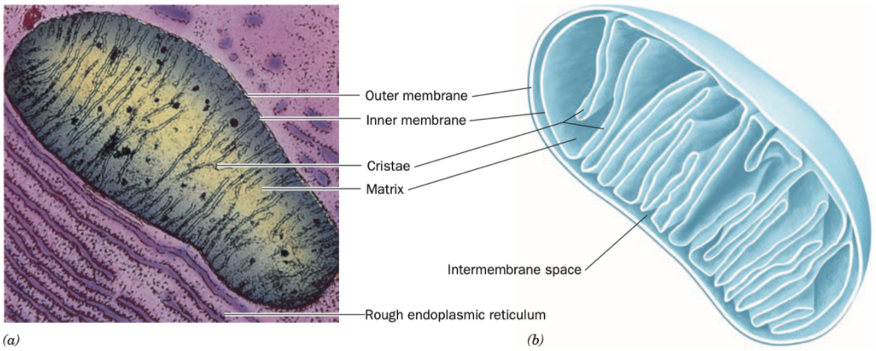

Figure 1.1. Mitochondria. (a) An electron micrograph of an animal mitochondrion. (b) Cutaway diagram of a mitochondrion (image from Voet, Donald, and Judith G. Voet. *Biochemistry*. 4th ed., John Wiley & Sons, 2011).

These two membranes have distinct differences in their permeability properties. The OMM contains numerous voltage-dependent anion channels (VDAC) responsible for forming channels that allow ions and small molecules to enter the mitochondria. Conversely, the IMM acts as a highly effective barrier, only permitting the passage of oxygen, carbon dioxide, and water. Specific substances and reaction products cross the IMM through a complex system of embedded mitochondrial protein carriers (Kunji, 2004). This tight regulation of the IMM permeability is crucial for creating an electrochemical gradient necessary for producing adenosine triphosphate (ATP), the cell energy source (Mitchell, 1961).

The human mitochondrial proteome comprises more than a thousand different proteins. The majority of these proteins are not directly produced within the mitochondria but are instead encoded by the cell nucleus. They are then translated by ribosomes in the cytoplasm and subsequently transported into the mitochondria. This import process is facilitated by a specific sequence called the mitochondrial targeting sequence (MTS) typically located at the protein N-terminus (Neupert and Herrmann, 2007). The MTS consists of a peptide ranging from 10 to 70 amino acids, characterized by a repeating pattern of hydrophobic and positively charged amino acids, which collectively form an amphipathic helix. To become functionally active, in most of the mitochondrial proteins the MTS must be cleaved, a crucial step accomplished by specific peptidases and proteases. This cleavage process plays a vital role in maintaining the balance and proper functioning of mitochondria (Neupert and Herrmann, 2007).

Nuclear-encoded mitochondrial proteins use the translocase of the outer membrane (TOM) complex to cross the OMM. Depending on the characteristics of their MTS, these proteins can be directed to various districts of the mitochondria, including the mitochondrial matrix, the OMM, the IMM, or the IMS. Other translocases and assembly machineries are responsible for this sorting process (Wiedemann et al., 2004). The IMM possesses its own machinery for importing proteins that need to be integrated into the IMM itself or transported into the mitochondrial matrix. Such task is accomplished by two complexes known as translocase of the inner membrane (TIM) complexes: TIM22 and TIM23, respectively (Chacinska et al., 2009).

Mitochondria were initially thought to exist as isolated, rod-shaped structures scattered throughout the cell cytoplasm (Palade 1953; Ernster and Schatz, 1981). However, we now understand that mitochondria form extensive and dynamic networks. The number, size, and mobility of mitochondria within cells vary significantly between different tissues (McCarron et al. 2013). For instance, in skeletal muscle, mitochondria align in rows parallel to the contractile fibers (Vendelin et al. 2005) but in neurons, mitochondria often move along the cytoskeleton, shuttling between dendrites and synapses in response to changing energy demands related to nerve transmission (Barnhart and Erin, 2016). The shape, size, and quantity of mitochondria in a cell are influenced by the processes of fusion and fission (Koshiba et al. 2004). Eukaryotic cells cannot generate new mitochondria from scratch, so their proliferation relies on pre-existing mitochondria through fission. The delicate balance between fusion and fission is regulated by a specialized family of dynamin-like GTPases (Hoppins et al., 2007). These GTPases favor one process over the other based on the cell energy requirements and specific signals. Fusion enables the mixing of mitochondrial DNA, proteins, or metabolites when resources are limited, often associated with defense mechanisms that enhance cell survival. On the other hand, fission is typically linked to mitochondrial dysfunction and cell death but also play a crucial role in normal cellular processes such as distributing and trafficking mitochondria or isolating impaired ones within the network. These damaged mitochondria are marked for degradation through selective autophagy, a processed known as mitophagy (Narendra et al., 2008).

1.1.3. Roles of mitochondria in cellular bioenergetics

In the mid-20th century research in bioenergetics highlighted the pivotal role of mitochondria in cellular energy production (Pagliarini and Rutter, 2013). This seminal work led to the now-familiar description of mitochondria as the cell's "energy hubs" (Siekevitz, 1957).

Mitochondria are responsible for the generation of more than 90% of the cell energy, primarily in the form of ATP. This energy release, essential for nearly all cellular functions, happens when an ATP molecule is de-phosphorylated to ADP. For the cell to function continually, ATP regeneration is crucial, and it arises from nutrient management in a process termed cellular respiration. This intricate metabolic pathway begins with glucose breaking down into carbon dioxide. In this phase, the final electron acceptor, oxygen, becomes reduced to water (Schell and Rutter, 2013). Prior to entering the mitochondria for respiration, glucose undergoes an initial set of anaerobic reactions in the cytoplasm, termed glycolysis. Here, glucose is oxidized to pyruvate, yielding 2 ATP molecules per glucose unit. To increase ATP yield, glycolysis is coupled with the tricarboxylic acid (TCA) or Krebs cycle. Within the mitochondria, glycolysis-derived pyruvate contributes its acetyl groups to Coenzyme A, resulting in acetyl-CoA and NADH generation. Acetyl-CoA then partakes in the TCA cycle, undergoing various enzymatic reactions to extract reducing equivalents from substrates. This translates into the reduction of cofactors NAD^+ and FAD to their respective reduced forms. The culmination of cellular respiration involves the electron transport chain (ETC) in the IMM. Here, electrons from NADH and $FADH_2$ power redox reactions, providing energy for the synthesis of ATP through oxidative phosphorylation (OXPHOS) (Figure 1.2). The ETC, comprising four protein complexes (Complex I (CI), NADH:ubiquinone oxidoreductase; Complex II (CII), succinate:ubiquinone oxidoreductase; Complex III (CIII), ubiquinone:cytochrome c oxidoreductase; and Complex IV (CIV or COX), cytochrome c oxidase), orchestrates the sequential electron transfer, ultimately yielding water by reducing oxygen (Saraste, 1999). NADH introduces electrons into the ETC at CI, while $FADH_2$ is associated with CII. Both CI and CII utilize these electrons to convert ubiquinone to its reduced form, ubiquinol (referred to as coenzyme QH_2). QH_2, soluble in the IMM, moves to CIII. Here, the electrons are transferred to another mobile electron-carrier, the cytochrome c. Subsequently, cytochrome c shuttles these electrons to CIV, culminating in their final transfer to oxygen, which results in the formation of water. As electrons are efficiently transferred through the ETC complexes, protons are actively pumped from the IMM into the IMS. This action results in the establishment of a proton-motive force (PMF). This force arises from two primary components: a gradient of proton concentration between the IMS and the mitochondrial matrix (ΔpH) and a disparity in electrical charges on either side of the IMM, referred to as the mitochondrial membrane potential ($\Delta\psi$m) (Mitchell, 1972, Dzbek and Korzeniewski, 2008). The PMF is exploited by Complex V or ATP synthase to generate ATP by phosphorylating ADP, through the energy provided by the backflow of protons from the IMS to the mitochondrial matrix (Walker, 2013). After its production, the ATP located within the mitochondrial matrix can be shuttled into the IMS via the dedicated ADP/ATP carrier (Kunji et al., 2016). Upon reaching the IMS, ATP can freely cross the OMM through VDAC, facilitating its distribution throughout the cell (Bonora et al., 2012).

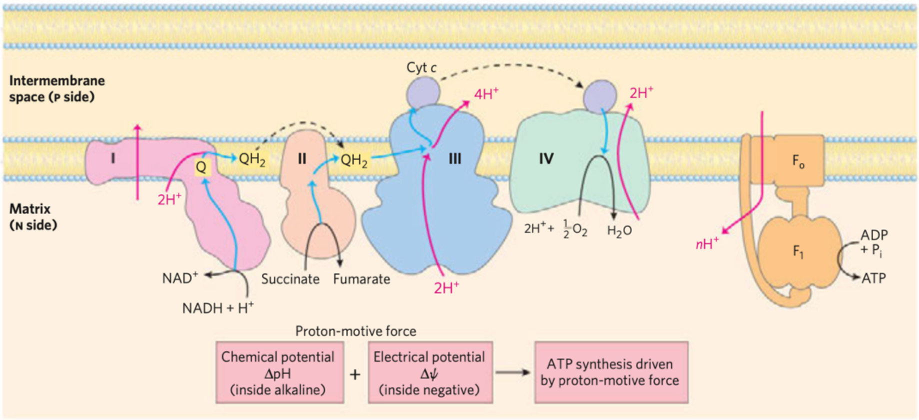

Figure 1.2. Bioenergetics of the electron transport chain. Electrons from NADH and $FADH_2$ pass through a chain of carriers in the inner mitochondrial membrane (IMM). Electron flow is accompanied by proton transfer across the membrane, producing both a chemical gradient (ΔpH) and an electrical gradient ($\Delta\psi$m) (combined, the proton-motive force). The inner mitochondrial membrane is permeable to protons; protons can reenter the matrix only through proton-specific channels (F_0). The proton-motive force that drives proton back into the matrix provides the energy for ATP synthesis, catalysed by Complex V. (image from Nelson, David L., and Michael M. Cox. *Lehninger Principles of Biochemistry*. 6th ed., W. H. Freeman, 2013).

1.1.4. Other mitochondrial functions

Mitochondria, traditionally associated to their primary role in energy synthesis, have been implicated in a multitude of metabolic and regulatory processes. One of the notable functions is non-shivering thermogenesis, a form of heat generation not linked to muscle tremors (Cannon and Nedergaard, 2004). This heat production arises from proton movements in the IMS of mitochondria that bypass the ATP synthase mechanism, a phenomenon termed as proton leak. The uncoupling proteins (UCPs) facilitate this process, which is particularly evident in brown adipose tissues of newborns and hibernating animals (Brand and Esteves, 2005, Brooks and Watson, 2012).

Furthermore, mitochondria are pivotal hubs for heme synthesis and iron-sulfur (Fe/S) cluster formation, as well as the generation and control of reactive oxygen species (ROS). Heme, an iron-bound porphyrin, plays an integral role not only in the electron transport chain but also in a range of cellular activities including oxygen transport and storage, signal transduction, and miRNA processing (Chiabrando et al., 2014). Fe/S clusters serve as versatile redox units crucial for the functionality of diverse enzymes and are indispensable for the correct function of the electron transport chain complexes CI, CII, and CIII (Rouault, 2015).

Interestingly, ROS, primarily produced due to electron leak in the electron transport chain, possess a dual role. While excessive ROS can damage DNA, proteins, and lipids, they are integral part to certain biological processes, including senescence (Finkel and Holbrook, 2000). ROS play an instrumental role in signaling pathways that govern various physiological functions. Hence, maintaining a balance in ROS levels is paramount, as both its deficiency and abundance can jeopardize cellular health (Dröge, 2002).

Lastly, mitochondria are at the heart of the apoptotic pathway, a process of programmed cell death (Green and Reed, 1998). Essential for embryogenesis and numerous physiological functions, apoptosis can be induced by a myriad of factors such as persistent DNA damage and oxidative stress (Hengartner, 2000). Central to this mechanism is the mitochondrial outer membrane permeabilization (MOMP), culminating in the release of cytochrome c from the IMM to the cytosol. Once in the cytosol, cytochrome c initiates the apoptosome assembly, activating caspases which then orchestrate cellular self-destruction (Kroemer et al., 2007).

1.2. Preservation and functionality of the mitochondrial genome

Throughout evolution, a significant proportion of genes originating from the primordial mitochondrial ancestor migrated to the host nuclear genome (nDNA), leading to the loss of mitochondrial autonomy. This further strengthened the mutualistic relationship between the mitochondria and the host (Ku et al., 2015). A subset of these relocated genes plays a pivotal role in ensuring mitochondrial stability. Concurrently, remnants of these genes exist in the nDNA as mitochondrial pseudogenes, known as nuclear mitochondrial DNA. Despite this extensive migration of genes, mitochondria have retained a compact yet crucial set of genes within the mitochondrial DNA (mtDNA) vital for ATP generation and protein synthesis.

The exact rationale for the mitochondria conservation of this distinct genome remains an area of active inquiry. One prevailing theory suggests that the proteins encoded by the mtDNA are highly hydrophobic in nature, making their import into the mitochondria challenging. Hence, evolutionary pressures may have favored the in-situ production of these proteins to bypass potential transport difficulties (Allen, 2015). An alternative view suggests that proteins encoded on the mtDNA serve to fine-tune the electron flow within the respiratory chain. By encoding key components of each complex in the ETC within the mtDNA, individual mitochondria can promptly adjust to metabolic demands by modulating protein synthesis, negating potential lags if these proteins were encoded in the nDNA (Allen, 2017). Lastly, the mtDNA genetic code has subtle deviations from that of nDNA, especially in the codons for amino acids like methionine and tryptophan and the inclusion of only two stop codons. Such differences might have established a barrier, preventing further gene migration from the mitochondria to the nucleus (Osawa et al., 1992). However, in contrast to animals and fungi, plants have retained the universal code also for mtDNA.

1.2.1. Organization of the mitochondrial genome

Mammalian mtDNA is a circular, double-stranded DNA molecule that exists in multiple copies. It encodes 13 crucial protein subunits of the respiratory chain complexes: seven for CI, one for CIII, three for CIV, and two for CV. Additionally, this mtDNA comprises 22 tRNAs and two ribosomal RNAs (rRNAs) needed for translation (Taanman, 1999) (Figure 1.3). Notably, CII is the only respiratory protein complex entirely encoded by nDNA.

The mtDNA is remarkably concise, devoid of introns, and other non-coding DNA tracts with the exception of an approximately 1 kb non-coding region (NCR), which contains the origin of replication of one mtDNA strand (the heavy strand, see below) and the origin of transcription of both strands. Otherwise, each gene is closely followed by another. Notably, two sets of protein-coding regions even overlap: ND4/ND4L and ATP6/ATP8. The two strands, distinguished as the heavy (H) or light (L) strand, differ in their G+T content, leading to variations in density in alkaline CsCl gradients, owing to the ionization of G and T in alkaline conditions (Doda et al., 1981).

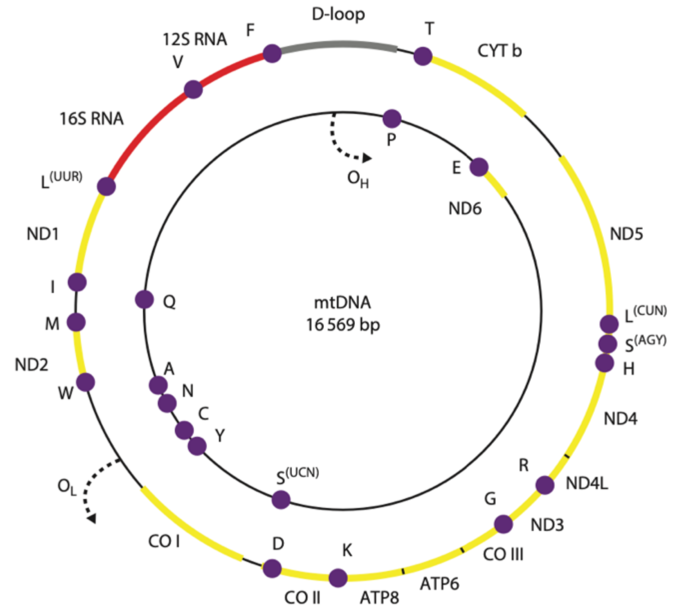

Figure 1.3. The human mitochondrial genome. The human mitochondrial genome (mtDNA) is a small 16,569-kb molecule of double-stranded DNA. MtDNA encodes for 13 essential components of the respiratory chain. ND1-ND6 and ND4L encode seven subunits of complex I (NADH-ubiquinone oxidoreductase). Cyt b is the only mtDNA complex III subunit (ubiquinol-cytochrome c oxidase reductase). COX I to III encode for three of the complex IV (cytochrome c oxidase, or COX) subunits, and the ATP 6 and ATP 8 genes encode for two subunits of complex V (ATP synthase). Two ribosomal RNA genes (12S and 16S rRNA) and 22 transfer RNA genes are interspaced between the protein-coding genes. These provide the necessary RNA components for intramitochondrial protein synthesis. O_H and O_L are the origins of heavy– and light-strand mtDNA replication (image from Love, Seth, et al. *Greenfield's Neuropathology*. 9th ed., vol. 1-2, CRC Press, Taylor & Francis Group, 2015).

Within the NCR lie the promoters essential for transcribing both strands of mtDNA: the H-strand promoter (HSP) and the L-strand promoter (LSP). Also, the NCR encompasses crucial sequences controlling mtDNA replication, such as the origin of H-strand replication (O_H). Another replication origin devoted to L-strand synthesis (O_L) is located around 11 kb from O_H, dividing the mtDNA into two sections termed as the major arc and minor arc (Nicholls and Minczuk, 2014). The NCR further includes three "conserved sequence block" (CSBs), identified from sequence comparison across various vertebrates (Walberg and Clayton, 1981, Saccone et al., 1999). Moreover, an element post O_H, termed termination-associated sequences (TAS), is present in the NCR. Another intriguing structure within the NCR is the displacement-loop (D-loop), a specialized segment resulting from the synthesis of a third DNA strand. This formation displaces the typical double-stranded DNA, leading to this unique D-loop structure (Nicholls and Minczuk, 2014).

Out of the plethora of proteins housed within the mitochondria, numbering over 1000, mtDNA encodes for a mere 13 polypeptides. Consequently, the vast majority, encompassing components of the respiratory chain and proteins pivotal for proper mitochondrial physiology, are products of nuclear gene translation occurring on cytosolic ribosomes (Wallace, 1999). Post synthesis, these proteins are delivered to the mitochondria via specialized import machinery. Noteworthy among these are proteins instrumental for mtDNA replication and transcription, topics comprehensively discussed in the following sections.

1.2.2. Transcription of mtDNA

The transcription process in mammalian mitochondria begins at two distinct sites, HSP and LSP, both situated in the NCR, resulting in the formation of two polycistronic RNAs (Falkenberg et al., 2007). The transcription activity from LSP gives rise to mRNA for the CI subunit ND6 and eight distinct tRNAs. On the other hand, the HSP-driven transcription leads to the genesis of the other ten mRNAs, corresponding to 12 protein products, alongside 14 tRNAs and the two rRNAs. After being produced, these extensive polycistronic RNAs are cleaved and processed into individual mRNAs, which then participate in translation via the mitochondrial ribosomal machinery (D'Souza and Minczuk, 2018).

The intricate process of mtDNA transcription is orchestrated by a monomeric, DNA-dependent RNA polymerase, termed POLRMT (Gustafsson et al., 2016). While POLRMT can specifically bind to promoter sequences, it cannot begin transcription independently. Instead, it necessitates the synergistic involvement of the mitochondrial transcription factor A (TFAM) and mitochondrial transcription factor B2 (TFB2M) for initiation (Gustafsson et al., 2016).

The transcription initiation phase is induced by the TFAM specific affinity to the promoter region, inducing a pronounced U-bend in the mtDNA structure. Following this, through synergistic binding with TFAM, POLRMT is recruited to the promoter, leading to the formation of a closed preinitiation complex. The sequential recruitment of TFB2M elicits architectural alterations in POLRMT, facilitating the DNA strand unwinding and establishing an open initiation complex, where RNA synthesis can start (Gustafsson et al., 2016) (Figure 1.4). The transition from the initial stage of transcription to the elongation phase in mitochondrial transcription involves a specific sequence of events. This process includes the release of TFB2M and the recruitment of a factor called the mitochondrial transcription elongation factor (TEFM). During the elongation process, the interaction between TEFM and POLRMT is believed to amplify the processivity of POLRMT, facilitating the synthesis of extended RNA sequences.

The precise mechanism guiding the termination of HSP transcription remain a topic of discussion. Earlier, it was theorized that the H-strand transcription began at two distinct sites, namely HSP1 and HSP2 (Montoya et al., 1982). The transcription that started at HSP1 was thought to end right after the 16S rRNA gene, within the tRNALeu(UUR) gene. This would result in a shorter transcript containing both 12S and 16S rRNAs. On the other hand, the HSP2-initiated process was believed to continue beyond this point, generating a near-genome length transcript (Ojala et al., 1982). This notion was postulated to account for the markedly elevated levels of mitochondrial rRNAs observed. The termination of the HSP1-driven transcript was speculated to be controlled by the mitochondrial termination factor 1 (MTERF1) through mechanisms involving base flipping and DNA unwinding. However, this hypothesis faced challenges after studies on MTERF1 knockout mice, which showed no variation in the relative rRNA and mRNA levels. This suggests that the higher rRNA abundance may stem from augmented stability rather than the presence of a separate promoter (D'Souza and Minczuk, 2018).

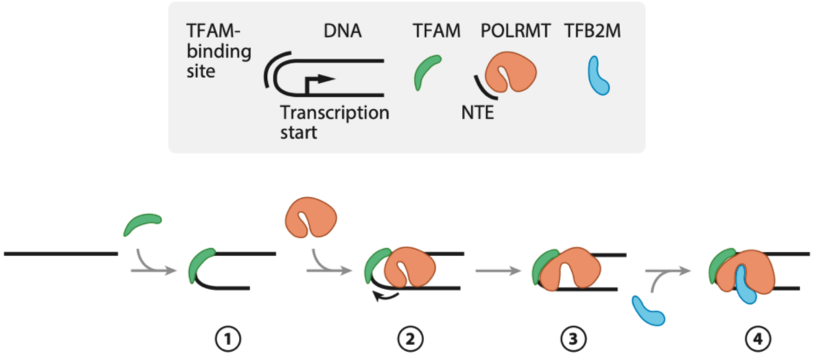

Figure 1.4. A sequential model of mammalian mitochondrial DNA transcription. (1) TFAM interacts with a high-affinity binding site just upstream of the transcription starting site and introduces a 180° bend in the DNA. (2) POLRMT is recruited by both TFAM and sequence-specific interaction with DNA. (3) In complex with DNA and TFAM, POLRMT undergoes a conformational change, which enables (4) the binding of TFB2M and the formation of a fully assembled initiation complex. Abbreviations: NTE, N-terminal extension; POLRMT, mitochondrial DNA-directed RNA polymerase; TFAM, mitochondrial transcription factor A; TFB2M, mitochondrial transcription factor B2 (image from figure 3, Gustafsson et al., 2016).

1.2.3. Replication of mtDNA

The replication of mtDNA is crucial for cellular function and relies on a tightly controlled process. In mammals, this replication is carried out by the DNA polymerase γ (POLγ), that ensures the replication of both the H- and L-strands (Gustafsson et al., 2016).

POLγ exists as a heterotrimer composed of one catalytic POLγA subunit and two accessory POLγB subunits. The catalytic subunit in humans has a molecular mass of 140 kDa and encompasses DNA 5’-3’ polymerase, 3’-5’ exonuclease, and 5’-deoxyribose phosphate lyase activities. The 3’-5’ exonuclease activity is crucial for proofreading and repairing errors during DNA synthesis, rendering POLγA highly accurate with a very low error rate (Kaguni, 2004). Disrupting the 3’-5’ exonuclease activity of POLγA in mice accelerates the accumulation of mutations in mtDNA (Trifunovic et al., 2004). Structurally, POLγA consists of N-terminal exonuclease and C-terminal polymerase domain separated by a linker domain, which plays a pivotal role in its interaction with the accessory subunit POLγB. The accessory subunit POLγB, with a molecular mass of 55 kDa, stabilizes interactions with template DNA, thereby enhancing POLγ. The vital roles played by POLγA and POLγB are highlighted by the fact that eliminating them from mice leads to early developmental arrest and significant mtDNA reduction (Hance et al., 2005).

Faithful replication of full-length mtDNA molecules also depends on the presence of other replication factors. *In vitro*, the minimal machinery for mtDNA synthesis consists of POLγ, the TWINKLE DNA helicase, and the mitochondrial single-stranded DNA-binding protein (mtSSB) (Falkenberg et al., 2007) (Figure 1.5).

The TWINKLE protein operates as a hexameric DNA helicase, uncoiling double-stranded DNA, relying on the energy provided by hydrolyzing nucleotide triphosphates. In the context of mitochondrial DNA replication, TWINKLE works together with POLγ by untwisting the double-stranded DNA template just ahead of the DNA polymerase. This action results in the creation of a single-stranded DNA (ssDNA) that POLγ then uses as a template to synthesize the complementary DNA strand (Spelbrink, 2010). The mtSSB protein forms a tetrameric structure when it binds to ssDNA. When mtDNA replication is underway, mtSSB envelops the exposed ssDNA, serving as a protective shield against nucleases. This protective action helps prevent the formation of secondary DNA structures and the unwanted creation of primers. Moreover, mtSSB plays an active role in enhancing mtDNA synthesis by boosting the helicase activity of TWINKLE and promoting the DNA synthesis function of POLγ (Korhonen et al., 2004).

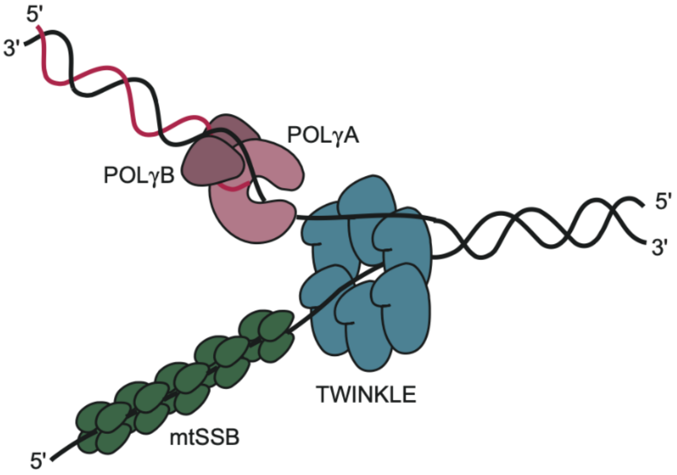

Figure 1.5. The mtDNA replication machinery. The TWINKLE helicase has 5' to 3' directionality and unwinds the duplex DNA template. The mtSSB protein stabilizes the unwound conformation and stimulates DNA synthesis by the POLγ holoenzyme (image from figure 3, Falkenberg et al., 2007).

The synthesis of mtDNA by POLγ necessitates an initial priming of DNA at the replication origins. This task is carried out by POLRMT, which, apart from its role in mtDNA transcription, also produces the RNA primers essential for starting the replication from the two mitochondrial origins, O_H and O_L (Fuste et al., 2010). When involved in mtDNA replication, POLRMT exhibits strong processivity on double-stranded DNA templates, facilitating the generation of full-length transcripts. However, with single-stranded DNA templates, POLRMT processivity is reduced, resulting in the production of brief primers ranging from 25-75 nucleotides in length, suitable for POLγ use (Wanrooij et al., 2008).

1.2.3.1. The mode of mtDNA replication

Mitochondrial DNA replication has been a subject of study for decades. As early as 1972, Vinograd and his group proposed a model, known as the strand displacement model, to explain how this process occurs (Robberson et al., 1972) (Figure 1.6). According to this model, both the heavy (H) and the light (L) strands of mtDNA undergo continuous synthesis.

The process begins at the O_H origin, where only the H-strand gets replicated, with the L-strand remaining unreplicated. During this phase, while TWINKLE moves along the parental H-strand ahead of POLγ, the displaced portion of the H-strand is covered by mtSSB (Miralles Fuste et al., 2014). This binding is crucial as it prevents the POLRMT from beginning random RNA synthesis on the now-exposed strand (Wanrooij et al., 2008). As the replication forks advances, it eventually crosses the O_L origin. When the parental H-strand in the O_L region becomes single-stranded, it forms a stem-loop configuration. This stem-loop efficiently prevents mtSSB from binding, allowing a short stretch of single-stranded DNA in the loop region to remain accessible for POLRMT to initiate RNA synthesis at this accessible point (Miralles Fuste et al., 2014, Fuste et al., 2010). However, POLRMT function is short-lived, as it gets replaced by POLγ after synthesizing 25 nucleotides, marking the beginning of L-strand DNA replication. From this point, both H- and L-strand synthesis goes on continuously until the replication is complete.

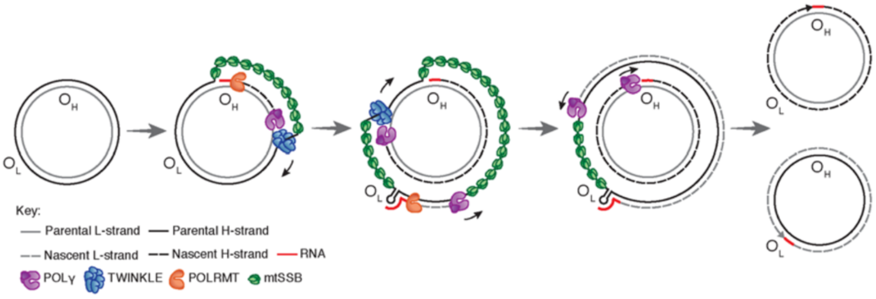

Figure 1.6. Strand-displacement mtDNA replication. Mitochondrial DNA replication is initiated at O_H and proceeds unidirectionally to produce the full-length nascent H-strand. mtSSB binds and protects the exposed, parental H-strand. When the replisome passes O_L, a stem-loop is formed that blocks mtSSB binding, presenting a single-stranded loop-region from which POLRMT can initiate primer synthesis. The transition to L-strand DNA synthesis takes place after about 25 nt, when POLγ replaces POLRMT at the 3′-end of the primer. Synthesis of the two strands proceeds in a continuous manner until two full, double-stranded DNA molecules have been formed (image from figure 2, Falkenberg, 2018).

However, there have been critiques and alternative suggestions to this model. One such alternative is the RITOLS (ribonucleotide incorporation throughout the lagging strand) model. This suggests that RNA molecules hybridize with the single-stranded H-strand, serving as a temporary lagging strand. Later in replication, this RNA is replaced by DNA. Despite this theory, the exact machinery needed for this RNA-based process remains unidentified (Reyes et al., 2013). However, the presence of RNaseH1 in mitochondria, an enzyme that actively degrades RNA molecules hybridized to single-stranded DNA argues against the use of RNA to stabilize single-stranded DNA regions (Holmes et al., 2015). Furthermore, the abundant presence of mtSSB in mitochondria suggests that alternative methods of protecting single-stranded DNA may not be necessary.

A third model for mtDNA replication, known as the strand-coupled model, has been proposed to account for specific observations in particular cell types and conditions (Holt et al., 2000). According to this model, mtDNA replication initiates bidirectionally at multiple points, and the newly synthesized L-strand is created as shorter fragments resembling Okazaki fragments, which are subsequently joined together to form a continuous strand (Holt et al., 2000). The formulation of this model was based on discoveries in certain cell types where Okazaki-like fragments were identified using neutral two-dimensional agarose gel electrophoresis (2D-AGE). However, the existence of these Okazaki-like fragments has been called into question, as they were not detected in organelle labeling experiments performed on purified mitochondria (Gustafsson et al., 2016).

1.3. Mitochondrial diseases

The original description of a mitochondrial disorder was by Luft and colleagues in 1962 (Luft, 1962). Their study involved two female patients who presented persistent fever, excessive sweating and an inability to tolerate heat. One of these patients had a preference for staying in a room maintained at 4 °C. Additionally, both individuals exhibited symptoms such as increased thirst and appetite, and polyuria. On physical examination, both patients displayed rapid heart rate and breathing, profuse perspiration, and warm, flushed skin. Furthermore, they experienced irregular reddish skin patches on their legs. Although some muscle weakness was evident, it remained mild and not confined to specific areas. This seminal report marked the dawn of the mitochondrial medicine. Subsequently over 150 unique genetic mitochondrial syndromes have been characterized, with the identification of more than 450 individual human genes as causative factors for mitochondrial diseases (https://genomit.eu/) (Figure 1.7).

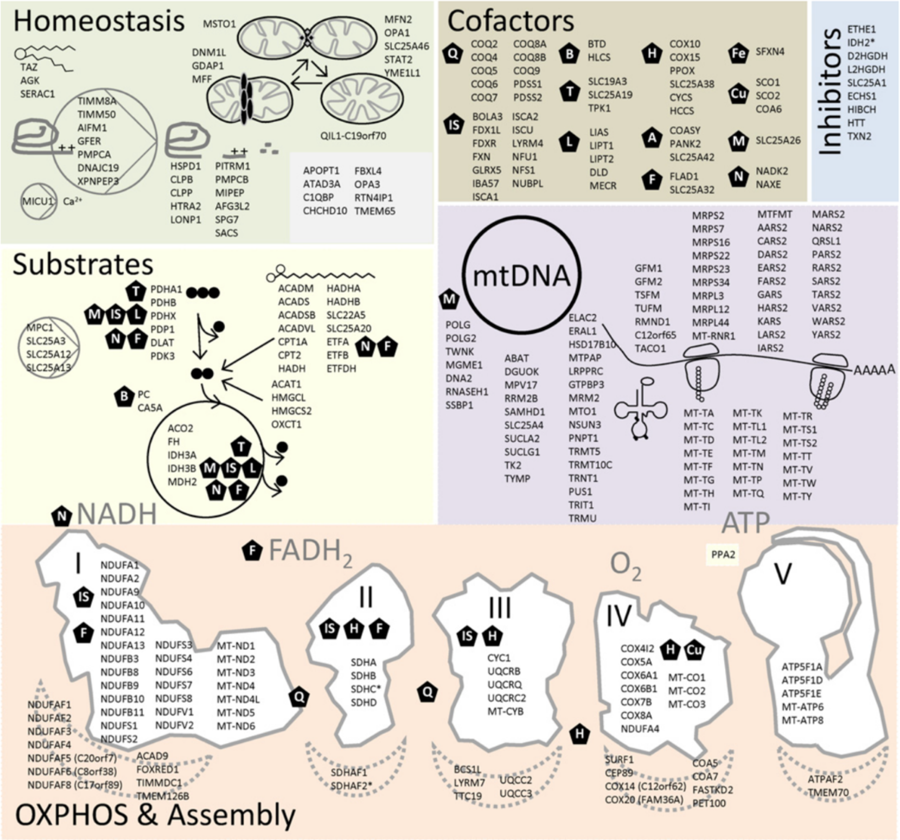

Figure 1.7. Mitochondria displaying the involved structures and known disease genes in different parts of mitochondrial energy metabolism. About 1,500 genes are thought to be involved in healthy mitochondrial function and disease-causing variants have been identified in ~300 implicated in mitochondrial metabolism (image from figure 1, Stenton and Prokisch, 2018).

Mitochondrial diseases arise from genetic abnormalities that impact the oxidative phosphorylation system (OXPHOS) in two main ways: either directly, such as affecting OXPHOS subunits or assembly factors, or indirectly by disrupting processes crucial for the proper formation of OXPHOS, including mtDNA replication, transcription, translation, biosynthesis of respiratory chain cofactors, and mitochondrial biogenesis. The former category is typically characterized by isolated biochemical deficiencies, which affect a specific complex within OXPHOS. In contrast, the latter category is often associated with multiple deficiencies in OXPHOS. The intricate and multifaceted nature of the biochemical pathways governing OXPHOS accounts for the remarkable heterogeneity seen in inherited mitochondrial disorders. These disorders encompass a wide spectrum of symptoms, severity levels, ages of onset, disease progression, and outcomes (DiMauro and Davidzon, 2005, Ghezzi and Zeviani, 2011). Mitochondrial diseases, when considered individually, are exceptionally rare. However, when grouped together, they rank among the most common inherited neurological disorders, affecting roughly 1 to 5,000 live births solely due to mtDNA mutation. This number rises further when accounting for common nuclear gene mutations (Ghezzi et al., 2018).

Mitochondrial disorders can potentially impact any tissue containing mitochondria (Figure 1.8). These diseases often manifest in multiple organs, particularly those with high metabolic requests, such as the brain (encephalopathies) and the skeletal muscle (myopathies). There are instances when both are affected, known as encephalomyopathies. Other organs like the heart and liver can also be affected, resulting in cardiomyopathies and hepatopathies (Ghezzi and Zeviani, 2018). In some rare cases, only one organ might be impacted, with Leber's hereditary optic neuropathy (LHON) causing isolated optic nerve atrophy being a notable example.

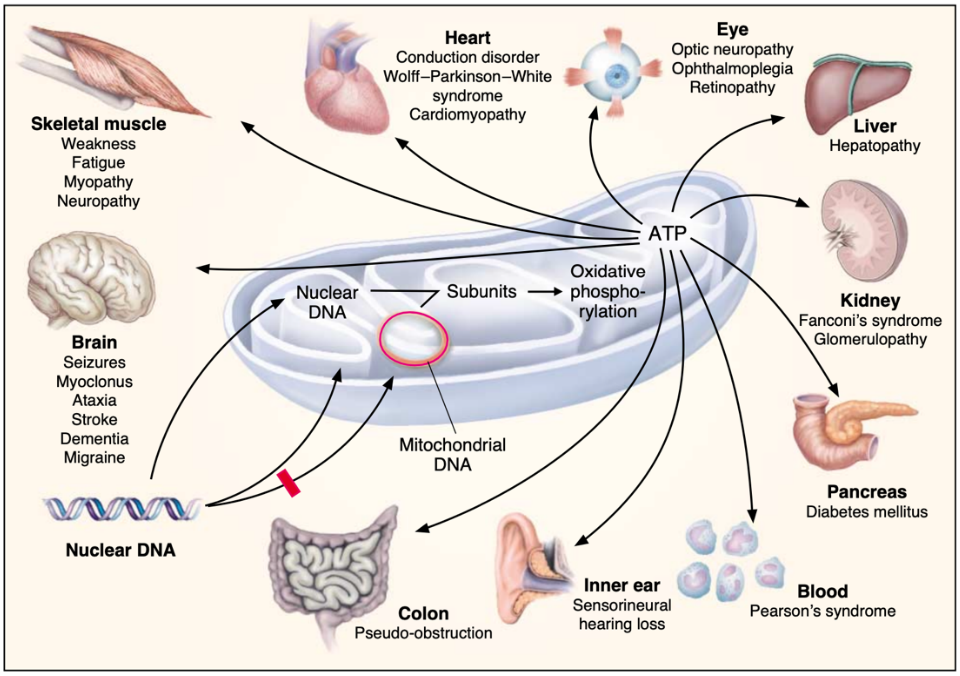

Figure 1.8. Dual genetic and multiple organ system manifestations of mitochondrial disease. The intricate function of the OXPHOS can be disrupted by defects in the subunits encoded by nDNA and mtDNA or by defects in intergenomic communication between the two types of DNA. The resulting deficits in the production of ATP has deleterious effects of a number of organ systems, causing the disorders shown in the picture (image from figure 1, Johns, 1995)

Mitochondrial diseases can present at any age, ranging from severe early childhood-onset syndromes to milder late-onset conditions. In adult-onset diseases, patients typically exhibit myopathy along with central nervous system abnormalities. Conversely, in infantile or childhood presentations, the severity is higher, affecting development and leading to cognitive impairment, as well as issues with muscular tone, coordination, cerebellar atrophy, dystonia, seizures, and respiratory problems (Gorman et al., 2016).

Mitochondrial maintenance and balance are controlled by nDNA and mtDNA. Consequently, mutations in these two genetic sources that result in mitochondrial dysfunction are significant contributors to human pathology and disease (figure 1.8). Notably, unlike nDNA, mtDNA is exclusively passed down through the maternal germ line (Wei and Chinnery, 2020). As a result, mitochondrial diseases can follow various model of inheritance, including Mendelian (autosomal or X-linked dominant or recessive) and non-Mendelian, such as maternal inheritance. In certain instances, these conditions arise from *de novo* mutations, particularly involving single macrodeletion in mtDNA. This complex genetic inheritance pattern further complicates the molecular diagnosis of the mitochondrial disorders.

1.3.1. Mutations in the mtDNA

It was not until 1988 that pathogenetic mutations in the mitochondrial genome were identified. In that year, Holt and his team discovered large-scale deletions in patients with mitochondrial myopathies (Holt et al., 1988), while Wallace and his colleagues found a point mutation in the gene responsible for subunit 4 of complex I (MTND4) connected to LHON (Wallace et al., 1988). These pioneering studies paved the way for more discoveries; from just one known mutation in 1988, the number of recognized pathogenic point mutations in mtDNA had increased to over 300 at latest count (http://www.mitomap.org) to which must added hundreds of large-scale deletions (figure 1.9). Around 80% of mitochondrial diseases that develop in adulthood and 25% that manifest in childhood are due to mutations in the mtDNA (Thorburn, 2004). Such mtDNA mutations can affect the proteins involved in OXPHOS either directly or indirectly. Direct impacts arise when mutations occur in genes coding for proteins. On the other hand, when mutations affect genes coding for mitochondrial tRNA or rRNA, the synthesis of these proteins is perturbed. More so, extensive mtDNA rearrangements, like major mtDNA deletions, can often interrupt several protein-coding genes as well as various tRNAs (Gorman et al., 2016).

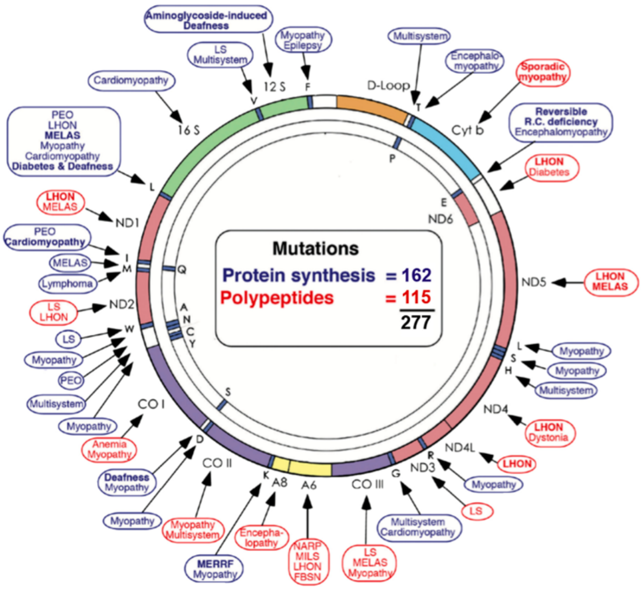

Figure 1.9. Mutations in the human mtDNA that are known to cause disease. Disorders caused by mutations in genes controlling protein synthesis are shown in blue and disorders caused by mutations in protein-coding genes are shown in red. FBSN, Familial bilateral striatal necrosis; LHON, Leber hereditary optic neuropathy; LS, Leigh syndrome; MELAS, mitochondrial encephalomyopathy, lactic acidosis, and stroke-like episodes; MERRF, myoclonus epilepsy and ragged-red fibers; MILS, maternally inherited Leigh symdrome; NARP, neuropathy, ataxia, retinitis pigmentosa; PEO, progressive external ophthalmoplegia (image modified from figure 3, Di Mauro and Schon, 2003).

One of the intricate aspects of many mitochondrial diseases is that cell may contain multiple mtDNA copies. In many cases, pathogenic mtDNA mutations can coexist alongside normal mtDNA molecules, a situation termed heteroplasmy (Stewart and Chinnery, 2021). Factors such as a germline bottleneck and the uneven distribution of mutated mtDNA in different tissues during growth can create significant variations in heteroplasmy levels. The germline bottleneck results from a combination of a reduction in overall mtDNA copy numbers and an imbalanced distribution of mutated and normal mtDNA during the gamete formation. This leads to diverse distributions of mtDNA mutations in the formed gamete cells (Stewart and Chinnery, 2021). Throughout an individual's life, some mtDNA types might accumulate in non-dividing tissues, causing mutated mtDNA to outnumber the normal ones. This process is called clonal expansion (Stewart and Chinnery, 2021). Interestingly, even in the absence of cell division, clonal expansion can take place via a mechanism called relaxed replication, where mtDNA replication is independent from nuclear DNA replication (van den Ameele et al., 2020). Further, evidence suggests that some mutant mtDNAs might have a replication advantage, such as mtDNA with extensive deletions, which replicate more rapidly (Stewart and Chinnery, 2015).

Clinical symptoms arising from OXPHOS biochemical defects usually emerge when there is a significant proportion (usually ≥60% in critical tissues) of heteroplasmic mutant mtDNA (Payne et al., 2013). The degree of heteroplasmy is associated with the likelihood of developing severe illness. For example, the m.8993T>G mutation in the MT-ATP6 gene is associated with two distinct syndromes. The first, NARP (neuropathy, ataxia, retinitis pigmentosa), typically manifests in young adults, leading to symptoms such as retinitis pigmentosa, cognitive decline, seizures, ataxia, proximal weakness, and sensory neuropathy. The second syndrome is MILS (maternally inherited Leigh syndrome), a more severe infantile encephalopathy with characteristic symmetrical lesions found in the basal ganglia and brainstem. The variation in severity between these two conditions can be attributed to the prevalence of the mutation: about 70% for NARP and roughly 90% for MILS (Tatuch at al., 1992). Even with similar heteroplasmy levels, a specific mtDNA mutation can lead to varying clinical manifestations. Notably, the m.3243A>G mutation, located in the MTTL gene that encodes the tRNALeu(UUR), is among the most common mtDNA mutations and is linked to a variety of syndromes (Pickett et al., 2018). Sometimes cells might have only mutant mtDNA, a condition referred to as homoplasmy. Yet, even with homoplasmy, symptoms can vary, pointing to the impact of other elements. For instance, while mtDNA mutations linked to LHON, which leads to sudden central vision loss in young adults, are often homoplasmic, not everyone with these mutations displays symptoms. In fact, a higher risk of developing LHON has been associated with male gender and lifestyle factors. The reason for this increased risk in men remains unclear genetically, but epigenetic factors, particularly the protective effect of estrogen in women, appear to be involved (Giordano et al., 2011). Studies have shown that enhanced mitochondrial biogenesis can serve as a protective element against the manifestation of LHON (Giordano et al., 2014). This suggests that the appearance of clinical symptoms due to mtDNA mutations could also be shaped by various genetic, environmental, and epigenetic contributors. Considering that mitochondria rely on both nDNA and mtDNA, and the possible interactions between them, such findings are expected (Chinnery et al., 2012).

1.3.2. Mutations in the nDNA

In 1989, Zeviani and his team identified an Italian family suffering from an adult-onset mitochondrial disorder. This condition was marked by chronic progressive external ophthalmoplegia (CPEO) and was linked to multiple deletions in the mtDNA. Notably, male family members passed on this condition to their children, indicating that the inheritance was not purely maternal. This pointed to the fact that the genetic defect causing the condition was not in the mtDNA but possibly in the nDNA. The disorder was inherited in an autosomal dominant manner. This discovery provided the first evidence that a mutation in a nuclear DNA-encoded protein could specifically and hereditarily impact mtDNA integrity (Zeviani et al., 1989). At the time of the initial discovery, the exact genetic mutation responsible was not pinpointed because comprehensive diagnostic methods were not available. Six years later, the first nDNA mutation related to mitochondrial diseases was identified (Bourgeron et al., 1995). A mutation in the nuclear-encoded flavoprotein subunit gene of the succinate dehydrogenase (SDH) was identified in two siblings with complex II deficiency affected by Leigh disease. Both patients were homozygous for an R554W substitution in the flavoprotein subunit (Bourgeron et al., 1995). Since the introduction of the whole exome sequencing (WES) as a diagnostic tool, over 450 nuclear genes have been discovered to be linked to mitochondrial diseases (Figure 1.10).

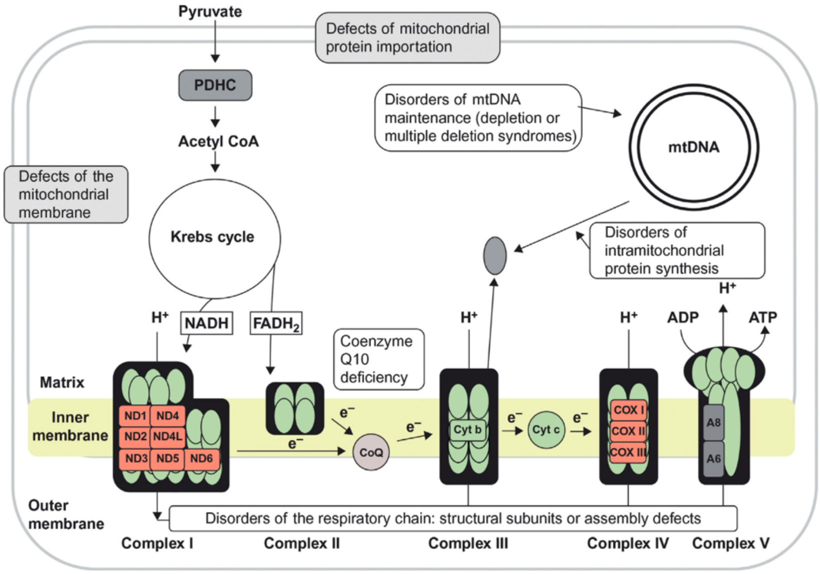

Figure 1.10. Mitochondrial disorders due to mutations in the nuclear genome (image from Rosenberg, Roger N., and Juan M. Pascual, editors. Rosenberg's Molecular and Genetic Basis of Neurological and Psychiatric Disease. 6th ed., vol. 1, Elsevier/Academic Press, 2020).

It is estimated that roughly 20% of mitochondrial diseases starting in adulthood and 75-80% beginning in childhood are due to mutations in the nDNA (Gorman et al., 2016). Among these, autosomal recessive mutations are predominantly responsible for the most severe syndromes that appear during childhood (Spinazzola and Zeviani, 2009). Mitochondrial diseases can emerge from the mutations in genes that encode for over a thousand proteins that the mitochondria rely upon for their function. Critical to this is the Oxidative Phosphorylation System (OXPHOS), the pathway responsible for ATP production in the cell. While the mtDNA directly codes for certain proteins involved in OXPHOS, a vast number of nuclear-encoded components are essential for its proper assembly and functionality, including all the constituents of Complex II. Genetic anomalies in these structural and assembly proteins can inhibit the incorporation or functionality of core OXPHOS components (Ghezzi and Zeviani, 2018) (Figure 1.10).

Furthermore, alterations in nuclear-encoded genes have the potential to indirectly impact OXPHOS by disrupting various processes essential for the effective assembly of OXPHOS components. These processes encompass a wide range of functions, such as the maintenance of mtDNA and its related gene expression activities (including mtDNA replication, transcription, and translation), the provision of deoxyribonucleotide triphosphates (dNTPs) required for mtDNA synthesis, the maintenance of protein quality control within mitochondria, and the regulation of mitochondrial dynamics involving fusion and fission events (Viscomi and Zeviani, 2017).

1.3.3. Leigh syndrome

Leigh syndrome (LS), also known as subacute necrotizing encephalomyelopathy, was first identified as a neurological condition in 1951. Leigh described the macroscopic and microscopic characteristics of the brain of a seven-month-old infant who had died following a six-week illness marked by symptoms such a drowsiness, difficulty with feeding, excessive sweating, optic atrophy, loss of hearing, progressive encephalopathy and terminal hyperpyrexia (Leigh, 1951). Leigh identified bilateral symmetrical lesions extending from the thalamus through brainstem structures to the posterior columns of the thoracic spinal cord. On closer inspections, these damaged areas showed intense capillary proliferation, gliosis and severe neuronal loss.

Historically, Leigh syndrome diagnosis was dependent on postmortem brain examination until the 1990s. By then, MRI technology, particularly T2-weighted imaging, emerged as a tool to detect the characteristic hyperintense lesions associated with the disorder (Medina et al., 1990). This discovery significantly improved the early recognition of the condition in infants and children. In 1996, strict diagnostic criteria for Leigh syndrome were proposed (Rahman et al., 1996), later updated to acknowledge a Leigh syndrome spectrum, encompassing various mitochondrial encephalomyopathies. The revised definition includes a characteristic clinical history featuring neurodevelopmental delay and/or regression, along with neuropathological confirmation or MRI evidence of symmetrical T2 hyperintense brain lesions in specific areas (basal ganglia, thalamus, midbrain and brainstem). Furthermore, the presence of biochemical indicators of mitochondrial dysfunction, such as elevated lactate levels or abnormal oxidative phosphorylation enzyme activities, is considered as part of the diagnostic process.

Leigh syndrome is the most common clinical presentation of mitochondrial disease in children. Most patients manifest symptoms before the age of 24 months, with the average age of onset being 7 months (Pincus, 1972, Sofou et al., 2014). However, it is also known that symptoms can begin later in life, even during adulthood. The exact prevalence is uncertain due to misdiagnoses or alternative classifications. However, two studies from Australia and Sweden estimate the birth prevalence to be around 1 in 40,000 and 1 in 34,000 respectively (Rahman et al., 1996, Darin et al., 2001). There is a notable male preponderance, with a male-to-female ratio of 1.7:1, the cause of which is not fully understood. While Leigh syndrome affects all ethnicities, certain genetic subtypes are more prevalent in specific regions, such as mutations in LRPPRC in the French-Canadian population (Debray et al., 2011) and in the British Pakistani community (Oláhová et al., 2015).

LS during childhood is characterized by developmental regression, where children lose previously acquired developmental milestones. This regression often occurs following an illness or metabolic stressors (e.g., surgery or fasting) but sometimes without an obvious trigger (Rahman et al., 1996). Affected children may have hypotonia due to various factors, including central and neuromuscular causes. Neurological symptoms involve specific brain regions, including the basal ganglia, thalamus, midbrain, and brainstem, resulting in conditions such as dystonia, spasticity, ataxia, tremors, ophthalmoplegia, and breathing abnormalities (Rahman et al., 1996, Finsterer, 2008 Baertling et al., 2014). Ophthalmological problems like optic atrophy and retinopathy, as well as sensorineural hearing loss, are common. Peripheral neuropathy can also occur, particularly in cases involving

SURF1 deficiency (Menezes et al., 2016). In adults, Leigh syndrome may manifest as spinocerebellar ataxia, peripheral neuropathy, and psychiatric symptoms.

LS has been reported to be caused by defects in 16 mitochondrial genes, which are responsible for encoding 10 subunits of OXPHOS and 6 tRNAs, and over 75 nuclear genes (Schubert and Vilarinho, 2020). Complex I deficiency is notably the most common biochemical abnormality observed in LS patients (Rahman et al., 1996). Indeed, Leigh syndrome often presents itself as the primary manifestation of this deficiency, with a systematic review identifying 65 out of 130 patients with nuclear-encoded CI deficiency displaying LS symptoms (Koene et al., 2012). Genetic investigations have identified a significant cluster of 30 genes associated with Leigh syndrome that are related to CI. This set comprises 6 mtDNA- and 16 nuclear-encoded subunits, along with 8 assembly factors. Specifically, mtDNA-encoded subunits implicated in Leigh syndrome are ND1, ND2, ND3, ND4, ND5, and ND6 (Lake et al., 2016). Regarding the nuclear subunits, many of the defects are rare and have been identified in a limited number of families. However, recurrent mutations appear particularly in the NDUFS1, NDUFS2, NDUFS4, and NDUFV1 subunits. Among the assembly factors of CI, NDUFAF2, NDUFAF5, and NDUFAF6 defects are predominantly associated with Leigh syndrome (Lake et al., 2016).

1.3.4. POLG-related disorders

Mutations in the POLG gene, which encodes for the catalytic subunit of the mitochondrial DNA polymerase (POLγA), are a major contributor to a variety of mitochondrial disorders due to their destabilizing effects on mtDNA (Chinnery and Zeviani, 2008). In 2001, Van Goethem et al. published a seminal paper describing four mutations in POLG that were associated with either autosomal dominant or autosomal recessive progressive external ophthalmoplegia (adPEO or arPEO) (Van Goethem et al., 2001). Since that pivotal work, over 300 mutations in POLG have been recorded (Human DNA Polymerase Gamma Mutation Database: https://tools.niehs.nih.gov/polg/) (Figure 1.11).

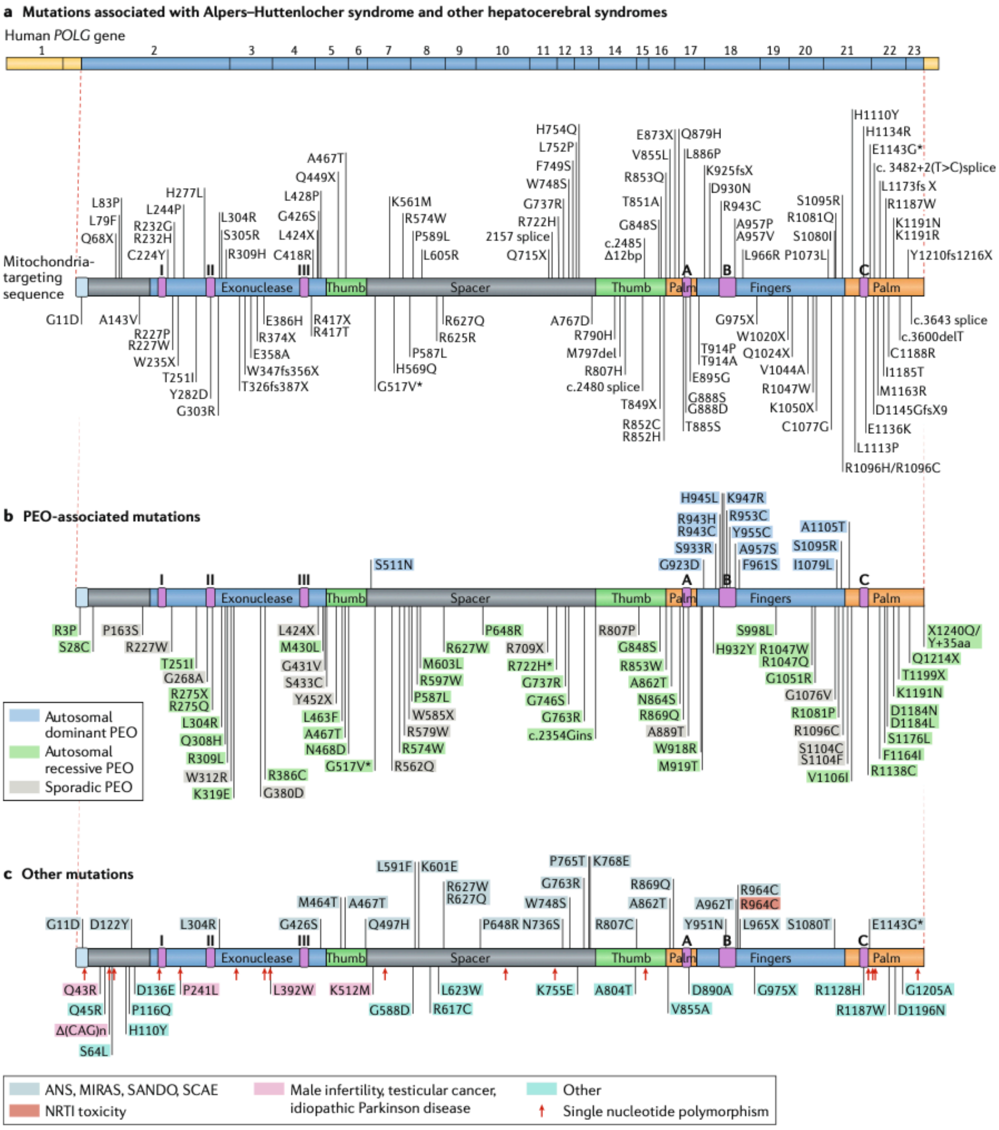

Figure 1.11. POLG mutations. Mutation map depicting disease-associated amino acid substitutions on the primary structure of POLG. In each panel, the top line depicts the 23 exons of the cDNA and the lower line represents the linear polypeptide with the functional domains (exonuclease and polymerase) indicated. **a** | Mutations associated with Alpers–Huttenlocher syndrome and other infantile hepatocerebral syndromes that cause mitochondrial DNA depletion. **b** | Mutations associated with progressive external ophthalmoplegia (PEO). **c** | Other mutations linked to POLG-related disease. ANS, ataxia neuropathy spectrum; MIRAS, mitochondrial recessive ataxia syndrome; NRTI, nucleoside reverse transcriptase inhibitor; SANDO, sensory ataxia neuropathy dysarthria and ophthalmoplegia; SCAE, spinocerebellar ataxia with epilepsy (image from figure 2, Rahman and Copeland, 2019).

POLG mutations can cause early childhood mtDNA depletion syndromes or later-onset syndromes arising from mtDNA deletions. These mutations are the leading single-gene cause of mitochondrial disease, representing 10% of such cases in a notable Australian group (Woodbridge et al., 2013). They are the primary cause of mitochondrial epilepsy across all age groups (Rahman, 2012) and they also constitute 10-25% of PEO cases (Bugiardini et al., 2017) and more than 10% of ataxia cases (Schicks et al.,2010).

POLG-related disorders are commonly linked with four predominant mutations: A467T, W748S, G848S, and the T251I-P587L allelic pair. In a study, it was found that these mutations made up half of all the mutations in individuals suffering from POLG-related conditions and about 75% of patients carried at least one of the aforementioned mutations (Uusimaa et al., 2013). A467T stands out as the most frequent pathogenic variant of POLG, representing an estimated 36% of all alleles linked to POLG-related disorders (Wong et al., 2008,). This mutation has been shown to dramatically reduce the activity of POLγ to just 4% of its typical activity. It does this by reducing the affinity of the enzyme for dNTPs and lowering catalytic activity (Chan et al., 2005). Moreover, the mutated POLγA subunit is not able to bind to the accessory subunit POLγB, which is indispensable for the continuous synthesis of DNA. These combined defects lead to stalling at the replication fork and a reduction of mtDNA over time. Following A467T, W748S is the next most prevalent POLG mutation. Its effects are a decrease in DNA polymerase activity, hindered processivity and a strong DNA-binding defect, though it still maintains standard interactions with POLγB (Chan et al., 2006). Intriguingly, W748S usually coexists with the E1143G mutation and is a common cause of ataxia neuropathy spectrum (ANS) (Hakonen et al., 2005). The third leading mutation in the POLG mutation database is G848S. This problematic variant leads to a drastic reduction of the DNA polymerase activity, often less than 1%, accompanied by a defect in its DNA-binding function (Kasiviswanathan et al., 2009). The T251I and P587L mutations, typically found together and prevalent in about 1% of the Italian population, have been associated with PEO (Ferrari et al., 2005). Individually, these two mutations lead to an approximate 30% decline in DNA polymerase activity. However, when combined, their effects become compounded, causing a significant drop in polymerase function to around 5% of the normal. This is due to a combination of decreased enzyme stability, impaired DNA-binding affinity, and reduced catalytic efficiency (DeBalsi et al., 2017). Lastly, the Y955C variant is notable as the most frequently occurring autosomal dominant mutation in POLG, leading to adPEO. Its consequences can extend to parkinsonism or premature ovarian failure (Luoma et al., 2004, Pagnamenta et al., 2006). The Y955C mutation results in a drastic reduction in DNA polymerase activity, often less than 1% (Ponamarev et al., 2002). Overall, the consequences of POLG mutations can be divided in two broad groups: multiple mtDNA deletions and mtDNA depletion. It is challenging to directly link specific POLG mutations to particular outcomes because the same mutation can lead to either mtDNA deletions, mtDNA depletion, or both. This means it is not straightforward to anticipate the clinical manifestations just by looking at the identified mutations. For instance, individuals who have two copies of the most frequent POLG mutation, A467T, can exhibit a variety of clinical features, including severe childhood-onset conditions like Alpers-Huttenlocher Syndrome (AHS), or other disorders such as Myoclonic epilepsy myopathy sensory ataxia (MEMSA), Ataxia neuropathy spectrum (ANS), and sensory ataxia neuropathy dysarthria and ophthalmoplegia (SANDO) (Neeve et al., 2012, Rajakulendran et al., 2016).

POLG-related disorders can manifest at any stage of life, from infancy to late adulthood. These disorders encompass a range of at least six primary syndromes. AHS is recognized by its childhood onset, progressing into severe encephalopathy accompanied by challenging-to-treat epilepsy and hepatic failure. On the other hand, individuals displaying symptoms of the childhood myocerebrohepatopathy spectrum (MCHS) exhibit developmental delays, lactic acidosis, myopathy, and liver dysfunction. Myoclonic epilepsy myopathy sensory ataxia (MEMSA) encompasses a spectrum of disorders with epilepsy, myopathy, and ataxia, typically without ophthalmoplegia, including disorders previously described as spinocerebellar ataxia with epilepsy (SCAE) (Rahman and Copeland, 2019). Ataxia neuropathy spectrum (ANS) comprises two conditions: mitochondrial recessive ataxia syndrome (MIRAS) and sensory ataxia neuropathy dysarthria and ophthalmoplegia (SANDO). arPEO is characterized by progressive weakness of the extraocular muscles, resulting in ptosis and ophthalmoparesis without associated systemic involvement. adPEO typically includes generalized myopathy and variable degrees of sensorineural hearing loss, axonal neuropathy, ataxia, depression, parkinsonism, hypogonadism, and cataracts (Rahman and Copeland, 2019) (Figure 1.12).

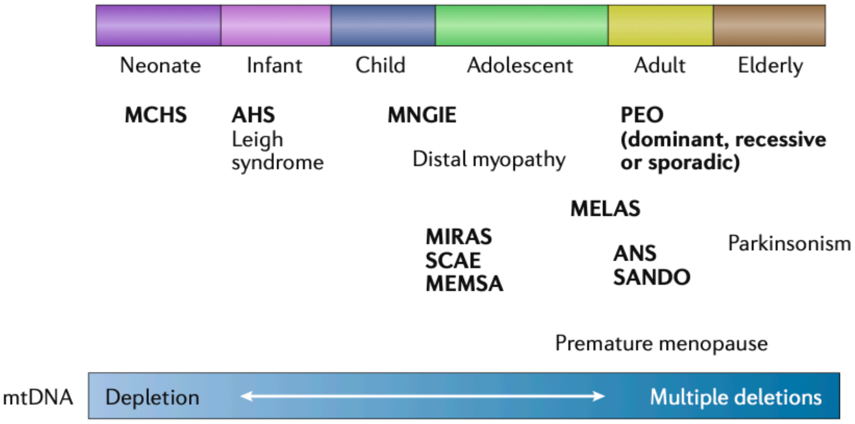

Figure 1.12. The clinical spectrum of POLG-related disease. Clinical spectrum of POLG-related disease according to age of onset, and the defects (mitochondrial DNA (mtDNA) depletion or deletions) associated with the diseases. Bold text indicates the most prevalent conditions (image from figure 1, Rahman and Copeland, 2019).

1.3.5. Experimental therapy for mitochondrial diseases

Mitochondrial diseases are typically highly disabling, complex conditions characterized by multisystem disfunction, with a prevalence of neurological impairment (Silva-Pinheiro et al., 2020). Currently, no curative therapies for mitochondrial disorders are available and interventions are based on management of the complications and supportive care to the patient. Over the past three decades, significant progress has been made in understanding the key mechanisms underlying mitochondrial disorders (Viscomi and Zeviani, 2020). It is now evident that mitochondria play a pivotal role in many signaling and executive pathways. This enhanced knowledge of the mechanistic aspects of mitochondrial diseases has paved the way for the identification of various potential treatments for these conditions. These approaches encompass methods that could theoretically address multiple diseases (generalist strategies) as well as treatments designed specifically for one particular disease ("disease-tailored" strategies) (Viscomi and Zeviani, 2020).

1.3.5.1. General therapeutic strategies

Some of these strategies include:

i. Activation of the mitochondrial biogenesis: This involves stimulating the production of new mitochondria in order to compensate for the dysfunctional ones. It can be achieved by activating PGC1α, which is the master regulator of the mitochondrial biogenesis. This can be done through the use of AMPK activators, such as AICAR (Viscomi et al., 2011), or by increasing the NAD$^+$ levels through the use of nicotinamide riboside (NR) or PARP inhibitors (Cerutti et al., 2014).

ii. Antioxidant therapy: Mitochondrial disfunction leads to an increase in reactive oxygen species (ROS), which can damage cells. Antioxidants can help scavenge these ROS and protect cells from oxidative stress. Examples of antioxidants used in the treatment of mitochondrial diseases include ascorbic acid, coenzyme Q10, and idebenone (Polyak et al., 2018, Abu-Libdeh et al., 2017).

iii. Hypoxia therapy: Hypoxia, or low oxygen levels, can stimulate the cellular response to mitochondrial dysfunction and improve mitochondrial function. Approaches such as intermittent hypoxia or exposure to non-lethal concentrations of carbon monoxide have shown potential to improve mitochondrial function in preclinical studies (Jain et al., 2016, Jain et al., 2019).

iv. Targeting mTORC1: The mTOR (mechanistic target of rapamycin) pathway plays a role in regulating cellular metabolism and growth. Inhibition of mTORC1 (mTOR complex I) with compounds like rapamycin and its analogs has shown promising results in improving mitochondrial function and extending lifespan in preclinical studies (Civiletto et al., 2018, Siegmund et al., 2017).

1.3.5.2. Disease-tailored strategies

Disease-tailored strategies refer to therapeutic approaches that specifically target the underlying cause of a specific disease. These strategies are designed to address the specific genetic or biochemical abnormalities that contribute to the disease. Examples of disease-tailored strategies for mitochondrial diseases may include gene therapy, supplementation of nucleotides, and supplementation of CoQ.

1.3.5.2.1. Gene therapy

The idea of gene therapy emerged in the 1970s, envisioning a method to replace defective genes with their WT versions. The principle behind this is simple: reintroduce the normal version of a faulty or absent gene to potentially alleviate the symptoms caused by the defective gene. This approach is particularly promising for genetic conditions, especially those that arise from single-gene mutations where just one working copy could prevent the disease from manifesting (Naldini et al., 2015).

Over the years, researchers have explored two main categories of vectors for delivering genes systematically in clinical trials: viral vectors and non-viral vectors. A large number of gene therapy trials have utilized modified recombinant viruses, including retroviruses, lentiviruses, adenoviruses, and adeno-associated viruses (AAVs), by replacing certain harmful genetic components with therapeutic genes

(Kay et al., 2001). While these viral vectors have been instrumental in the advancement of gene therapy, they have also revealed certain challenges, particularly in safety. Concerns have arisen due to their association with cancer development and unwanted immune reactions (Baum et al., 2006, Bessis et al., 2004). To address these challenges, researchers have turned to non-viral gene therapy, using synthetic molecules, like liposomes and polymers, to assist in delivering DNA into cells. These non-viral vectors have the advantage of being less immunogenic than viral vectors and they do not face the challenge of pre-existing immunity to viral capsid proteins (Yin et al., 2014). However, non-viral vectors exhibit reduced efficiency in systemic delivery when compared to viruses, which have naturally evolved to effectively introduce their genetic material into cells (Yin et al., 2014).

1.3.5.2.2. AAV-based gene therapy

The prevailing approaches for treating genetic diseases with gene therapy using viral vectors have largely converged on two main vector types: lentivirus for ex vivo gene transfer into hematopoietic and other stem cells and AAV for in vivo transfers into postmitotic tissues (Naldini, 2011).

AAVs belong to the Dependoparvovirus genus within the Parvoviridae family. Its existence is dependent on a helper virus like AdV, leading to its particular name and classification. AAV is present in several vertebrates, including humans and non-human primates (NHPs). Currently, it is believed that AAV does not cause diseases in humans. The structure of AAV includes a protein capsid about 26 nm in size and a single-stranded DNA genome approximately 4.7 kb in length, which can be either plus (sense) or minus (anti-sense) (Muzyczka and Berns, 2001). This capsid consists of three subunits: VP1, VP2, and VP3, which are present in a 1:1:10 ratio respectively. The AAV genome has two inverted terminal repeats (ITRs) at its ends, which are essential for viral replication and packaging. The AAV genome has a rep gene encoding four proteins crucial for its replication, named based on their sizes: Rep78, Rep68, Rep52, and Rep40. The cap gene is responsible for the three capsid subunits, produced through alternate splicing and different start codon translations. Another gene within the cap coding sequence encodes the assembly activating protein (AAP) which aids in virion assembly (Sonntag et al., 2010). Interestingly, the AAV genome can integrate into the AAVS1 locus in human cells, establishing latency. This integration is partly due to sequence similarities between AAVS1 and the ITR, along with Rep activity. It should be noted that recombinant AAV (rAAV) lacks the rep gene, reducing the likelihood of rAAV genome integration.

Recombinant AAVs (rAAVs) possess the same capsid structure as their wild-type counterparts (wtAAVs). However, instead of the usual AAV protein-coding sequences, rAAVs carry therapeutic gene cassettes. The only remaining viral sequences are the inverted terminal repeats (ITRs), essential for genome replication and packaging during the production of the vector. By omitting the viral coding sequences, rAAVs can accommodate larger therapeutic payloads and exhibit lower immunogenicity and cytotoxicity when introduced into a living organism. These ITR-enclosed rAAV genomes can be integrated into plasmids, allowing for modifications using conventional molecular cloning methods. However, it is vital to note that rAAVs can ideally hold genomes less than 5.0 kb in size (Dong et al., 1996). This means the design of the therapeutic content must take into account not only the actual therapeutic gene but also essential regulatory elements like promoters and polyadenylation signals.

The efficacy of rAAV largely depends on the molecular interactions between its capsid and the receptors on the target cell surface (Huang et al., 2014). Current serotypes are believed to identify unique cell receptors, like glycoproteins, and therefore display different tissue-type and cell-type tropism profiles. After receptor recognition the AAV is internalized by endocytosis (Duan et al., 1999, Bartlett et al., 2000). Within endosomes, intact rAAV particles undergo pH-dependent structural changes necessary for transduction and traffic through the cytosol using the cytoskeletal network (Wang et al., 2019). Following endosomal escape, rAAV enters the nucleus through the nuclear pore complex, where it undergoes capsid uncoating to release its genome. The single-stranded rAAV genome released in the nucleus is not immediately ready for gene expression; it needs to be converted into a double-stranded form, which is a critical step for transduction (Fischer et al., 1996, Ferrari et al., 1996). After second strand synthesis, the double-stranded genome undergoes circularization either through intra-molecular or inter-molecular genome recombination at the ITRs. This circularization and concatemerization process stabilize the rAAV genome as episomal DNA, ensuring persistent gene expression in postmitotic cells.

In the context of mitochondrial diseases, AAVs have been used to deliver therapeutic genes in several mouse models of mitochondrial diseases. This includes models of autosomal dominant optic atrophy (ADOA) (Sarzi et al., 2018), mitochondrial neurogastrointestinal encephalomyopathy (MNGIE) (Torres-Torronteras et al., 2018), ethylmalonic encephalopathy (EE) (Di Meo et al., 2012), and Leigh syndrome (Di Meo et al., 2017). MNGIE and EE, despite being distinct diseases, both exhibit elevated levels of harmful compounds: pyrimidine nucleotides in the case of MNGIE and hydrogen sulfide for EE. In mouse models for both conditions, AAV8 vectors targeting the liver were utilized to introduce the normal gene, compensating the impaired function of the defective one. This approach facilitated the liver ability to eliminate the toxic compound from the blood and surrounding tissues (Di Meo et al., 2015). In 2017, it was demonstrated by Di Meo et al. that the phenotype of *Ndufs4*$^{-/-}$ mice could be partially restored using human *NDUFS4* only when the AAV9 vector was simultaneously administered systematically and intracranially (Di Meo et al., 2017). This underscores the potential and the difficulties of targeting multiple organs, especially the brain, which is protected by the blood-brain barrier (BBB). Indeed, the AAV9 serotype did not readily cross the BBB, and primarily targeted the glial cells when injected into the brains of newborn mice. Interestingly, newly developed serotypes, like PHP.B have gained attention for their remarkable ability to cross the BBB (Chan et al., 2017). Results from our lab using a PHP.B vector on *Ndufs4*$^{-/-}$ mice confirm the potential of AAV-based gene therapies specifically designed for the brain to address mitochondrial diseases and potentially other conditions (Silva-Pinheiro et al., 2020). However, the applicability of PHP.B for clinical use is restricted due to its liver toxicity seen in non-human primates and its dependence on the presence of Ly6a, a glycosylphosphatidylinositol protein, which is not found in primates (Hordeaux et al., 2019).

1.4. Aims of the thesis

This thesis has twofold aims:

1) To develop a gene therapy strategy in a mouse model of Leigh disease the *Ndufs4*$^{-/-}$ mouse, using a self-complementary adeno-associated viral 9 vector (scAAV9).

2) To investigate the molecular pathogenesis of *POLG*-related diseases by (i) characterizing a knockin mouse model harboring a *POLG* Y933C mutation, which corresponds to Y955C, the most common autosomal dominant POLG mutation found in human patients, (ii) characterizing *in vitro* the human and murine mutations using purified recombinant protein versions of POLγA.

Chapter 2

Materials and Methods

2. Materials and Methods

2.1. Mouse models and associated procedures

All animal experiments were carried out in accordance with the EU Directive 2010/63/EU. The *Polg*$^{+/Y933C}$ and *Ndufs4*$^{-/-}$ mice were kept on C57BL/6J background, and wild-type (WT) littermates were used as controls. The animals were maintained in a temperature- and humidity-controlled animal care facility with a 12-h light/12-h dark cycle and free access to food and water, and they were monitored weekly to examine body condition, weight, and general health. The mice were sacrificed by cervical dislocation at the indicated age for subsequent analysis.

2.1.1. Generation of the *Polg*$^{+/Y933C}$ mouse

The *Polg*$^{+/Y933C}$ mice were generated using the single nuclease CRISPR/Cas9 WT approach. All the components of the system (Cas9-WT, gRNAs, and HDR template) were first electroporated in embryonic stem (ES) cells, followed by the screening of positive clones, and generation of chimer mice harbouring the *Polg* Y933C allele. The Cas9 WT mRNA (Sigma-Aldrich), the IVT gRNA-Fw1: 5’-ATG GCC GCA TCT ATG GGG CT-3’ (GeneArt) and the HDR template (IDT) were sent to the “Core Facility for Conditional Mutagenesis” at the IRCCS Ospedale San Raffaele (Milan, Italy), where they were delivered to mouse ES cells by electroporation. The cells were then seeded as single clone in 96-well plates and allowed to grow for DNA extraction. One of the positive clones (3B2p2oL2) was expanded and microinjected into blastocysts, originating one female chimeric mouse. The chimera was then bred with a WT male to verify germline transmission. Genotyping of the pups allows the identification of founder mice (F_0), heterozygous for the Y933C allele (*Polg*$^{+/Y933C}$) and confirmed the generation of a *Polg*^{Y933C} mouse line.

2.1.2. Phenotypic analysis

2.1.2.1. Treadmill

A standard treadmill apparatus (Panlab) was used to measure motor exercise endurance according to the number of falls in the motivational grid during a gradually accelerating program with speed initially set at 8 cm/s and increasing by 2 cm/s every 5 min. The test was terminated by exhaustion, defined as >10 falls/min into the motivational grid.

2.1.2.2. Rotarod

A rotarod apparatus (Ugo Basile) was used to assess coordination skills. During the test, mice had to maintain themselves on a rod turning at accelerating speeds. The latency to fall was recorded. The mice underwent three trial sections at least 20 min apart, using an acceleration protocol from 2 to 40 rpm in 300 seconds.

2.1.3. *In vivo* adeno-associated virus (AAVs) transduction

The human NDUFS4 (hNDUFS4) gene was cloned into a scAAV9-CAG vector by Dr Samantha Corrà (Dep of Neuroscience, University of Padua). The scAAV9-hNDUFS4 viral particles were synthesized by the AAV Vector Core of the Telethon Institute of Genetics and medicine (TIGEM, Naples). For i.v. injections, P1 pups were injected with 10^{11} viral particles into the temporal vein, using a 31G, 30° beveled needle syringe. For i.c.v. injections, P1 pups were injected with 10^{10} viral particles into one lateral ventricle, located 1 mm lateral to the superior sagittal sinus and 2 mm rostral to the transverse sinus, to a depth of 2mm using an electrophysiology glass capillary connected to a sterile syringe.

2.1.4. Histological analysis

2.1.4.1. Tissue preparation and processing

Mice were sacrificed by cervical dislocation at the indicated age. The organs were quickly dissected and samples for histological analysis were taken. Brain, liver, kidney, and heart samples were placed in formaldehyde, in the form of 10% neutral buffered formalin (NBF), which is the most commonly used fixative for histopathological analysis. NBF guarantees preservation of tissue and cellular morphology, hardening of the samples for posterior processing, inactivation of proteolytic enzymes and protection of the samples against contamination and decomposition. After a few days of fixation, tissues were processed with a Leica ASP300S tissue processor, using either the “Small” (Table 2.1) or “Biopsy” (Table 2.2) protocol, and infiltrated with Tissue Infiltration Medium paraffin (Leica). All the sections were cut on a Leica RM2245 semi-automated rotary microtome to a thickness of 4 µm for all the stains except for Pathogreen (8 µm). After drying the sections were stained with haematoxylin and eosin (H&E), Pathogreen, or were subjected to immunohistochemistry (IHC) as detailed below. Skeletal muscle samples were frozen by immersion in isopentane cooled in liquid nitrogen to -160 °C. Cryostat frozen sections are necessary for skeletal muscle samples to assess the pattern and distribution of muscle enzymes and components which are destroyed by formalin fixation and paraffin processing. The isopentane is first frozen in a small glass beaker immersed in liquid nitrogen until it is completely solid. It is then allowed to warm to a point when there is liquid and solid together. The specimen is then submerged into the liquid phase of the isopentane. The duration of the freezing depends on the size of the specimen; usually 15 seconds is sufficient. The frozen samples are then mounted on a metal specimen disk with Tissue-Tek O.C.T. Compound, and sectioned at 8 µm in a cryostat at -20 °C. These sections are then stained with H&E or subjected to COX or SDH staining, as detailed below.

Table 2.1 “Small” protocol for the Leica ASP300S tissue processor.

Step	Solution	Cycle (Time in minutes)	Temperature	Pressure/Vacuum
1	70% Ethanol	30	RT	Yes
2	80% Ethanol	30	RT	Yes
3	95% Ethanol	30	RT	Yes
4	95% Ethanol	30	RT	Yes
5	100% Ethanol	30	RT	Yes
6	100% Ethanol	30	RT	Yes
7	100% Ethanol	30	RT	Yes
8	Xylene	30	RT	Yes
9	Xylene	60	RT	Yes
10	Paraffin	30	60 °C	Yes
11	Paraffin	30	60 °C	Yes
12	Paraffin	60	60 °C	Yes

Table 2.2 “Biopsy” protocol for the Leica ASP300S tissue processor.

Step	Solution	Cycle (Time in minutes)	Temperature	Pressure/Vacuum
1	70% Ethanol	10	RT	No
2	80% Ethanol	15	RT	No
3	95% Ethanol	15	RT	No
4	95% Ethanol	15	RT	No
5	100% Ethanol	15	RT	No
6	100% Ethanol	15	RT	No
7	Xylene	10	RT	No
8	Xylene	10	RT	No
9	Xylene	10	RT	No
10	Paraffin	15	60 °C	Yes
11	Paraffin	15	60 °C	Yes
12	Paraffin	15	60 °C	Yes

2.1.4.2. Haematoxylin and eosin (H&E) staining

H&E staining is one of the most widely used histological stain, which clearly shows the overall structure of the tissue. It is simple to use, easy to automate and demonstrates different tissue structures clearly. Haematoxylin stains the cell nuclei in purple, showing clear intranuclear detail, while eosin stains cell cytoplasm and most connective tissue fibers in varying shades and intensity of pink.

2.1.4.2.1. H&E staining protocol for formalin-fixed paraffin-embedded (FFPE) tissue sections

FFPE sections were deparaffinized, hydrated, stained in Mayer’s haematoxylin (Sigma Aldrich) for 15 min, washed with tap water for 3 min, and then stained with eosin-Y solution 1%, alcoholic (Leica) for 1 min. Sections were briefly washed with distilled water, differentiated in 95% ethanol for 1 min (2 changes), dehydrated in absolute ethanol, cleared in xylene, and mounted with Cytoseal 60 (Thermoscientific).

2.1.4.2.2. H&E staining protocol for frozen tissue sections

Sections were stained with Mayer’s haematoxylin for 5 min, rinsed in tap water for 3 min, and then transferred in eosin-Y solution 1%, alcoholic for 15 sec. Sections were then briefly washed with distilled water, differentiated in 95% ethanol and dehydrated in absolute ethanol. Finally, sections were cleared in xylene and mounted with Cytoseal 60.

2.1.4.3. Pathogreen staining

Pathogreen stain^{TM} (Biotium, 80027) is an anionic green fluorescent dye that stain degenerating neurons by an unknown mechanism similarly to Fluoro-Jade. 8-µm-thick FFPE sections were brought to water, incubated with 0.06% potassium permanganate solution for 10 min, rinsed twice with distilled water and further incubated in distilled water for 2 min. Sections were then incubated for 10 min in 1X Pathogreen staining solution, obtained by diluting the stock solution 1:1000 in 0.1% acetic acid in distilled water, rinsed 3 times for 1 min each with distilled water, and then air-dried on a slide warmer at 50 °C for at least 5 min. Finally, sections were cleared in xylene and mounted with Cytoseal 60.

2.1.4.4. Immunohistochemistry (IHC)

Immunohistochemistry was performed on 4-µm-thick FFPE sections using the Novolink Polymer Detection System (Leica, RE7140-K), following the manufacturer’s instructions. Sections were deparaffinized with xylene and then hydrated through graded alcohols. Heat-induced epitope retrieval (HIER) was performed in a microwave to expose the antigenic sites and allow the binding of the primary antibody. The slides were washed with distilled water and endogenous peroxidase activity was neutralized with Peroxidase Block for 5 min. Then, the slides were washed once with PBS and incubated in Protein Block for 5 min. The sections were washed again with PBS and incubated with the primary antibody for 30 mins at room temperature (RT). A list of the primary antibodies and dilution are presented in Table 2.3. After incubation the slides were washed once with 50 mM Tris-HCl pH 7.6 added with 300 mM NaCl, 0.1% Tween-20 (T-TBS), and then incubated with Post Primary for 30 min at RT. The sections were washed again with T-TBS and incubated with Novolink Polymer for 30 min at RT. After a final washing step with T-TBS the sections were incubated with DAB working solution to produce a brown precipitate at the antigen site. The slides were rinsed with distilled water, dehydrated, cleared, and mounted.

Table 2.3 Antibodies used for immunohistochemistry

Antigen	Host	Dilution	Manufacturer (code number)
CD68	Rabbit	1:2000	Abcam (ab283654)
GFAP	Mouse	1:1000	Sigma Aldrich (G 3893)
Cleaved caspase-3	Rabbit	1:200	Cell Signaling (9661)
NDUFS4	Rabbit	1:600	Novus Biologicals (NBP1-31465)

2.1.4.5. Cytochrome c oxidase (COX) staining

Histochemical staining of COX activity was performed on 8-µm-thick cryostat sections of skeletal muscle, using diaminobenzidine (DAB) as an electron donor to produce a brown end product. Sections were incubated for 1 h at 37 °C in incubating medium [5 mM DAB and 100 µM cytochrome c in 100 mM phosphate buffer (pH 7.0)], rinsed in tap water, dehydrated in ascending alcohol series, cleared and mounted in synthetic resin.

2.1.4.6. Succinate dehydrogenase staining

SDH staining was performed on 8-µm-thick cryostat sections of skeletal muscle, using nitroblue tetrazolium (NBT) as an electron acceptor which is reduced to a bluish insoluble formazan product at the site of enzyme activity. The staining reaction is accelerated by the presence of phenazine methosulfate (PMS). Sections were incubated for 30 minutes at 37 °C in incubating medium [130 mM sodium succinate, 2 mM NBT, 0.2 mM PMS and 1 mM sodium azide in 100 mM phosphate buffer (pH 7.0)]. At the end of incubation, sections were washed with tap water, dehydrated in ascending alcohol series, cleared and mounted in synthetic resin.

2.1.4.7. Modified Gomori trichrome

It is an excellent stain used for striated muscle and peripheral nerve. Due to the differences in sarcoplasmic and pathological inclusion staining, architectural changes in muscle fibers, such as nemaline rods or "ragged red" fiber change, are easily visible. 8-µm-thick cryostat sections of skeletal muscle were stained in Harris' haematoxylin for 5 minutes, rinsed in distilled water, and then incubated in Gomori trichrome solution (Table 2.4) for 20 minutes. Sections were then rinsed in tap water, dehydrated rapidly in ascending alcohol series, cleared, and mounted in synthetic resin.

Table 2.4 Gomori trichrome solution

Chromotrope 2R	0.6 g
Fast green FCF	0.3 g
Phosphotungstic acid	0.6 g
Glacial acetic acid	1.0 mL
Distilled water	100 mL
Adjust to pH 3.4	

2.2. Nucleic acid-based methods

2.2.1. DNA extraction from mouse tissues

Genomic DNA was extracted by re-suspending frozen mouse tissue samples in 400 µl of DNA lysis buffer [0.5% sodium dodecyl sulfate (SDS), 100 mM NaCl, 2.5 mM EDTA, 20 ng/µl Proteinase K in 50 mM Tris-HCl (pH 8.0)]. Samples were then incubated ON at 56 °C, shaking at 300 RPM. The following day, one volume of chloroform and 0.6 M potassium acetate were added to the tube and mixed vigorously. The resulting mixture was centrifuged at 21,000 g for 10 min at 4 °C. The upper aqueous phase was transferred to a new tube, followed by ethanol precipitation with 1 ml of 95% ethanol. The tubes were centrifuged at 21,000 g for 10 min at 4 °C and the supernatant was discarded. The pellet was washed with 70% ethanol and centrifuged again at 21,000 g for 10 min at 4 °C. Subsequently, the supernatant was discarded, the pellet air-dried and finally resuspended in nuclease-free water. DNA concentration was measured by NanoDrop^{TM} 2000 spectrophotometer (ThermoScientific) at a wavelength of 260 nm.

2.2.2. Polymerase chain reaction (PCR) associated procedures

The PCR reactions were performed using a SimpliAmp Thermal Cycler (Applied Biosystems) with *Taq* polymerase to amplify the DNA sequence of interest by multiple cycles of three temperature-mediated steps: 1) denaturation of the double-stranded template DNA by heat; 2) annealing of two synthetic oligonucleotide primers to the denatured template DNA; 3) extension, in which DNA synthesis is initiated at the 3’ ends of the bound primers in an enzymatic reaction catalyzed by the *Taq* polymerase. The primer sequences and corresponding cycling programmes are specified in the individual sections.

2.2.2.1. Design and synthesis of oligonucleotide primers

The PCR primers used in this study were designed using the web-based software Primer3Plus (www.bioinformatics.nl/cgi-bin/primer3plus/primer3plus.cgi).

The parameters applied are:

- Primer length between 18 and 27 nucleotides, with 20 nucleotides as optimal.
- Primer GC% between 40 and 60 %.
- Primer T_m between 57.0 and 63.0 °C, with 60.0 °C as optimal.

Each newly designed primer pair was tested for specificity using the NCBI tool Primer Blast (www.ncbi.nlm.nih.gov/tools/primer-blast/index.cgi).

The oligonucleotide primers were ordered from BMR Genomics, delivered dry and desalted and resuspended to a stock concentration of 100 µM with nuclease-free water.

2.2.2.2. Agarose gel electrophoresis

Analysis of the DNA products from PCR amplification was performed by separating the DNA fragments by agarose gel electrophoresis according to their size. Unless otherwise specified, 1% agarose gels were utilized for general applications. Gels were cast with the appropriate weight per volume (w/v) of agarose (ThermoFisher), tipically 1% gel: 0.70 g of agarose dissolved in 70 ml of 1 x TBE [89 mM tris base, 89 mM boric acid, 2 mM EDTA (pH 8.0)]. To the gel solution, 7.0 µl of 10,000 X SYBR Safe dye (ThermoFisher) were added to allow visualization with an ultraviolet (UV) light transilluminator after the run. A 1kb Plus DNA ladder (ThermoFisher) was used as standard for fragment size determination, and samples were electrophoresed at 90 V (EM100, Mini Gel Unit, Engineering & Design Plastics, UK) with 1x TBE as the running buffer.

2.2.2.3. Genotyping of the *Polg* Y933C allele

Genomic DNA extracted from ear biopsies was used to genotype individual mice. PCR was performed in 25 µl containing: 25-50 ng of DNA, 0.2 mM of each dNTP, 1.25 U of GoTaq polymerase (Promega), 1X Green GoTaq Buffer and 0.25 µM of each primer (Polg_Y933C_Fw: 5'-GCCTTTGGCTGGATGACTCT-3'; Polg_Y933C_Rv: 5'-CAGCGCCTGTCTATCTGCTT-3'). PCR conditions are listed in Table 2.5.

Table 2.5 PCR condition of the *Polg* Y933C allele

Temperature	Duration	Cycle number
95 °C	3 min	1
95 °C	30 sec	35
61 °C	30 sec	
72 °C	30 sec	
72 °C	5 min	1
4 °C	∞	

At the end of the PCR reaction, 1 U of MscI (restriction site next to the Knockin allele) was added together with 1 X CutSmart® Buffer. The restriction reaction was incubated at 37 °C for at least 3 h. At the end of the reaction, samples (5 µl) were loaded directly into 1 % agarose gel and run as described in Section 2.2.2.2.

The expected PCR products after MscI digestion are:

1) Two WT alleles: 561 bp
2) One WT allele and one Y933C allele: 131 bp + 430 bp + 561 bp
3) Two Y933C alleles: 131 bp + 430 bp

2.2.2.4. Genotyping of the *Ndufs4* KO allele

Genomic DNA extracted from ear biopsies was used to genotype individual mice. PCR was performed in 20 µl containing: 25-50 ng of DNA, 5% DMSO, 1X Platinum™ Direct PCR Universal Master Mix (ThermoFisher) and 0.25 µM of each primer (WT allele: NDUFS4_Fw: 5’-AGCCTGTTCTCATACCTCGG-3’, NDUFS4_Rv1: 5’-GCTCTCTATGAGGGTACAGAG-3’; KO allele: NDUFS4_Fw: 5’-AGCCTGTTCTCATACCTCGG-3’, NDUFS4-Rv2: 5’-GGTGCATACTTATACTACTAGTAG-3’). PCR conditions are listed in Table 2.6.

Table 2.6 PCR conditions for the *Ndufs4* mouse genotyping

Temperature	Duration	Cycle number
95 °C	3 min	1
95 °C	30 sec	35
53 °C	30 sec	
72 °C	30 sec	
72 °C	5	1
4 °C	∞	

At the end of the PCR, samples (5 µl) were loaded directly into 1 % agarose gel and run as described in Section 2.2.2.2.

The expected PCR products are:

1) Two WT alleles: 160 bp
2) One WT allele and one KO allele: 160 bp + 260 bp
3) Two KO alleles: 260 bp

2.2.2.5. Long-range PCR for the detection of mtDNA deletions

Genomic DNA extracted from mouse tissues was used. PCR was performed in 25 µl containing: 50 ng of DNA, 0.2 mM of each dNTP, 1 U of PrimeSTAR GXL DNA polymerase (TAKARA), 1X GXL buffer and 0.25 µM of each primer (LongR_mtDNA_Fw: 5’-GAGGTGATGTTTTTGGTAAACAGGCGGGGT-3’, LongR_mtDNA_Rv: 5’-GGTTCGTTTGTTCAACGATTAAAGTCCTACGTG-3’). PCR conditions are listed in Table 2.7

Table 2.7 PCR conditions of the Long-Range PCR

Temperature	Duration	Cycle number
98 °C	3 min	1
98 °C	10 sec	35
68 °C	13 min	
72 °C	5 min	
4 °C	∞	

At the end of the PCR reaction, samples (10 µl) were mixed with 6X DNA loading dye (Promega) and loaded into 0.8 % agarose gel and run in 1X TBE buffer at constant 60 V for 3 h. This primer set anneal tail-to-tail in the mouse 16S gene and generates an expected band of 15,781 bp covering almost the entire mouse mtDNA.

2.2.2.6. Real-time quantitative PCR (qPCR)

All real-time qPCR reactions were performed in individual wells of a 384-well plate, that was sealed and loaded into a QuantStudio^{TM} 5 Real-Time PCR system (Applied Biosystems).

2.2.2.6.1. mtDNA copy number

Real-time qPCR was used to determine the relative mtDNA copy number in different mouse tissues. SYBR Green technology was used for relative quantification of mtDNA. SYBR Green emits fluorescence when bound to dsDNA, so after each cycle of PCR, the amount of SYBR Green correlates with the amount of DNA. Setting the threshold determines the level of fluorescence signal that is above the background to be considered a reliable signal. The cycle at which the threshold is met is called the cycle threshold (Ct) and is used for the calculation of the relative gene copy number or gene expression, using the 2^$^{-\Delta\Delta Ct}$ method.

mtDNA relative quantification was performed using primers specific to a mouse mtDNA region in the *COI* gene and primers specific to *RNase P*, a single copy gene taken as a nuclear gene reference.

Each sample was run in three technical replicates and each reaction was performed in 10 µl containing: 30 ng of DNA, 1X GoTaq® qPCR Master Mix (Promega) and 0.25 µM of each primer (*COI*: mCoI_Fw: 5'-TGCTAGCCGCAGGCATTACT-3', mCOI_Rv: 5'-CGGGATCAAAGAAAGTTGTGTTT-3'; *RNase P*: mRNaseP_Fw: 5'-GCCTACACTGGAGTCGTGCTACT-3', mRNaseP_Rv: 5'-GCCTACACTGGAGTCGTGCTACT-3', mRNaseP_Rv: 5'-CTGACCACACGAGCTGGTAGAA-3'). PCR conditions are listed in Table 2.8.

Table 2.8. qPCR conditions of mtDNA relative quantification

Temperature	Duration	Cycle number
95 °C	2 min	1
95 °C	15 sec	40
60 °C	1 min	

The Ct values for each sample were used to calculate the relative mtDNA copy number using the 2^-$^{\Delta\Delta Ct}$ method, as detailed in "Livak and Schmittgen, 2011".

2.2.2.6.2. Viral genome copies

Real-time qPCR was used to determine the viral genome copies of scAAV9-h*NDUFS4* in the different tissue of injected mice. The SYBR Green technology was used as described in Section 2.2.2.5.1 but the data analysis was performed differently. Quantification of viral genome copies was performed using a pair of NDUFS4 primers that anneal to both human and mouse *NDUFS4*. The *RNase P* gene was used as a reference. Each sample was run in three technical replicates and each reaction was performed in 10 µl containing: 30 ng of DNA, 1X GoTaq® qPCR Master Mix (Promega) and 0.25 µM of each primer (NDUFS4: hm_NDUFS4_Fw: 5'-CTTTGTTCCTGCTCGCAATA-3', hm-NDUFS4_Rv: 5'-

ATGCCCAACCCATCAAAG-3’; RNase P: mRNaseP_Fw: 5’-GCCTACACTGGAGTCGTGCTACT-3’, mRNaseP_Rv: 5’-CTGACCACACGAGCTGGTAGAA-3’). Real-time qPCR conditions are in Table 2.9.

Table 2.9 qPCR conditions for viral genome quantification

Temperature	Duration	Cycle number
95 °C	2 min	1
95 °C	15 sec	40
60 °C	1 min	

NDUFS4 Ct values were first normalized using RNAse P Ct values to account for variations in DNA input. Because the NDUFS4 primers anneal to both the AAV vector and mouse DNA, untreated mice were used to extrapolate the Ct value corresponding to 2 copies of NDUFS4 per nucleus. Therefore, the viral genome copies were calculated as $2 \times 2^{-\Delta Ct}$, where ΔCt corresponds to the difference between the Ct values of injected mice minus the Ct values of the untreated mice.

2.3. Protein-based methods

2.3.1. Determination of protein concentration

Protein concentrations of whole cell lysates from mouse tissues were estimated using a modified version of the Lowry protein assay, DC™ Protein Assay (Bio-Rad), according to the manufacturer’s instructions. The absorbance of protein samples of unknown concentrations and five BSA standards with concentrations ranging from 0 to 1.5 mg/ml was measured using a Varioskan™ LUX multimode microplate reader (ThermoFisher) at a wavelength of 750 nm. The known BSA standards were used to generate a calibration curve that was used to extrapolate the unknown protein concentrations based on their absorbance values.

2.3.2. Sodium Dodecyl Sulfate Polyacrylamide Gel Electrophoresis (SDS-PAGE)

Frozen mouse tissues (about 50 mg) were homogenized in 10 volumes of phosphate buffer [10 mM potassium phosphate, pH 7.4, 1X cOmplete^{TM} mini EDTA-free Protease Inhibitor Cocktail (Roche)] using a Potter Tissue Homogenizer (Vetrotecnica). Mitochondrial-enriched fractions were collected after centrifugation at 800 g for 10 min, and frozen and thawed three times in liquid nitrogen. Protein concentration was determined as described in Section 2.3.1. Samples were stored at -20 °C until use. Protein lysates (10 – 40 µg) were mixed with 10X NuPAGE^{TM} sample reducing agent and 4X NuPAGE^{TM} LDS sample buffer (ThermoFisher) and incubated for 5 min at 95 °C (or 10 min at RT when analysing proteins of the MRC). Protein samples were loaded and separated under denaturing conditions by SDS-PAGE using 4-12% gradient precast polyacrylamide NuPAGE® Bis-Tris gels (ThermoFisher). The NuPAGE® MOPS SDS Running Buffer (1X: 50 mM MOPS, 50 mM Tris base, 0.1% SDS, 1 mM EDTA, pH 7.7) was used in all applications (ThermoFisher). Gels were run at 130V for 1-2 h at 4 °C, with 5 µl PageRuler^{TM} Plus Prestained Protein Ladder, 10 to 250 kDa (ThermoFisher) in one of the lanes for size comparison.

2.3.3. Blue Native Gel Electrophoresis (BNGE)

Frozen mouse brain tissues (about 50 mg) were homogenised in 10 volumes of Medium A (320 mM sucrose, 1mM EDTA, 10mM Tris-HCl, pH 7.4) in a Potter Elvehjem homogeniser using a teflon pestle. Homogenates were centrifuged (800 g for 5 min at 4 °C) to remove nuclei and cell debris. The resulting supernatant was collected and centrifuged (9,000 g for 10 minutes at 4 °C) to obtain an enriched mitochondrial fraction. The pellet was then resuspended in 1 ml of Medium A and an aliquot of 5 µl was taken for determination of protein concentration (see Section 2.3.1). The samples were then centrifuged (9,000 g for 5 minutes at 4 °C) and the pellet was resuspended in the appropriated amount of solubilisation buffer (1.5 M aminocaproic acid, 50 mM Bis-Tris/HCl, pH 7.0) to obtain a protein concentration of 10 mg/ml. Samples were solubilized with 4 mg of n-dodecyl β-D-maltoside (Sigma-Aldrich) per mg of protein, incubated on ice for 5 min and centrifuged (18,000 g for 10 minutes at 4 °C). The supernatant was collected and mixed with sample buffer (750 mM aminocaproic acid, 50 mM Bis–Tris/HCl pH 7.0, 0.5 mM EDTA and 5% Serva Blue G-250). BNGE protein samples (30 µg) were loaded and separated under non-denaturing conditions and run through a 3-12 % Native-PAGE gel (NativePAGE^{TM} 3 to 12%, BIS-TRIS, Mini Protein Gels, ThermoFisher). Initially the gel was run for 1 h at 150 V in Cathode Buffer A (50 mM tricine, 15 mM BIS-TRIS, pH 7.0, 0.02% Coomassie G-250), and further run for 1-2 h at 200 V (~8 mA) in Cathode Buffer B (50 mM tricine, 15 mM BIS-TRIS, pH 7.0, 0.002% Coomassie G-250). The Anode Buffer (50 mM tricine, 15 mM BIS-TRIS, pH 7.0) was used in all applications.

2.3.4. Western blotting

Proteins separated by both SDS-PAGE and BN-PAGE were electroblotted onto methanol-activated PVDF membranes (PVDF Transfer Membrane, ThermoFisher) using a wet transfer system (Mini Trans-Blot® Cell Module, Bio-Rad). Transfer of SDS-PAGE was performed at 4 °C and 100 V for 1 h in transfer buffer (25 mM Tris-HCl, 192 mM Glycine, 20 % methanol and 0.025 % SDS). Blotting of BN-PAGE was performed at 4 °C and 300 mA for 1 h in bicarbonate transfer buffer (10 mM $NaHCO_3$, 3 mM Na_2CO_3).

2.3.5. Immunodetection

PVDF membranes were blocked with 5% milk in PBS containing 0.1% Tween 20 (PBS-T) for 1 h at RT with shaking and then incubated overnight with specific primary antibodies in 5% milk in PBS-T at 4°C (Table 2.10). After incubation with the primary antibody, the membranes were washed three times with PBS-T (10 min at RT) with shaking. The membranes were then incubated with horseradish peroxidase (HRP)-conjugated anti-rabbit, anti-mouse, or anti-goat (Promega, catalogue number: W4011 [rabbit], W4021 [mouse] and V8051 [goat]) IgG secondary antibodies at a dilution of 1:3000, respective to the used primary antibody). Three additional washes in PBS-T were performed (10 min at RT) and then membranes were developed by incubation with SuperSignal^{TM} West Pico PLUS Chemiluminescent Substrate (ThermoFisher), according to the manufacturer's instructions. Developed membranes were imaged using the Nine Alliance Q9 Atom Advanced imaging system (Uvitec). Bands were quantified using the Fiji software.

Table 2.10 Primary antibodies used for immunodetection

Antigen	Host	Dilution	Manufacturer (CN)
NDUFS4	Rabbit	1:1000	Novus Biologicals (NBP1-31465)
NDUFA9	Mouse	1:1000	Abcam (ab14713)
POLγA	Goat	1:500	Santa Cruz (sc-5931)
POLγB	Rabbit	1:500	Novus (NBP2-94064)
TFAM	Rabbit	1:2000	Abcam (ab131607)
GAPDH	Mouse	1:5000	GeneTex (GTX627408)
SDHB	Mouse	1:1000	Abcam (ab14714)
β-tubulin	Rabbit	1:3000	Proteintech (10094-1-AP)

2.4. Mitochondrial respiratory chain functional assays

2.4.1. Mitochondrial respiratory chain complex enzymatic activity

The activities of respiratory chain complexes and citrate synthase (CS) were measured spectrophotometrically in mouse tissue samples. Frozen mouse tissues (20-30 mg) were homogenized in 10 volumes of Medium A (10 mM Tris-HCl, pH 7.4, 320 mM sucrose, 1 mM EDTA) using a Potter tissue homogenizer with a Teflon pestle. Homogenates were centrifuged (800 g for 5 min at 4 °C) and the crude mitochondria-enriched supernatants were snap frozen immediately in liquid nitrogen. Samples were stored at -80°C until use. On the day of the experiment, the mitochondrial-enriched homogenates were first thawed on ice and then snap-frozen and rapidly thawed between liquid nitrogen and a 37 °C water bath for three consecutive freeze-thaw cycles. Protein concentration was determined as described in Section 2.3.1 and samples were loaded into individual wells of a 96-well plate and placed on ice. The spectrophotometric activity of CI, CIV, and CS, was measured as described in (Bugiani et al., 2004). The protein concentration and path length per 200 µl of reaction were used to calculate the specific biochemical activities of each sample using the Beer-Lambert law: A=εlc (A=absorbance, ε=molar absorption coefficient, l=optical path length, c=molar concentration).

$$\text{Specific activity=} \frac{\Delta\text{Abs x total reaction volume (ml)}}{\varepsilon \text{ x sample volume (ml) x [prot] (mgml}^{-1}\text{) x l (cm)}}$$

The specific activities of CI and CIV were each normalised against the relative activity of CS. Technical replicates (at least 3) were performed per sample using the same reaction buffer.

2.4.1.1. Complex I

CI activities were measured in tissue homogenates by following the decrease in absorbance due to the oxidation of NADH at 340 nm ($\varepsilon_{NADH340nm}$=6.81 $mM^{-1}cm^{-1}$).

Tissue homogenate samples were incubated in a reaction mix (20 mM potassium phosphate pH 8.0, 0.2 mM NADH, 1 mM sodium azide, 0.1% BSA, 1 mM EDTA Na_4 pH 7.4) at 30 °C for 10 min and then the absorbance change was recorded for two mins to ensure that the baseline was stable. The reaction was primed with 50 μM CoQ, followed for 2 min, and then inhibited with the CI-inhibitor rotenone (5 μM). Specific CI activity was obtained by subtracting the activity in presence of rotenone from total activity.

2.4.1.2. Complex IV

Complex IV activity was measured by following the decrease in absorbance at 550 nm due to the oxidation of cytochrome c ($\varepsilon_{cytc550nm}$=18.5 $mM^{-1}cm^{-1}$). The reaction mix [50 mM potassium phosphate pH 7.0, 100 μM cytochrome c (90-95% reduced)] was equilibrated at 37 °C for 3 min, and the reaction was started by the addition of the homogenate sample. The decrease of absorbance was followed at 550 nm for 2 min.

2.4.1.3. Citrate synthase

The citrate synthase assay monitors the production rate of coenzyme A from oxalacetate by measuring free sulfhydryl groups using the thiol reagent 5,5'-dithio-bis-(2-nitrobenzoic acid) (DTNB). DTNB reacts with sulfhydryl groups to produce free 5-thio-2-nitrobenzoate anions (TNB), which are yellow in colour. Citrate synthase specific activity is measured by following the increase in absorbance due to the formation of the 5-thio-2-nitrobenzoate anion at 412 nm ($\varepsilon_{TNB412nm}$=13.8 $mM^{-1}cm^{-1}$). Tissue homogenate samples were incubated in a reaction mix (75 mM Tris-HCl pH 8.0, 0.1 mM DTNB, 0.1% Triton X-100, 0.4 mM Acetyl-CoA) at 30 °C for 2 min. The reaction was primed with oxalacetate (0.5 mM), and the increase of absorbance was followed at 412 nm for 2 min.

2.4.2. In-Gel Activity (IGA)

In-gel activity was performed on BNGE samples, prepared as described in Section 2.3.3. Gels were briefly rinsed in water and then incubated 2 h at RT while gently shaking in 10 ml of CI detection solution [0.1 M Tris-HCl pH 7.4, 0.14 mM NADH, 1 mg/ml Nitro Blue Tetrazolium (NBT, Sigma-Aldrich)]. After incubation, gels were washed with water and digitally scanned with a professional scanner (EPSON Expression 1680 Pro, EPSON).

2.5. *In vitro* assays with recombinant proteins

The *in vitro* assays with purified recombinant proteins presented in this work were carried out by Dr. Louise Jenninger of Maria Falkenberg's lab at the Department of Medical Biochemistry and Cell Biology at the University of Gothenburg.

2.5.1. Expression and purification of recombinant proteins

Human and mouse POLγA versions (lacking the mitochondrial targeting sequence aa 1–25) and human and mouse POLγB (lacking the mitochondrial targeting sequence aa 1–24 and aa 1–16, respectively) were cloned into a pBacPAK9 vector, with a cleavable 6xHisTag in the N-terminus. *Autographa californica* nuclear polyhedrosis virus recombinant for the individual proteins were prepared as described in the BacPAK manual (Clontech).

For protein expression, Sf9 cells were grown in suspension, harvested by centrifugation (60-72 h after infection), frozen in liquid nitrogen, thawed and lysed at 4 °C in lysis buffer [25 mM Tris-HCl pH 8.0, 0.8 M NaCl, 10 mM β-mercaptoethanol and 1x protease inhibitors (1 mM PMSF, 2 mM pepstatin, 0.6 mM leupeptin and 2 mM benzamidine in 100% ethanol)]. The cellular suspension was homogenized using an Ultra-Turrax T3 homogenizer (IKA) and centrifuged at 20,000 g for 45 min in a JA-25.50 rotor (Beckman Coulter). The supernatant was loaded onto His-Select Nickel Affinity Gel (Sigma-Aldrich) equilibrated with buffer A (25 mM Tris–HCl, pH 8.0, 0.4 M NaCl, 10% glycerol and 10 mM β-mercaptoethanol). The protein was eluted with buffer A containing 250 mM imidazole. Removal of the 6×HisTag was achieved by overnight dialysis in presence of ≈0.5 mg TEV in buffer A. An additional Nickel purification step was performed to get rid of uncut His tagged protein and TEV. The protein was subsequently purified over a 5-ml HiTrap Heparin HP column (GE Healthcare) and a 1-ml HiTrap Q HP column (GE Healthcare), both equilibrated in buffer B (25 mM Tris–HCl pH 8.0, 10% glycerol and 1 mM DTT) containing 0.2 M NaCl, followed by elution driven by a linear gradient (50 and 10 ml, respectively) of buffer B containing 1.2 M NaCl (0.2–1.2 M NaCl). POLγA was subjected to an additional step of purification over a 1-ml HiTrap SP HP column. The column was equilibrated with buffer B containing 0.1 M NaCl and eluted with a linear gradient (10 ml) of buffer B containing 1.2 M NaCl (0.1–1.2 M NaCl). For POLγB, an additional step of purification with a 1-ml HiTrap Talon column (GE Healthcare) was used in between HiTrap Heparin HP (GE Healthcare) and HiTrap SP HP (GE Healthcare).

This column was equilibrated with buffer C (25 mM Hepes pH 6.8, 10% glycerol, 0.4 M NaCl, 1 mM β-mercaptoethanol) containing 5 mM imidazole and elution driven by a linear gradient (10 ml) of buffer C containing 150 mM imidazole (5–150 mM imidazole). Protein purity was checked on a precast 4–20% gradient SDS-PAGE gel (BioRad, 567–8094) and pure fractions were aliquoted and stored at −80 °C.

For the generation of mutant version of POLγA, QuikChange Lightning Site-Directed Mutagenesis Kit (Agilent, #210519) was used according to manufacturer's instructions.

2.5.2. Electrophoretic Mobility Shift Assay (EMSA)

DNA binding affinity of POLγ holoenzyme (POLγA-B2) to a primer-template was assessed using a 36-nucleotide (nt) oligonucleotide [5'-TTTTTTTTTTATCCGGGCTCCTCTAGACTCGACCGC-3'] annealed to a ^{32}P 5'-labeled 21-nt complementary oligonucleotide (5'-GCGGTCGAGTCTAGAGGAGCC-3'). This produces a primed-template with a 15 bases single-stranded 5'-tail. The reactions were performed in 15 µl volumes containing 10 fmol DNA template, 25 mM Tris–HCl pH 8.0, 1 mM TCEP, 0.1 mg/ml bovine serum albumin, 10% glycerol, and 100 µM ddCTP. POLγA-B2 was added as indicated in the figure and reactions were incubated on ice for 10 min followed by 10 mins at RT before being separated on a 6% Native PAGE gel in 0.5× TBE for 25 min at 180 V. The resulting bands were visualised using autoradiography. To analyze the binding affinity (Kd), the intensities of bands representing unbound and bound DNA were quantified using Multi Gauge V3.0 software (Fujifilm Life Sciences). The fraction of bound DNA was determined from the background-subtracted signal intensities using the expression: bound/(bound+unbound). The fraction of DNA bound in each reaction was plotted versus the concentration of POLγA-B2. Data were fit using the 'one site – specific binding' algorithm in Prism 8 (Graphpad Software) to obtain values for Kd. Each Kd value is shown as an average of three independent reactions.

2.5.3. *In vitro* DNA replication on a circular single-stranded template

A 32P 5′-labeled 32-mer oligonucleotide [5′-CTATCTCAGCGATCTGTCTATTTCGTTCATCC-3′] was hybridized to a single-stranded pBluescript SK(+) O_L plasmid. Reactions were carried out in 25 µl volumes containing 10 fmol template DNA, 25 mM HEPES pH 7.6, 1 mM DTT, 10 mM $MgCl_2$, 0.1 mg/ml BSA, 3 pmol mtSSB (tetrameric), and 100 fmol POLγA (WT or mutant) in complex with 200 fmol POLγB (dimeric). dNTPS were added at a concentration of either 1, 10, 30, or 100 mM. Reactions were incubated at 37 °C for 60 min and stopped by the addition of 5 µl of stop buffer (90 mM EDTA pH 8.0, 6% SDS, 30% glycerol, and 0.25% bromophenol blue). Products were analysed on 0.8% agarose gels in 1x TBE buffer and visualized by autoradiography.

2.5.4. *In vitro* DNA rolling circle replication assay

A 70-mer oligonucleotide [5′-42(T)-ATCTCAGCGATCTGTCTATTTCGTTCAT-3′] was hybridized to a single-stranded pBluescript SK(+) followed by one cycle of polymerization using KOD polymerase (Novagen) to produce a ∼4-kb double-stranded template with a preformed replication fork. Reactions of 25 µl were carried out containing 10 fmol template DNA, 25 mM HEPES pH 7.6, 1 mM DTT, 10 mM $MgCl_2$, 0.1 mg/ml BSA, 1 mM ATP, 10 µM dNTPs, 2 µCi [α-^{32}P] dCTP, 4 pmol mtSSB (tetrameric), and 200 fmol TWINKLE (hexameric). POLγA-B2 [75 fmol POLγA in complex with 150 fmol POLγB (dimeric) for WT (human or mouse) and mutant (Y955C or Y933C) alone; 75 fmol POLγA^{WT} with 75, 150, 225 or 375 fmol of mutant POLγA (Y955C or Y933C) in complex with 300, 450, 600 or 900 fmol POLγB (dimeric) for WT (human or mouse) and mutant (Y955C or Y933C) mixes (ratio 1:1, 1:2, 1:3, 1:5)] was added as indicated in the figure. Reactions were incubated for 30, 60 and 90 minutes at 37 °C and stopped with 8 µl of alkaline loading buffer (18% w/v Ficoll, 300 mM NaOH, 60 mM EDTA pH8.0, 0.25% w/v bromophenol blue and 0.25% w/v xylene cyanol). Products were run in 0.8% alkaline agarose gels and visualized by autoradiography. Incorporation of [α-^{32}P]-dCTP was measured by spotting 5 µl aliquots of the reaction mixture (after the indicated time points at 37°C) on Hybond N+ membrane strips (GE Healthcare Lifesciences). The membranes were washed (3× with 2× SSC and 1× with 95% EtOH) and the remaining activity was quantified using Multi Gauge V3.0 software (Fujifilm Life Sciences). A dilution series of known specific activity of [α-^{32}P]-dCTP was used as a standard.

2.6. Statistics

Data visualization and statistical analyses were performed using GraphPad Prism software (version 9.0). All numerical data are presented as mean with either standard error of the mean (SEM) or standard deviation (SD), as indicated in the respective figure legends. No preliminary tests were performed to assess the sample distribution, and it was assumed that all data followed a normal distribution. For comparisons between two groups, a two-tailed Student's t-test was employed, with specific details in the figure legend. Survival analysis was carried out using Kaplan-Meier distribution and a log rank test. The statistical procedures for each set of results will be specified in the text or figure legends. Statistically significant differences were denoted by * for $P < 0.05$, ** for $P < 0.01$,

*** for P < 0.005, and **** for P < 0.001. Animals were randomly assigned to treated and untreated groups, and no blinding was applied to the operator.

Chapter 3

Results

Gene therapy of a mouse model of Leigh syndrome by administration of a scAAV9-h*NDUFS4* viral vector

3. Gene therapy of a mouse model of Leigh syndrome by administration of a scAAV9-h*NDUFS4* viral vector

3.1. Introduction

Leigh syndrome (LS) is the most common mitochondrial disease of infancy. It is caused by mutations in more than 75 nuclear genes, with respiratory complex I (CI) defects being the most common cause (Rahman et al., 1996). It presents with feeding difficulties, hypotonia, abnormalities of motor coordination, posture and gait, vomiting, oculomotor abnormalities, blindness and optic atrophy, seizures, and psychomotor delay. In most of the cases, the disease leads to death within 1 to 2 years from onset. The condition is characterized by the presence of symmetrical spongy, necrotizing lesions that affect both the gray and the white matter. Currently, no curative therapy for LS is available. The clinical and neuropathological lesions of LS are mimicked by the *Ndufs4*$^{-/-}$ mouse model of LS which lacks a small, accessory but biochemically important subunit of NADH-binding (N) module of CI (NADH dehydrogenase ubiquinone iron-sulphur protein 4, *Ndufs4*).

Complex I, also known as NADH:ubiquinone oxidoreductase, is a key enzyme involved in cellular energy production and NAD$^+$ homeostasis. It plays a central role in OXPHOS, coupling NADH oxidation to ubiquinone reduction, leading to the generation of a proton gradient that drives ATP synthesis. Mammalian Complex I is composed of 45 subunits, including 14 conserved core subunits and 31 supernumerary subunits (Figure 3.1). The core subunits are essential for catalysis and are divided into hydrophilic and membrane-bound domains. The hydrophilic domain contains the NADH-dehydrogenase module (N-module), which is responsible for NADH oxidation, and the membrane-bound domain transport proton across the inner membrane. The presence of supernumerary subunits, such as NDUFS4, NDUFS6, NDUFA12, and NDUFAF2, is crucial for the stability and assembly for Complex I.

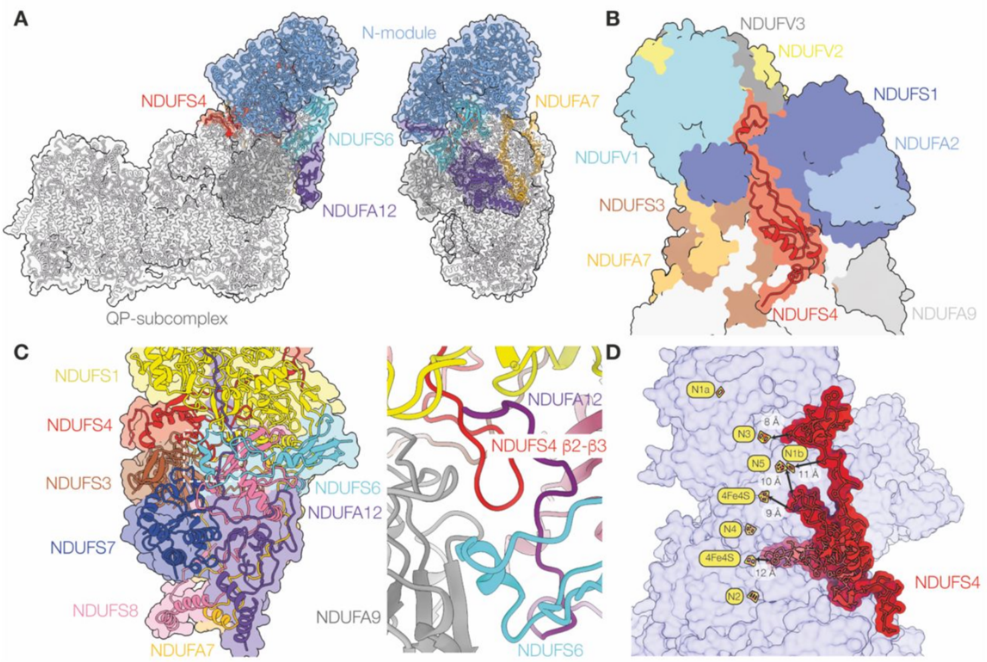

Figure 3.1. The NDUFS4 subunit in wild-type Complex I from mouse heart mitochondria. (A) Overview structures of Complex I viewed from the membrane and from the heel showing the locations of NDUFS4 (red), the N-module (blue) and subunits NDUFS6 (cyan), NDUFA12 (purple) and NDUFA7 (gold). (B) View of the front of the hydrophilic domain showing NDUFS4 (red) and the surrounding subunits. (C) Subunits surrounding NDUFA12 on the heel of the complex, and structural elements interacting with the β2-β3 loop of NDUFS4 that passes underneath NDUFS1 to form a junction of NDUSF4, NDUFA12, NDUFA6 and NDUF9 (right, close-up of the boxed region from a different viewpoint to focus on the loop). D) NDUFS4 approaches four of the seven FeS clusters in the FeS chain between the FMN and the ubiquinone-binding site (image from Yin et al., 2023).

In the absence of NDUFS4, the N-module of Complex I becomes loosely associated with the rest of enzyme, and the subunits NDUFA12 and NDUFS6 are absent. This results in a failure of proper Complex I assembly which leads to severe reduced levels of CI activity by spectrophotometric assay (Kruse et al., 2008). The *Ndufs4*$^{-/-}$ mice develop a post-weaning, early-onset multiple neurological decline characterized by severe ataxia, motor freezing and food avoidance. This decline is consistently preceded by coat loss, which occurs once, around 20 days after birth (Kruse et al., 2008). All mice die within two months after birth with a median survival of 45 days. In addition, histological analysis of the brain revealed progressive neuronal degeneration, gliosis, and activation of the microglia in specific regions of the brain, including early involvement of the olfactory bulb and vestibular nuclei (Quintana et al., 2010). Gene replacement therapy has been proposed as a therapeutic approach for patients suffering from mitochondrial disorders, particularly because of the encouraging advances of this field in the treatment of other non-mitochondrial disorders. Adeno-associated viral vectors (AAVs) are currently the leading platform for in vivo gene delivery to treat a variety of human diseases. They can infect both dividing and nondividing cells establishing long-term and efficient transgene expression with minimal toxicity and cellular immune response in many tissues. However, unlike other DNA-based viral and nonviral vectors such as adenoviruses and plasmids, AAV packages and delivers a single-stranded (ss) DNA genome that is transcriptionally inactive until it is converted into a double-stranded (ds) template. This process contributes in part to the delayed transduction and occasional inefficiency. In fact, the treatment of *Ndufs4*$^{-/-}$ animals with a single-stranded adeno-associated viral 9 (ssAAV9) recombinant vector expressing the human NDUFS4 gene resulted in limited efficacy in preventing the clinical and neuropathological abnormalities of the *Ndufs4*$^{-/-}$ mice (Di Meo et al., 2017). Self-complementary AAV vectors are modified AAVs that bypass the required second-strand synthesis to achieve transcription of the transgene allowing a superior and accelerated transduction in vitro and in vivo (Wang et al., 2003). For these reasons, we used a self-complementary AAV9 (scAAV9) vector to ubiquitously deliver the human NDUFS4 gene product, a protein highly similar to the murine ortholog, in *Ndufs4*$^{-/-}$ mice.

In this chapter I will describe the therapeutic outcomes following either a single intravascular (i.v.) injection or a double i.v. and intracerebroventricular (i.c.v.) injection of scAAV9-h*NDUFS4* in newborn *Ndufs4*$^{-/-}$ mice.

3.2. Evaluation of the therapeutic outcomes of gene rescue in *Ndufs4*$^{-/-}$ mice using a single i.v. injection of scAAV9-h*NDUFS4*

To investigate the therapeutic outcomes of AAV-mediated gene therapy in the brain, the human wild-type *NDUFS4* cDNA (h*NDUFS4*) was cloned into a scAAV viral vector under the control of the strong, general CMV early enhancer/chicken β-actin (CAG) promoter. This construct was then used to produce viral particles with the AAV9 capsid generating the final scAAV9-h*NDUFS4*.

A single dose of scAAV9-h*NDUFS4* was injected into the temporal vein in 4 *Ndufs4*$^{-/-}$ pups at postnatal day 1 (P1) with 10^{11} viral genomes (vg). This dosage was chosen since a previous attempt on 2 P1 *Ndufs4*$^{-/-}$ pups i.v. treated with $3.5X10^{10}$ virions was ineffective to significantly increase the rotarod performance (WT=257±9 s, n=7; *Ndufs4*$^{-/-}$=131±18 s, n=7; AAV-treated *Ndufs4*$^{-/-}$=97±12 s, n=2) and prolong the median lifespan of the treated animals compared to the untreated littermates (52 versus 45 days, long rank test; p n.s.) (Figure 3.2).

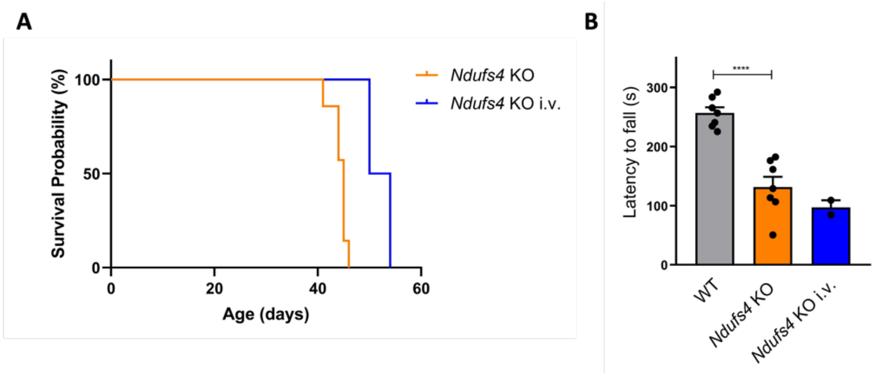

Figure 3.2. Clinical characterization of 10^{10} vg scAAV9-h*NDUFS4* i.v.-treated newborn mice. (A) Kaplan-Meier survival probability in *Ndufs4*$^{-/-}$ (orange; n=6), scAAV9^{NDUFS4} i.v.-treated *Ndufs4*$^{-/-}$ (blue; n=2). (B) Rotarod analysis in WT (grey; n=7), *Ndufs4*$^{-/-}$ (orange; n=7), scAAV9-h*NDUFS4* i.v.-treated *Ndufs4*$^{-/-}$ (blue; n=2). Error bars represent SEM. The asterisks represent the significance levels calculated by unpaired, Student's two-tailed t-test: *$p<0.05$, **$p<0.01$ and ***$p<0.001$.

3.2.1. Clinical characterization

The i.v. treatment with 10^{11} scAAV9 viral units prevented the coat loss and significantly prolonged the median lifespan of *Ndufs4*$^{-/-}$ mice (n=6) compared to the untreated littermates (n=7) (94 versus 45 days, long rank test; p=0.001). This is displayed in the Kaplan-Meier graph of Figure 3.3A. Nevertheless, all the treated animals, which seemed healthy for most of their lives and maintained a weight gain similar to the untreated animals (Figure 3.3B), exhibited a sudden decline in their final days. This decline was marked by the onset of ataxic gait, followed by locomotor freezing and food avoidance, leading to a loss of more than 15% of body weight – the threshold for humane euthanization under our ethical license.

Between the ages of 5 and 7 weeks, Ndufs4$^{-/-}$ mice undergo rapid degeneration and display a range of neurological symptoms, including a notable loss of motor skills. The impact of the scAAV9-hNDUFS4 treatment on their motor coordination was assessed using a standard accelerating rotarod test. At 40 days, untreated animals showed a significantly impaired motor performance, confirming degenerated motor skills (WT=238±16 s, n=8; Ndufs4$^{-/-}$=152±13 s, n=6; **p<0.01). Notably, the motor coordination of the AAV-treated Ndufs4$^{-/-}$ animals was comparable to the WT littermates (277±5 s, n=6; p=n.s.). However, there was a moderate reduction in the motor performance at 50 days (WT=261±11 s, n=8; i.v.-treated *Ndufs4*$^{-/-}$=233±15 s, n=6; p=n.s.), with a significant decline observed by 70 days of age (WT=260±10 s, n=8; i.v.-treated *Ndufs4*$^{-/-}$=145±14, s n=6; ****p<0.001) (Figure 3.3C). The only one untreated *Ndufs4*$^{-/-}$ individual living up to 50 days could barely stay on the rotating bar.

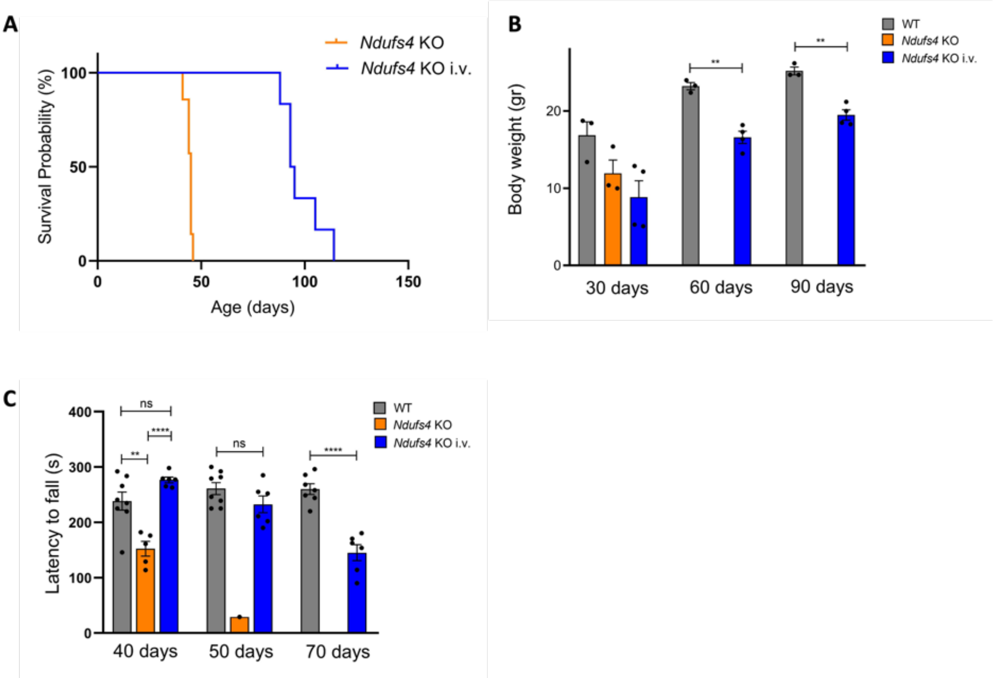

Figure 3.3. Clinical characterization of scAAV9-h*NDUFS4* i.v.-treated newborn mice. (A) Kaplan-Meier survival probability in *Ndufs4*$^{-/-}$ (orange; n=6), scAAV9 i.v.-treated *Ndufs4*$^{-/-}$ (blue; n=6). Significance was calculated with a long rank test (median life span 45 for *Ndufs4*$^{-/-}$ *vs.* 94 days for scAAV9 i.v.-treated *Ndufs4*$^{-/-}$; p<0.001). (B) Variation in body weights over time in WT (grey; n=6), *Ndufs4*$^{-/-}$ (orange; n=6), scAAV9-h*NDUFS4* i.v.-treated *Ndufs4*$^{-/-}$ (blue; n=6). Error bars represent mean±SEM. (C) Rotarod performance in WT (grey; n=8), *Ndufs4*$^{-/-}$ (orange; n=6), scAAV9-h*NDUFS4* i.v.-treated *Ndufs4*$^{-/-}$ (blue; n=6) mice. At 70 days no *Ndufs4*$^{-/-}$ mice were alive. Error bars represent mean±SEM. *p<0.05, **p<0.01, ***p<0.001 and ****p<0.0001 calculated by unpaired, Student's two-tailed t-test.

3.2.2. Molecular characterization

Given that the *Ndufs4*$^{-/-}$ mice symptoms are attributed mainly to brain anomalies (Quintana et al., 2010), I evaluated if *NDUFS4* expression was restored in the brain. In addition, I extended some analyses to other tissues relevant for mitochondrial disease, including heart and skeletal muscle.

First, I analysed the biodistribution of the viral vector in different tissues of treated *Ndufs4*$^{-/-}$ mice by quantitative PCR (qPCR). Approximately 1-2 vg/nucleus were detected in brain and heart, and 3-4 vg/nucleus in skeletal muscle (Figure 3.4A). Notably, three WT animals injected with the same amount of virus did not show any toxicity for up to 6 months. I used an anti-hNDUFS4 antibody to evaluate protein expression in brain homogenates by Western-blot (WB) immune-visualization. The hNDUFS4 protein expressed in treated wild-type and knockout animals was clearly detectable in amounts comparable to the murine endogenous protein detected in control littermates (Figure 3.4B).

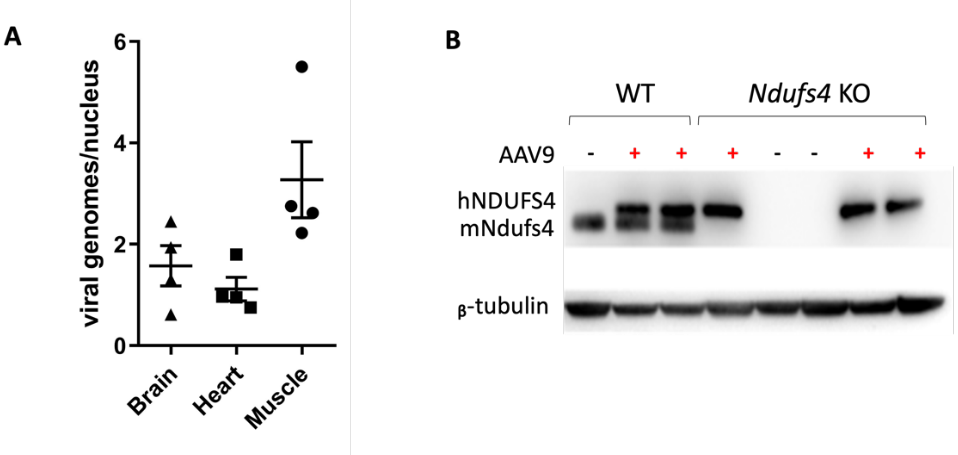

Figure 3.4. Molecular characterization of scAAV9-h*NDUFS4* i.v.-treated newborn mice. (A) Viral genome copies in tissues from AAV9-treated *Ndufs4*$^{-/-}$ mice (n=4). Error bars indicate the mean±SEM. (B) Western blot analysis of brain homogenates. β-tubulin was used as protein-loading standard.

Interestingly, I observed a difference in the apparent molecular weight between the endogenous murine NDUFS4 and the transduced human NDUFS4 proteins, as previously reported (Papa et al., 2008, Di Meo et al., 2017). I then investigated in greater detail the distribution of the hNDUFS4 protein in the brain tissue. Immunohistochemistry using the same anti-NDUFS4 antibody showed immunoreactivity in various brain regions of treated animals and was comparable with that shown in corresponding brain areas of controls (Figure 3.5). Importantly, no anti-NDUFS4-positive staining was present in untreated *Ndufs4*$^{-/-}$ animals.

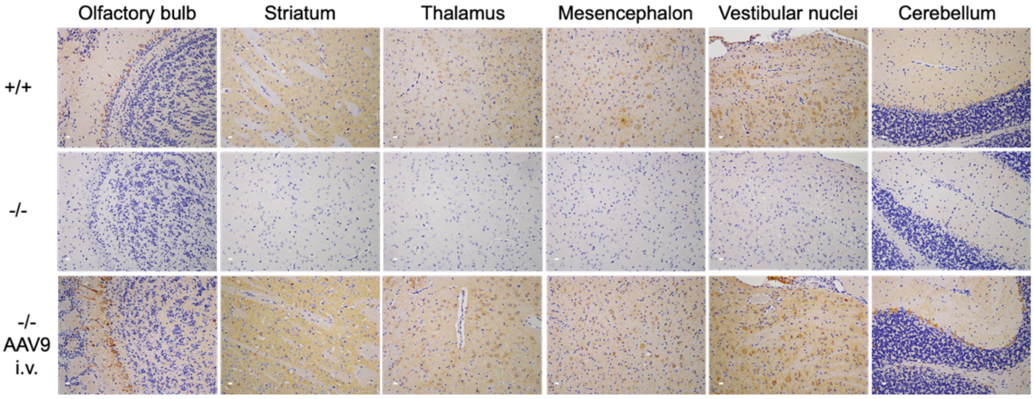

Figure 3.5. Restoration of NDUFS4 expression in the brain of a mouse injected with a single i.v. dose of scAAV9-h*NDUFS4*. Representative microscope images of the olfactory bulb, striatum, mesencephalon, vestibular nuclei and cerebellum stained using an anti-NDUFS4 antibody. Scale bars, 10 μm.

3.2.3. Biochemical characterization

The phenotype of *Ndufs4*$^{-/-}$ mice is attributed to a loss of NDUFS4 which leads to CI assembly defects (failure to assemble the N-module) and thereby a reduction of CI activity. I thus measured CI activity in brain homogenates of untreated and AAV-treated animals. As expected, rotenone-insensitive NADH (reduced nicotinamide dinucleotide)-CoQ (coenzyme Q) reductase activity was markedly decreased in *Ndufs4*$^{-/-}$ mice (30.0%±5.4% compared to WT, **p<0.01). In contrast, CI activity was 101.4%±12.9% of the WT in AAV-treated animals, demonstrating a biochemical rescue in these animals (Figure 3.6A). Furthermore, BNGE and in-gel activity on isolated brain mitochondria revealed that the activity associated with fully assembled CI was restored in scAAV9-h*NDUFS4*-treated *Ndufs4*$^{-/-}$ mice, while it was virtually absent in untreated animals (Figure 3.6B). Accordingly, western blot immunovisualization of the BNGE revealed robust recovery of fully assembled CI, although there was persistency of a well-known 830 kDa band (Figure 3.6C), which has previously been shown to correspond to the CI lacking the N module (Ogilvie et al., 2005). This band was the only CI-cross reacting material visualized in the lanes of untreated animals, which completely lack fully assembled CI.

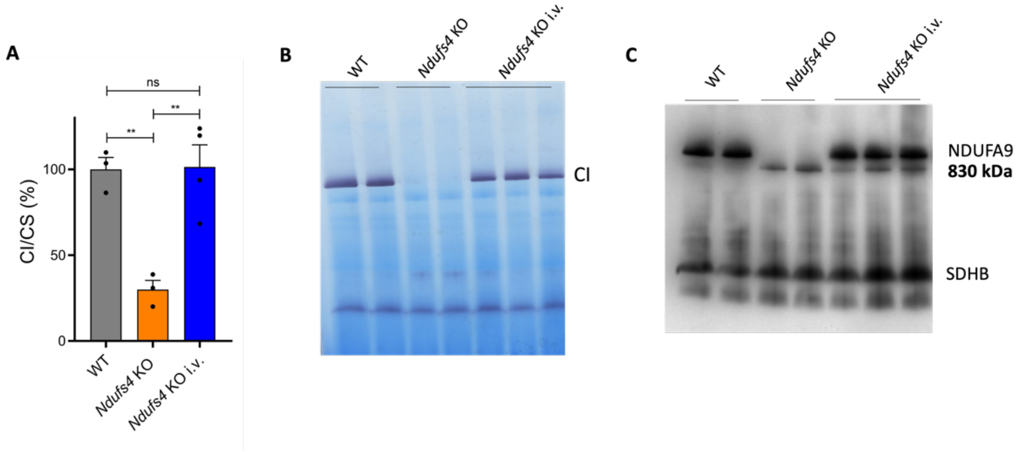

Figure 3.6. Biochemical characterization of scAAV9-h*NDUFS4* i.v.-treated newborn mice. (A) Spectrophotometric activity of complex I (CI) in brain homogenates from WT mice (grey; n=3), *Ndufs4*$^{-/-}$ (orange; n=3) and AAV-treated *Ndufs4*$^{-/-}$ mice (blue; n=4) expressed as a percentage of CI/citrate synthase (CS). Error bars represent SEM. The asterisks represent the significance levels calculated by unpaired, Student's two-tailed t-test: $*p<0.05$, $**p<0.01$ and $***p<0.001$. (B) In-gel activity for CI. Note the complete absence of the CI band in *Ndufs4*$^{-/-}$ samples. (C) Western blot analysis of first-dimension BNGE on brain mitochondria with antibody specific for CI (NDUFA9). Note that only the 830-kDa subassembly band is present in *Ndufs4*$^{-/-}$ samples, while both fully assembled, and subassembly bands are present after treatment with scAAV9-h*NDUFS4*. An antibody specific for complex II was used as loading control (SDHB).

3.2.4. Histological and immunohistochemical characterization

Next, I decided to evaluate whether scAAV9-h*NDUFS4* treatment could circumvent some of the histopathological features observed in *Ndufs4*$^{-/-}$ mice, such as gliosis, activation of microglia, and neuronal degeneration.

Neuropathological analysis of brain sections from the terminally-ill treated individuals revealed the presence of areas of neuronal loss, neurodegeneration, and spongiotic changes in the neuropilum (Figure 3.7 and Figure 3.8). To assess microgliosis, I performed an immunohistochemistry staining using an anti-CD68 antibody. Microgliosis refers to the activation and proliferation of microglia, which are the primary innate immune cells in the central nervous system (CNS) (Kettenmann et al., 2011, Eggen et al., 2013, Butvsky and Weiner, 2018). Microglia play a crucial role in maintaining the homeostasis of the CNS and are involved in immune surveillance, phagocytosis, and the release of various signaling molecules. All pathological changes in the brain result in the activation of microglial cells. CD68 is a transmembrane glycoprotein primarily expressed on the surface of macrophages. When microglial cells are activated in response to a pathological change, they undergo morphological changes and upregulate cell surface markers, including CD68. In the scAAV9-h*NDUFS4* i.v.-treated *Ndufs4*$^{-/-}$ animals, I observed scattered dark brown CD68-positive activated microglial cells in some brain regions (Figure 3.7B and Figure 3.8B). The primary method for detection of perturbed astrocytes (astrogliosis) is through glial fibrillary acidic protein (GFAP) immunohistochemistry which reveals the cytoskeletal protein unique to astrocytes (Fix et al., 1996, O'Callaghan and Sriram, 2005). Under normal circumstances, the astrocytes perform a variety of functions, including contributing to the blood-brain barrier, movement of nutrients and waste within the brain, and glutamate transport (Morenberg, 2005). Under perturbation or damage, they respond with a change in state, as they are being called upon to perform additional tasks (Morenberg, 2005). These perturbed astrocytes are more intensively stained due to an increased expression of GFAP. Immunohistochemical staining using an anti-GFAP antibody revealed areas of moderated reactive astrogliosis in the brains of the scAAV9-h*NDUFS4* i.v.-treated *Ndufs4*$^{-/-}$ animals (Figure 3.7C and Figure 3.8C). Lastly, I assessed neurodegeneration with PathoGreen staining, an anionic green fluorescent dye functionally similar to Fluoro-Jade dyes. These dyes stain degenerating neurons and their processes after exposure to a variety of insults. The mechanism of neuronal staining by anionic fluorescent dyes has not been determined. It has been proposed that the negatively charged dyes bind to positively charged polyamines or other molecules specifically generated in dying neurons. A significant neurodegeneration was observed in the same areas that displayed activation of microglia and astrogliosis (Figure 3.7D and Figure 3.8D). The lesions observed in the AAV-treated *Ndufs4*$^{-/-}$ animals were actually more severe than those observed in the untreated animals. This may be due to the fact that the untreated animals had a significantly shorter lifespan and were not able to develop fully formed lesions. Instead, they became manifested in the treated animals that had a longer survival time. The most affected areas in the AAV-treated brains included the olfactory bulb, frontal cerebral cortex, striatum, thalamus, and hypothalamus.

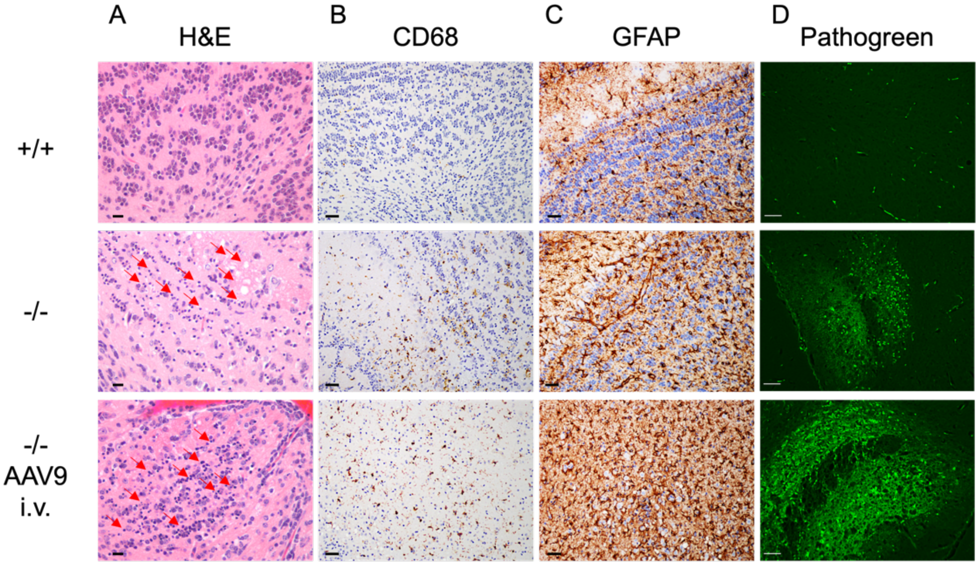

Figure 3.7. Profound alterations in the olfactory bulb from mice injected with a single dose of scAAV9-h*NDUFS4*. (A) H&E staining. Note the presence of degenerated neurons and spongiotic changes (red arrows) in the olfactory bulb of both untreated and treated *Ndufs4*$^{-/-}$ mice compared to the *Ndufs4*$^{+/+}$ animals. Scale bars, 10 μm. (B) Analysis of microgliosis by immunohistochemical staining with an anti-CD68 antibody reveals the presence of numerous dark brown activated microglial cells. Scale bars, 10 μm. (C) Analysis of astrogliosis using an antibody against the GFAP protein. Scale bars, 10 μm. (D) PathoGreen staining. Note the presence of many degenerated neurons in the olfactory bulb of the injected animals. Scale bars, 10 μm.

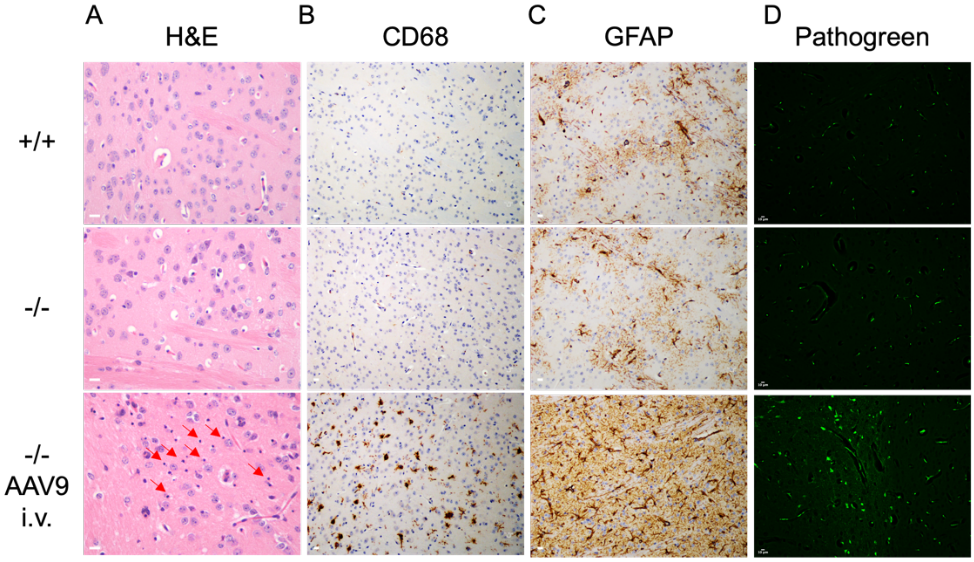

Figure 3.8. Morphological and immunohistochemical alterations in the striatum of a mouse injected with a single dose of scAAV9-h*NDUFS4*. (A) H&E staining showing the presence of degenerating neurons (red arrows) in the striatum from the mouse injected with a single dose of virus. Scale bars, 10 µm. (B) CD68 immunohistochemistry shows the presence of activated microglia (brown color). (C) Marked astrogliosis revealed by immunostaining with an antibody against GFAP. Scale bars, 10 µm. (D) PathoGreen staining showing the presence of a lot of degenerating neurons. Scale bars, 10 µm. Note that none of the stainings show the presence of pathological alterations in the striatum of the untreated animal.

3.3. Evaluation of the therapeutic outcomes of gene rescue in *Ndufs4*$^{-/-}$ mice using a double i.v. + intra-cerebral-ventricle (i.c.v.) injection of scAAV9-h*NDUFS4*

Although the results of the intravenous treatment were promising, the moderately survival rate of the animals was only moderately extended by three to four months compared to the untreated *Ndufs4*$^{-/-}$ littermates. The reasons behind the limited effects of the i.v. treatment are unclear, since I demonstrated that the recombinant protein was present in the brain, and a significant amount of assembled Complex I was detected, although there was also a quote of partially assembled Complex I that lacked the N module. However, the number of viral copies in the brain was relatively low (1-2 copies per cell on average). It is possible that the NDUFS4 protein, at the dosage of virus injection dosage, was unevenly distributed in the brain, as previously demonstrated by using a ssAAV9-*NDUFS4* vectors (Di Meo et al., 2017). This would explain the presence of patchy, severe lesions which were concentrated in specific areas of the brain in the euthanized i.v. treated animals such as the striatum (Figure 3.8). In an effort to overcome the marginal enhancement of the clinical outcome observed in our *Ndufs4*$^{-/-}$ model, we sought to increase the brain targeting of the recombinant vector. This was achieved by implementing a dual administration approach at P1. This protocol involved the i.v. injection of 10^{11} viral particles in the temporal vein, followed by the introduction of 10^{10} viral particles directly into the cerebral ventricle via intrathecal puncture.

3.3.1. Long-term survival and clinical outcome of the scAAV9-h*NDUFS4* i.v./i.c.v.-treated newborn mice

This treatment was performed in five *Ndufs4*$^{-/-}$ animals at P1. One animal died at 85 days of age with neurological symptoms and neuropathology similar to the single injected animals. The other four mice were sacrificed between 6 and 9 months of age, when they were all active and healthy, just to perform the molecular, biochemical, and morphological analysis. Weekly rotarod testing revealed considerable differences between individual mice. Importantly, one mouse could stand on the rotating bar for more than 200 s, while the other three mice managed times between 85 to 105 s (Figure 3.9A). Nevertheless, over time there was no evident decline in their performance, with each mouse maintaining consistent times across the tests. Consistently, there was not a marked difference in body weight between the four longer-living animals and their littermate controls (Figure 3.9B). However, the animal that received double injections and was euthanatized at 85 days consistently weighed less than its littermates, weighing 10 g at 80 days.

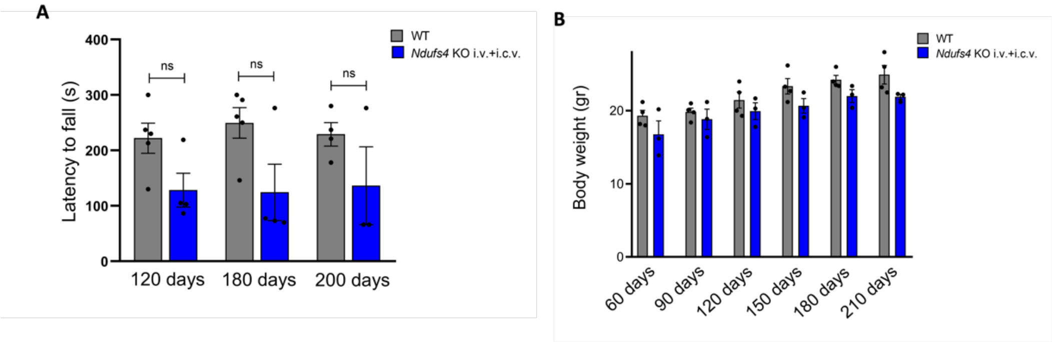

Figure 3.9. Clinical characterization of scAAV9-h*NDUFS4* i.v. + i.c.v.-treated newborn mice. (A) Rotarod analysis in WT (grey; n=5) and scAAV9-h*NDUFS4* i.v. + i.c.v.-treated *Ndufs4*$^{-/-}$ (blue; n=4) mice. Error bars represent SEM. (B) Variation of body weights over time in WT (grey; n=4), scAAV9-h*NDUFS4* i.v. + i.c.v.-treated *Ndufs4*$^{-/-}$ (blue; n=3) mice. Error bars represent SEM.

The Kaplan-Meier survival probability graph gave a long rank test of 0.001 in comparison to the survival probability of untreated littermates (Figure 3.10). This protocol ensured that the *Ndufs4*$^{-/-}$ mice remained healthy for longer periods than both their untreated naïve and i.v. treated animals. I euthanized the four double treated animals to analyze over time the biochemical, morphological and genetic features in comparison to controls.

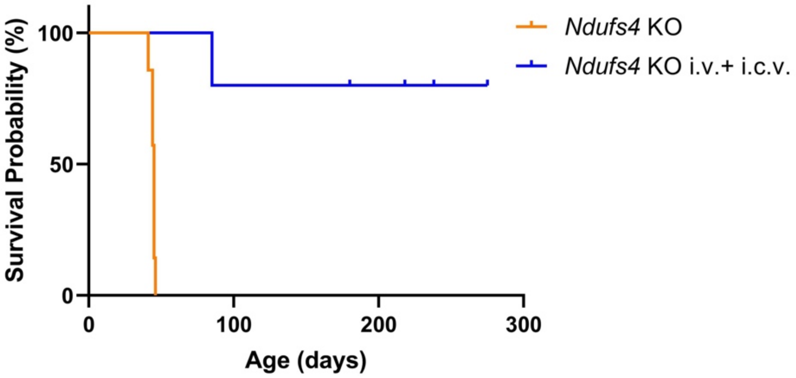

Figure 3.10. Lifespan of *Ndufs4*$^{-/-}$ mice upon scAAV9-h*NDUFS4* i.v. + i.c.v. treatment. Kaplan-Meier survival probability in *Ndufs4*$^{-/-}$ (orange; n=6), scAAV9-h*NDUFS4* i.v. + i.c.v.-treated *Ndufs4*$^{-/-}$ (blue; n=5). Significance was calculated with a long rank test (p=0.001). No WT mouse was loss during the period of evaluation.

3.3.2. Enhanced viral delivery and improved Complex I assembly in the brain of scAAV9-h*NDUFS4* i.v. + i.c.v.-treated *Ndufs4*$^{-/-}$ mice.

I analysed the biodistribution of the viral vector in different tissues of treated *Ndufs4*$^{-/-}$ mice. In the brain, specifically in the forebrain, the viral copy number was approximately 7 copies per cell, which was much higher compared to animals receiving only the i.v. treatment (Figure 3.11A). In skeletal muscle, the viral copy number was similar to that of the i.v. only treated mice, with approximately 3-4 copies per nucleus. Interestingly, the individual that became sick and died at 85 days also had 7 copies of viral vector per cell in the brain, suggesting that the viral copy number alone may not be the only determinant of the observed substantial prolongation of health and lifespan in the doubly treated animals. Other factors may also contribute to the overall therapeutic effect. Then, I measured CI activity in brain homogenates of untreated and AAV-treated mice. The rotenone-sensitive NADH-CoQ reductase activity was not significantly different from, and in fact, was comparable to that of age-matched control (84%±10% of the WT, p n.s.) (Figure 3.11B). Additionally, BNGE and in-gel activity on isolated mitochondria showed that the activity linked with fully assembled Complex I was restored in scAAV9-h*NDUFS4* i.v. + i.c.v.-treated *Ndufs4*$^{-/-}$ mice (Figure 3.11C). WB immunovisualization of the BNGE revealed robust recovery of fully assembled Complex I and the virtual absence of the 830 kDa band that was prominent in the naïve untreated animals in which assembled Complex I was undetectable (Figure 3.11D), as well as in i.v. treated animals. Altogether, these findings suggest that the double treatment approach led to increased viral payload and improved assembly of Complex I in the brain of treated mice, contributing to the observed extended lifespan and improved health outcomes.

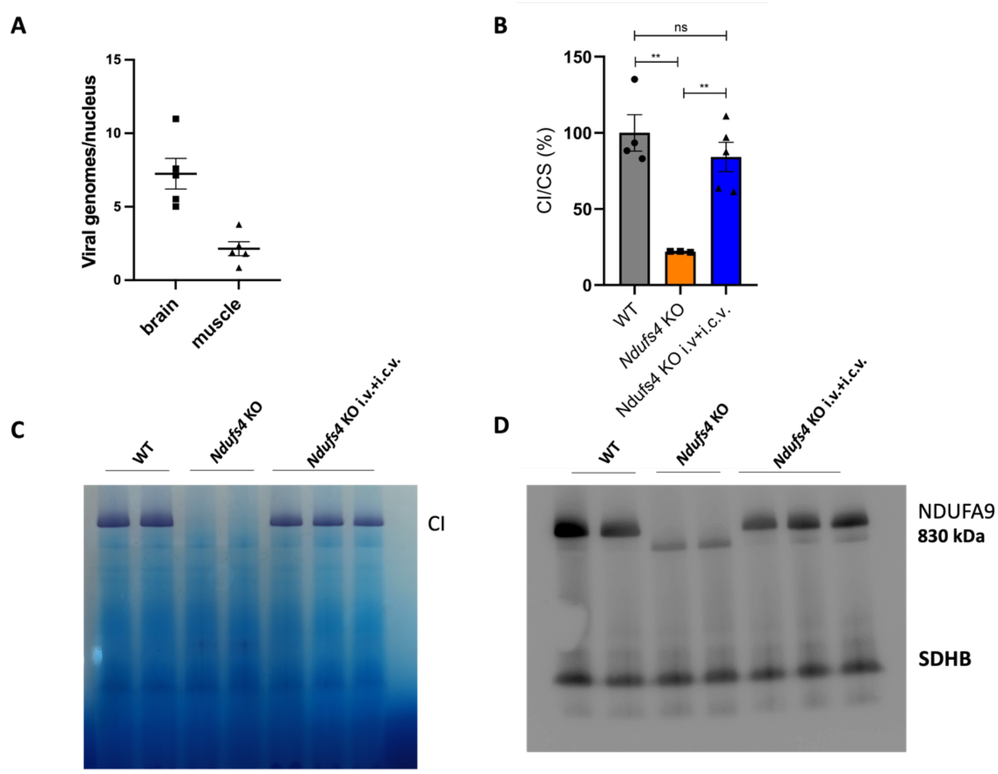

Figure 3.11. Molecular characterization of scAAV9-h*NDUFS4* i.v. + i.c.v.-treated newborn mice. (A) Viral genome copies content in brain from AAV-treated *Ndufs4*$^{-/-}$ mice (n=5). Error bars indicate SEM. (B) Spectrophotometric activity of Complex I (CI) in brain homogenates from *Ndufs4*$^{+/+}$ mice (grey; n=4), *Ndufs4*$^{-/-}$ (orange; n=3), AAV-treated *Ndufs4*$^{-/-}$ mice (blue; n=4) expressed as percentage of CI/citrate synthase (CS). Bars indicate SEM. *$p<0.05$, **$p<0.01$, ***$p<0.001$ calculated by unpaired, Student's two tailed t-test. (C) In-gel activity for CI. Note the complete absence of the CI band in *Ndufs4*$^{-/-}$ samples. (D) Western blot (WB) analysis of first-dimension blue-native gel electrophoresis on brain mitochondria with an antibody specific for CI (NDUFA9). Note that only the 830-kDa subassembly band is present in *Ndufs4*$^{-/-}$ samples, while both fully assembled and subassembly bands are present after treatment with scAAV9-h*NDUFS4*. An antibody specific for Complex II was used as control (succinate dehydrogenase B).

3.3.3. Histological analysis reveals a remarkable preservation of brain morphology in scAAV9-h*NDUFS4* i.v. + i.c.v.-treated newborn mice

The histological analysis of the brains from the four healthy animals that received the double treatment did not show any significant alterations. The brain sections exhibited a normal morphology, similar to that of age-matched control animals (Figure 3.12). Notably, there were no signs of spongiosis, activated microglia or reactive gliosis in the AAV-treated animals (Figure 3.12). Furthermore, Pathogreen staining revealed no evidence of degenerated neurons in several areas, including olfactory bulb and cerebellum (Figure 3.12 and 3.13). Examination of other organs, including the heart, liver, and kidney, revealed no evident abnormalities when stained with haematoxylin and eosin (Figure 3.14).

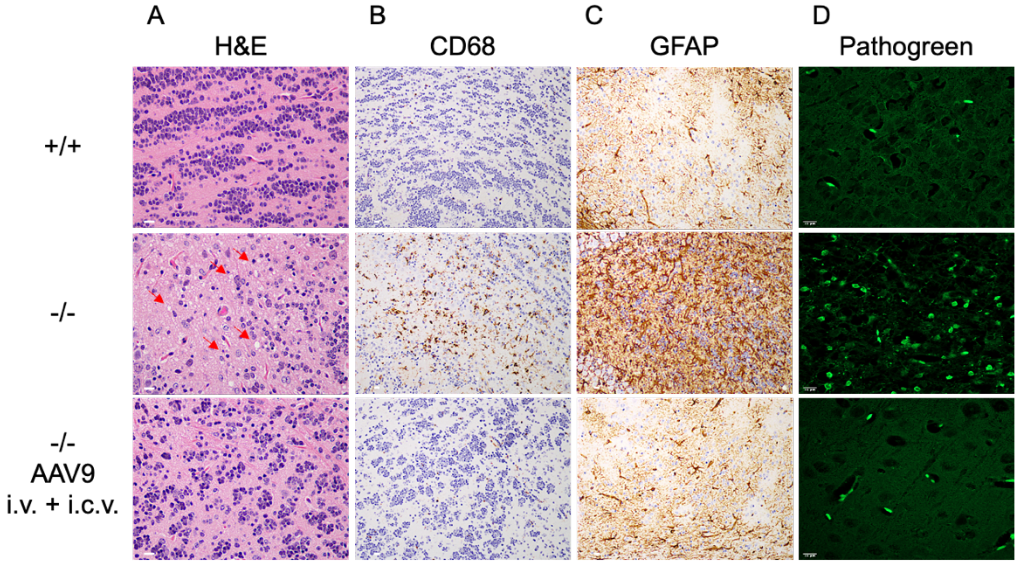

Figure 3.12. Preservation of brain morphology in scAAV9-h*NDUFS4* i.v. + i.c.v.-treated *Ndufs4*$^{-/-}$ mice. scAAV9-h*NDUFS4* prevented microgliosis, astrogliosis and neuronal degeneration in the olfactory bulb subjected to a double i.v. + i.c.v. administration of scAAV9-h*NDUFS4*. (A) Haematoxylin and eosin staining. Note the presence of spongiosis and degenerated neurons (red arrows) in the olfactory bulb of the untreated animal that are absent in scAAV9-h*NDUFS4*-treated animals. Scale bars, 10 μm. (B) Immunohistochemistry using an antibody against CD68 shows the presence of brown activated microglial cells in the olfactory bulb of the untreated animals that are absent in the treated animal. Scale bars, 10 μm. (C) Analysis of astrogliosis by immune decoration with an anti-GFAP antibody. Scale bars, 10 μm. (D) PathoGreen staining showing the absence of degenerated neurons in the scAAV9-h*NDUFS4*-treated animals. Scale bars, 10 μm.

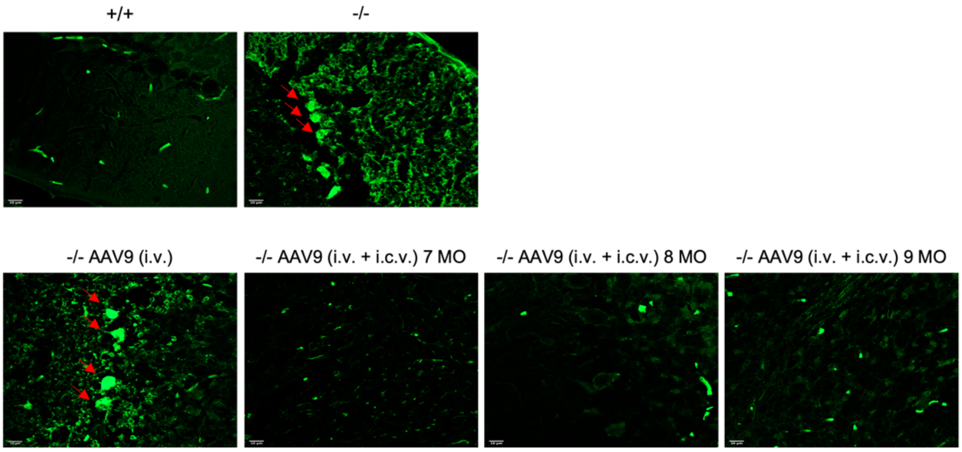

Figure 3.13. Neurodegeneration in cerebellum of *Ndufs4*$^{-/-}$ mice is reversed upon scAAV9-h*NDUFS4* treatment. Pathogreen staining specific to the degenerated neurons is positive in cerebellum (red arrows indicate Purkinje cells) of both untreated and scAAV9-h*NDUFS4* i.v.-injected *Ndufs4*$^{-/-}$ mice whereas it is negative in the scAAV9-h*NDUFS4* i.v. + i.c.v.-treated animals at 7, 8 and 9 months of age. Scale bars, 10 μm.

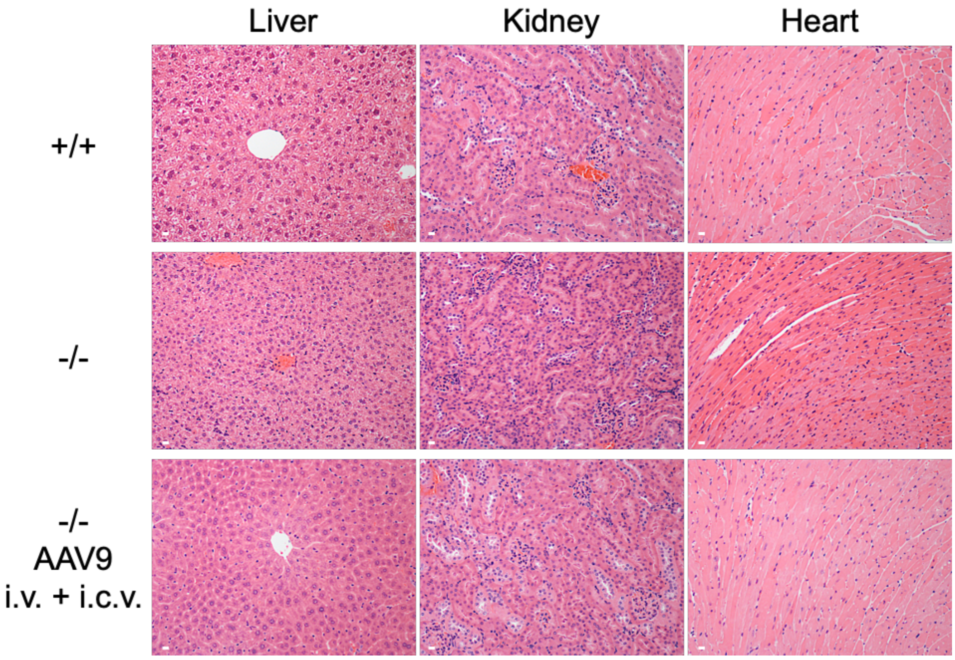

Figure 3.14. H&E staining does not show any morphological alterations in liver, kidney and heart from i.v. + i.c.v. treated animals. Scale bars, 10 μm.

In contrast, the animal sacrificed at 85 days showed neuropathological finding consistent with the previously treated animals that received only i.v. treatment (Figure 3.15). These findings included the presence of degenerated neurons, spongiotic changes, activation of the microglia and astrocytosis in in the same brain regions that were affected in the i.v. treated animals (e.g., olfactory bulb, thalamus, striatum, frontal cerebral cortex). Histological analysis of heart and kidney did not show any alteration, whereas the liver showed extensive apoptosis, which was further confirmed by immunohistochemistry with an anti-cleaved caspase 3 antibody (Figure 3.16).

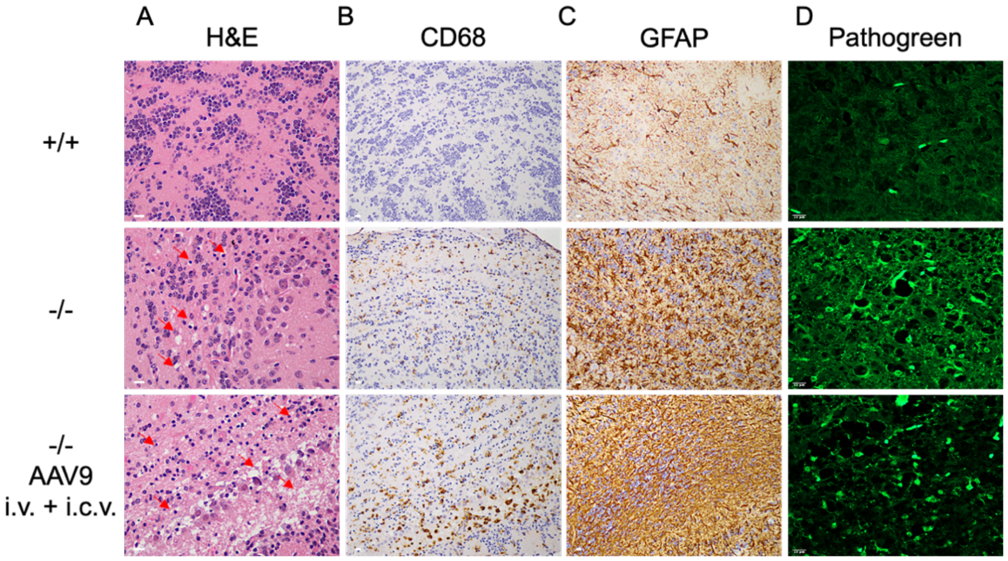

Figure 3.15. Neuropathological analysis of the olfactory bulb in the scAAV9-h*NDUFS4* i.v. + i.c.v.- treated mouse diseased at 85 days. Note the presence of spongiosis and degenerated neurons (H&E, red arrows) in the olfactory bulb of both untreated and AAV-treated mice. Immunohistochemistry for CD68 and GFAP reveals the presence of numerous dark brown activated microglial and astroglial cells in both the treated and untreated -/- mice. The Pathogreen staining, which is specific to neurodegenerated cells is robustly positive in both the treated and untreated -/- mice. Scale bars, 10 μm.

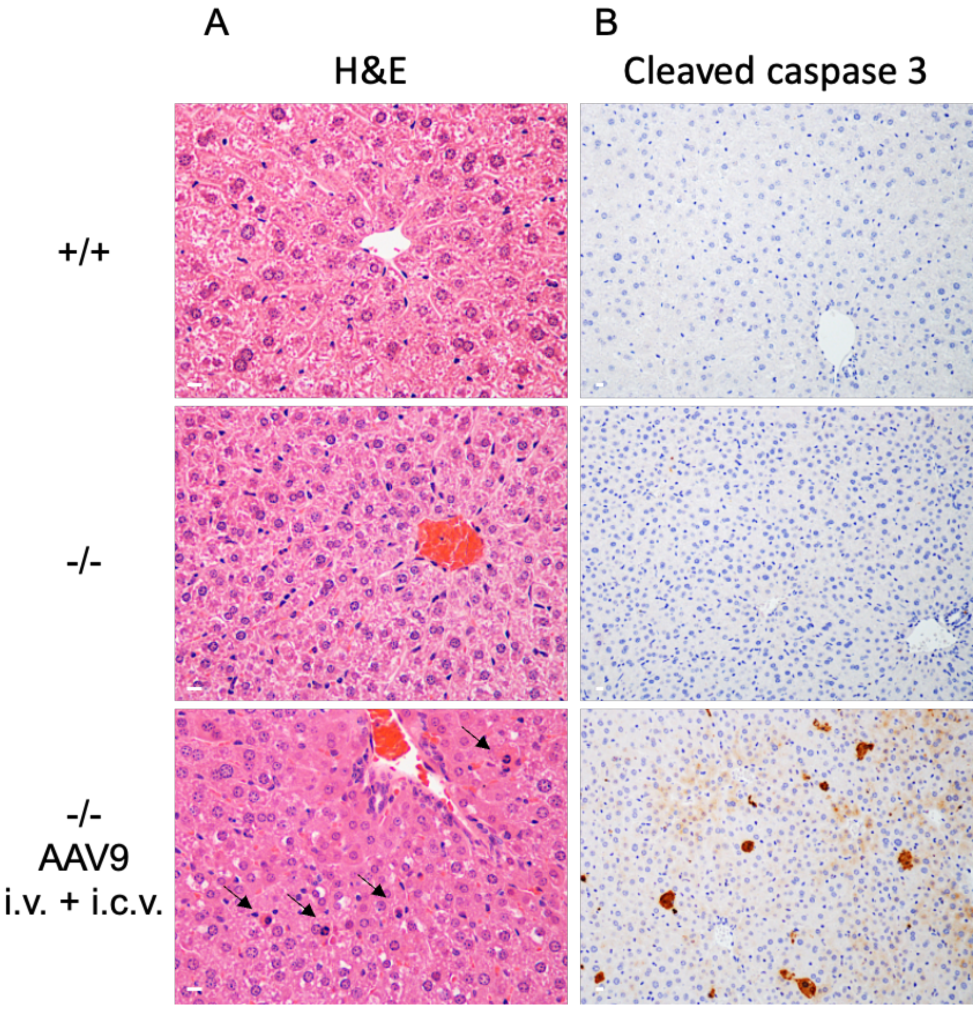

Figure 3.16. Presence of apoptotic hepatocytes in the liver of the scAAV9-h*NDUFS4* i.v. + i.c.v.-treated mouse diseased at 85 days. (A) H&E staining that shows the presence of apoptotic bodies (black arrows) in the liver of the i.v. + i.c.v. treated animal but not in the untreated one. Scale bars, 10 µm. (B) Immunohistochemistry using an antibody against the cleaved caspase 3 showing the presence of several apoptotic cells stained in brown. Scale bar, 10 µm.

Altogether, these findings indicate that the double i.v./i.c.v. treatment with the scAAV9-h*NDUFS4* vector effectively prevented the development of histological abnormalities in the brain tissues of the treated mice.

Chapter 4

Results

In vivo and *in vitro* characterization of the POLγA Y933C mutation

4. *In vivo* and *in vitro* characterization of the POLγA Y933C mutation

4.1. Introduction

Mutations in the *POLG* gene, which encodes the catalytic subunit of the mitochondrial DNA polymerase known as POLγA, are a major cause of human disease causing a spectrum of clinical manifestations characterized by either mtDNA multiple deletions or depletion of mtDNA copy number (Viscomi and Zeviani, 2017).

The range of syndromes related to *POLG* mutations varies widely in the clinical presentation. Interestingly, a single mutation can lead to different clinical manifestations, affecting various tissues and displaying a variable age of onset. Typically, an earlier age of onset correlates with more severe symptoms. However, the reasons for such complexity and tissue specificity are not fully understood.

Over 300 mutations in *POLG* have been identified. Among these, a substitution of Tyrosine with Cysteine at codon 955 (Y955C) is the most common autosomal dominant mutation found in patients and it causes autosomal dominant progressive external ophthalmoplegia (adPEO). This condition is associated with multiple deletions of the mtDNA (Van Goethem et al., 2001). AdPEO is clinically characterized by ophtalmoparesis, ptosis and myopathy. Different families have been described with variable additional symptoms, such as severe depression, peripheral neuropathy, hypoacusis, hypogonadism, ataxia, tremor, cataracts, and rhabdomyolysis. The disease onset typically ranges from 18 to 40 years of age.

Morphological analysis of patients' muscles reveals ragged red fibers and cytochrome c oxidase negative fibers. Electron microscopy of patients' muscles indicates abnormal mitochondria with distorted cristae and various inclusions. Biochemical analysis of the muscle respiratory chain activities often shows a mild deficiency of respiratory chain Complexes I, III and IV, which are the enzymes containing mtDNA-encoded components. However, sometimes, these levels can also fall within the normal range.

Before the start of my PhD, we generated a POLG knock-in mouse model harbouring the Y933C mutation, which corresponds to the human Y955C change. In this chapter, I describe:

1) the *in vivo* characterization of the mouse model harbouring the Y933C mutation at two different ages (5 and 24 months).

2) the *in vitro* characterization of the mouse Y933C and human Y955C mutations using purified recombinant protein versions of POLγA.

4.2. Phenotypic characterization of *Polg*^{Y933C} mice

4.2.1. Disrupted mendelian distribution of offspring observed in *Polg*^{Y933C} mice

Breeding of heterozygous *Polg*$^{+/Y933C}$ mice failed to produce homozygous *Polg*$^{Y933C/Y933C}$. From a total of 63 mice, I obtained 25 WT/WT and 38 *Polg*$^{+/Y933C}$ (Table 4.1), thus suggesting that Y933C is embryonic lethal with a complete penetrance when in homozygosity ($\chi^2 = 22.524$ with 2 df, ****p=0.0001). Such observation comes in line with the dominant behavior of *POLG* Y955C in human disease, and that only heterozygous patients have been reported so far. For this reason, this work restricted the analysis to *Polg*$^{+/Y933C}$.

Table 4.1 Distribution of *Polg*^{Y933C} genotypes from *Polg*$^{+/Y933C}$ X *Polg*$^{+/Y933C}$ interbreeding

Genotypes	Number expected [%]	Number observed [%]
Polg$^{+/+}$	15.75 [25 %]	25 [40 %]
Polg$^{+/Y933C}$	31,5 [50 %]	38 [60 %]
Polg$^{Y933C/Y933C}$	15,75 [25 %]	0 [0 %]

4.2.2. *Polg*$^{+/Y933C}$ mice did not display exercise intolerance and impaired motor coordination

Mutations in the human *POLG* gene, including Y955C, are associated with myopathy, often characterized by fatigue and exercise intolerance (Rahman and Copeland, 2019) in addition to a number of other symptoms. For this reason, I decided to evaluate whether the mutant mice presented compromised motor performance by running until exhaustion on a treadmill apparatus. Maximal exercise capability and endurance were evaluated by exhaustion trials, in which an automated treadmill and standardized program for increasing the belt speed by 0.24 m/min to a maximum speed of 75 m/min were used to run animals until they reached exhaustion, as defined in section 2.1.2.1. Five-month-old *Polg*$^{+/Y933C}$ mice did not display any significant difference compared to WT littermates (*Polg*$^{+/+}$=982±114 m, n=5; *Polg*$^{+/Y933C}$=971±84 m, n=5) (Figure 4.1A). As the Y955C mutation in patients causes a late-onset disease, we performed the treadmill test on 24-month-old animals, but no difference compared to the WT littermates was detected (*Polg*$^{+/+}$=687±58 m, n=3; *Polg*$^{+/Y933C}$=639±56 m, n=4) (Figure 4.1B). Due to the natural loss of exercise capability with aging, the distance reached at exhaustion by WT animals at 24 months of age was less than for the young age group.

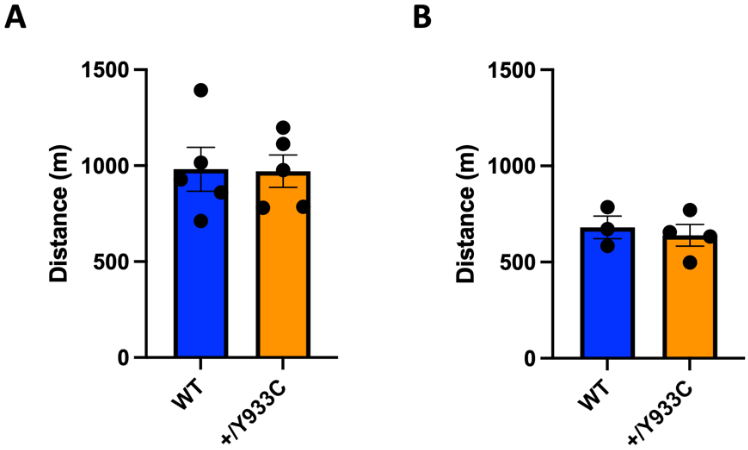

Figure 4.1. Evaluation of exercise endurance. (A) Distance run in meters by 5 month old WT (blue; n=5) and *Polg*$^{+/Y933C}$ (orange; n=5) animals on the treadmill. (B) Distance run in meters by 24-month-old WT (blue; n=3) and *Polg*$^{+/Y933C}$ (orange; n=5) animals on the treadmill. Data are presented as mean±SEM.

Motor performance and coordination were next assessed using a Rotarod apparatus. Mice were tasked with adapting to an increasing walking speed whilst maintain balance on a cylindrical rod for a duration of 5 mins. The latency to fall (s) was recorded manually per animal for three separate test trials, and these values were averaged per animal. Five-month-old and 24-month-old Polg$^{+/Y933C}$ heterozygous animals did not show any statistically significant difference in rotarod performance compared to the WT littermates (Figure 4.2).

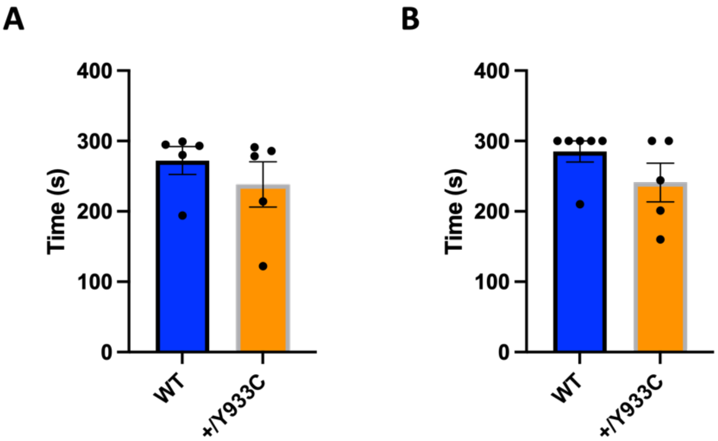

Figure 4.2. Evaluation of motor performance and coordination. (A) Time spent on the rotating rod by 5-month-old WT (blue; n=5) and *Polg*$^{+/Y933C}$ (orange; n=5) animals. (B) Time spent on the rotating rod by 24-month-old WT (blue; n=6) and *Polg*$^{+/Y933C}$ (orange; n=5) animals. Data are presented as mean±SEM.

4.3. Histological analyses of tissues from *Polg*$^{+/Y933C}$ mice

4.3.1. Histopathological alterations observed in brains of *Polg*$^{+/Y933C}$ mice

Murine tissues were subjected to histological examination to assess whether the *Polg* Y933C mutation affected the normal architecture of various high-energy tissue type and to determine if there were visible hallmarks of disease.

Brain sections stained with haematoxylin and eosin (H&E) did not reveal any obvious differences between WT and *Polg*$^{+/Y933C}$ at 5 months of age (Figure 4.3). However, at the age of 24 months, heterozygous mice exhibited a conspicuous vacuolation in the white matter of the cerebellum and the brainstem. This was either absent or much less abundant in WT littermate mice (Figure 4.4). The primary neurohistological indicators of perturbation in the brains, often associated with a diagnosis of inflammation, are activated microglia and astrocytosis. We analyzed these parameters by immunohistochemistry using suitable specific antibodies, as described in section 3.2.4.

IHC staining using anti-CD68 antibody revealed the presence of numerous activated microglial cells across the white matter of the cerebellum and the brainstem of the 24-month-old *Polg*$^{+/Y933C}$ mice (Figure 4.5), indicating an ongoing inflammatory process. Notably, some CD68 positive cells were also observed in the WT brains, likely as a consequence of aging. Moreover, the 24-month-old *Polg*$^{+/Y933C}$ showed a moderate increase in GFAP staining compared to the WT littermates in the brainstem (Figure 4.6). Altogether these data suggest that neurodegenerative processes are ongoing in the brain of the 24-month-old *Polg*$^{+/Y933C}$.

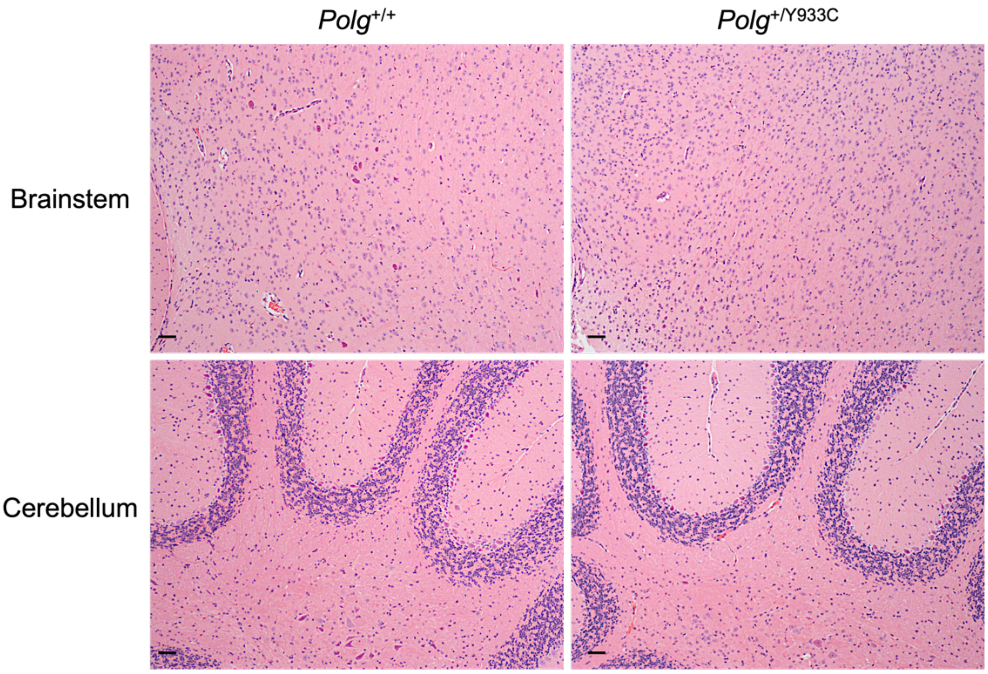

Figure 4.3. Histological analysis of brain of 5-month-old mice. Representative H&E staining of brain sections of 5-month-old *Polg*$^{+/Y933C}$ animals did not reveal any obvious morphological alterations. Scale bars, 50 μm.

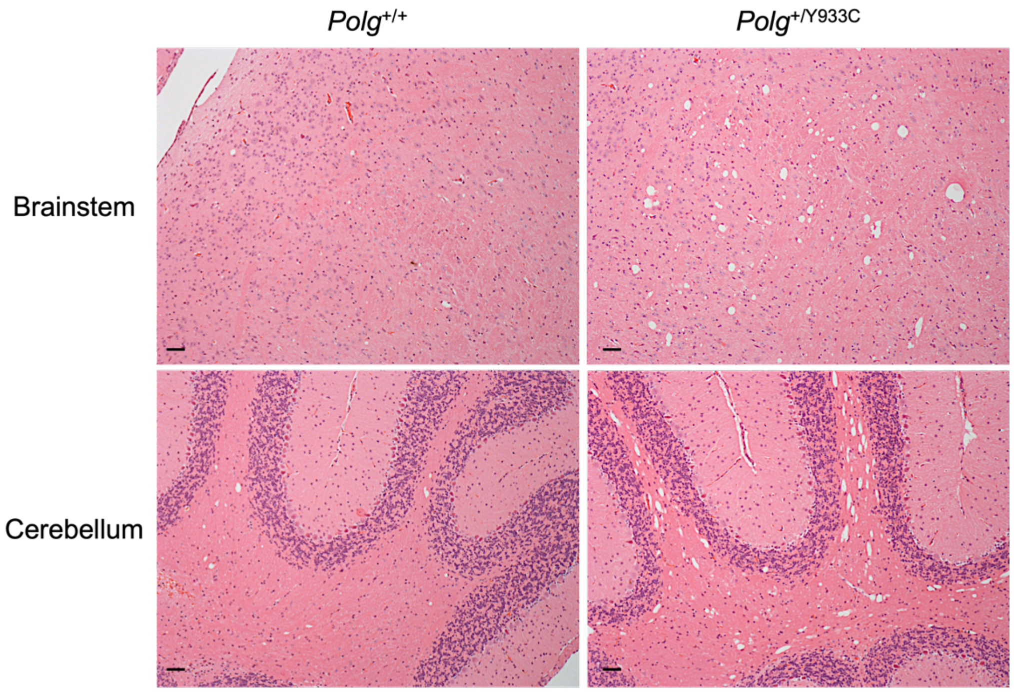

Figure 4.4. Histological analysis of brain of 24-month-old mice. Representative H&E staining of brain sections of 24-month-old *Polg*$^{+/Y933C}$ mice. Note the presence of extensive vacuolization in the brainstem and in the cerebellar white matter of the heterozygous mice which is hardly visible in the control littermates. Scale bars, 50 μm

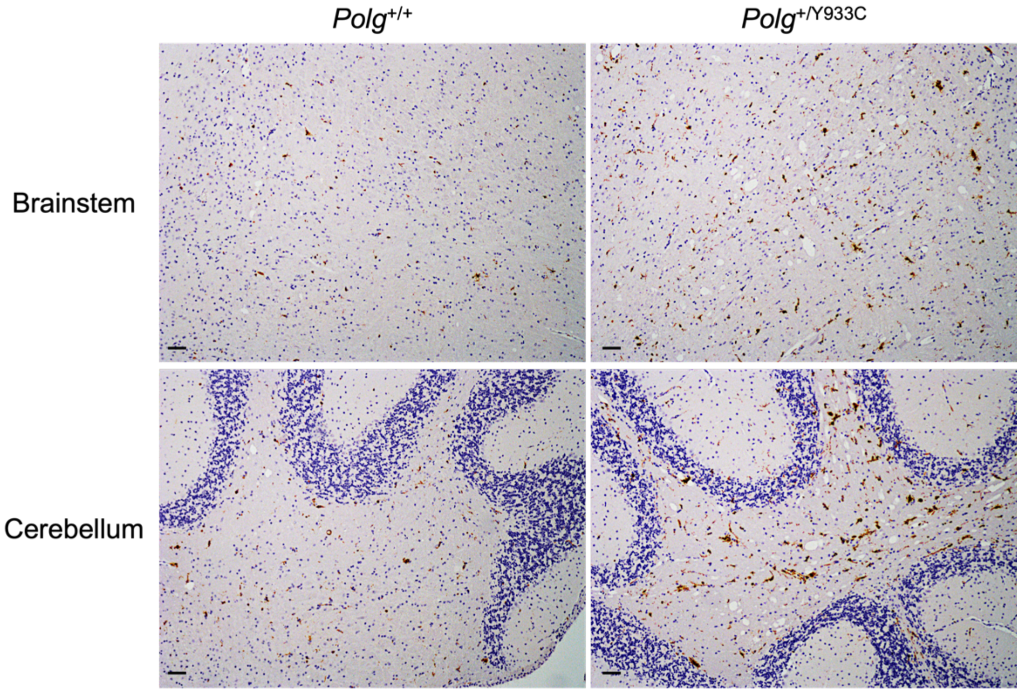

Figure 4.5. Immunohistochemical analysis of brain of 24-month-old mice. Representative CD68 immunohistochemistry of brain sections of 24-month-old *Polg*$^{+/Y933C}$ animals showing the presence of numerous brown activated microglial cells in the brainstem and the cerebellar white matter of *Polg*$^{+/Y933C}$ mice. Note that some positive cells are also present in the corresponding brain regions of WT littermates. Scale bars, 50 μm.

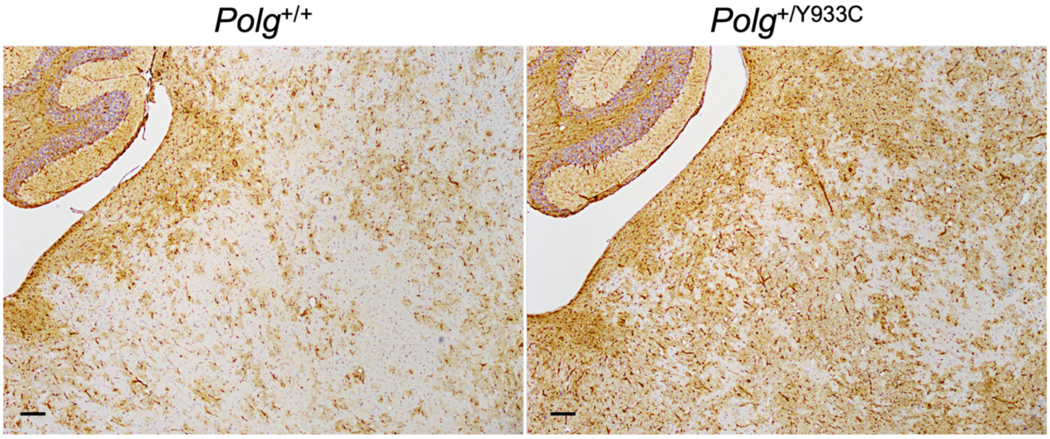

Figure 4.6. Immunohistochemical analysis of brain of 24-month-old animals. Representative GFAP immunohistochemistry of brain sections of 24-month-old *Polg*$^{+/Y933C}$ mice. Note the increased staining for GFAP in the brainstem of the heterozygous mouse. Scale bars, 100 μm.

4.3.2. Histological analysis of the skeletal muscle from *Polg*$^{+/Y933C}$

I next analyzed the skeletal muscle. H&E staining of gastrocnemius from 5-month-old *Polg*$^{+/Y933C}$ mice revealed small areas characterized by increased content of connective tissue, variation in fiber size, and the presence of centralized nuclei (Figure 4.7).

Muscle biopsies from *POLG* patients frequently exhibit cytochrome c oxidase (COX) negative fibers. Therefore, muscle samples from our mice were subjected to COX and SDH staining. However, I did not observe COX negative/SDH positive fibers. Nevertheless, we detected few fibers with central areas devoid of mitochondria that were negative for both COX and SDH stainings (Figure 4.8).

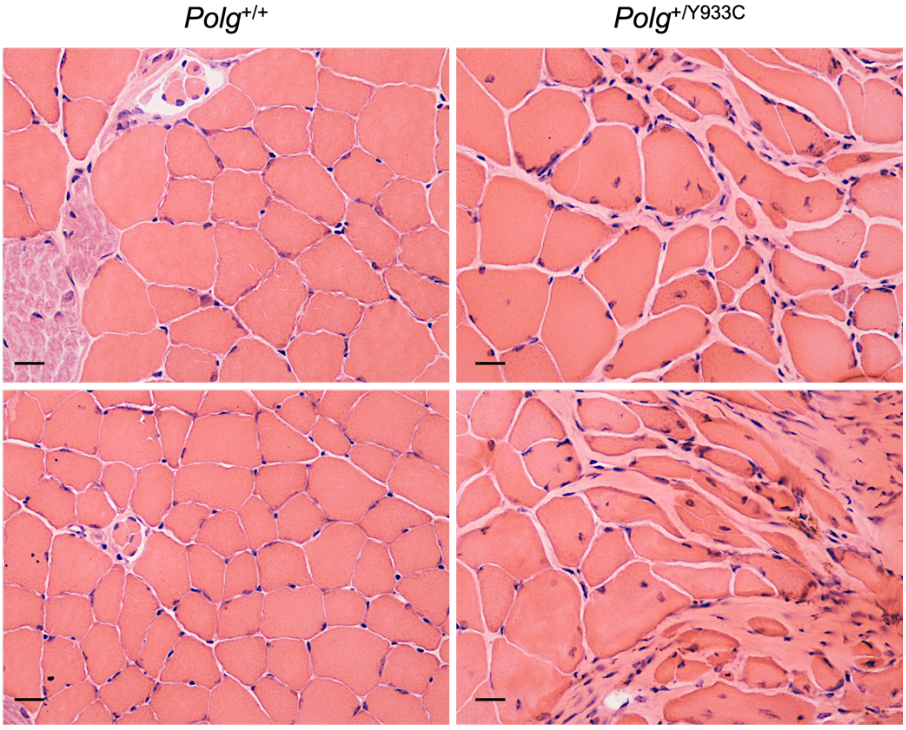

Figure 4.7. Histological analysis of the skeletal muscle. Representative H&E staining of skeletal muscle samples from 5-month-old *Polg*$^{+/Y933C}$ and WT animals. Note the presence of increased connective tissue and the variation in fibers size in the mutated samples. Scale bars, 20 μm.

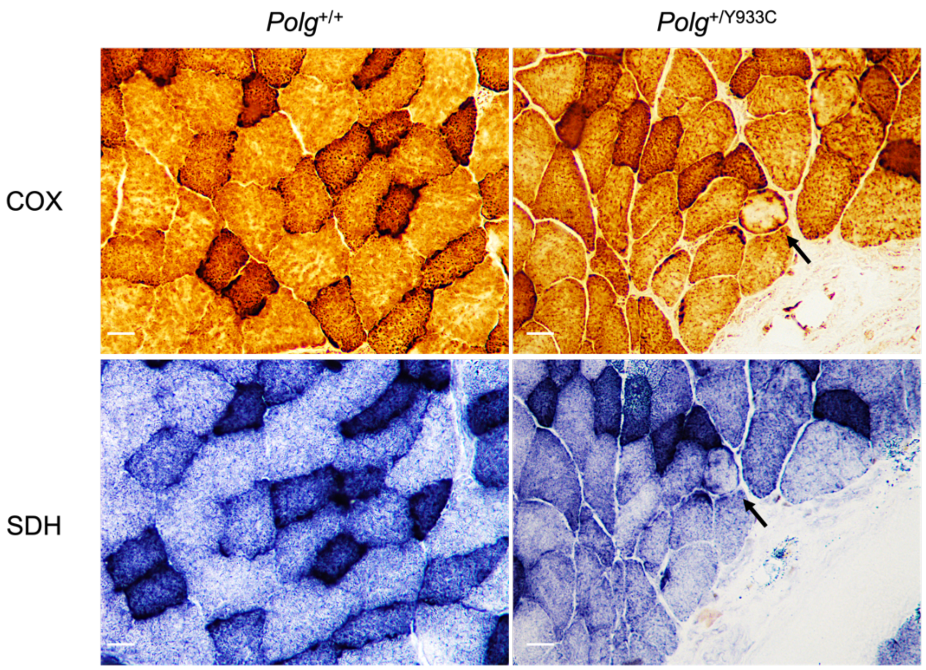

Figure 4.8. Histochemical analysis of the skeletal muscle. Staining for COX (top) and SDH (bottom) in skeletal muscle samples of 5-month-old WT and *Polg*$^{+/Y933C}$ animals. The black arrow pointed to a fiber with the central area devoid of mitochondria. Scale bars, 20 μm.

The H&E staining showed similar alterations in the skeletal muscle of both WT and *Polg*$^{+/Y933C}$ mice at 24 months of age, likely due to aging. However, double COX/SDH staining revealed the presence of several mitochondria-depleted fibers in the *Polg*$^{+/Y933C}$ mice (Figure 4.9). However, even at this age we were not able to detect the presence of COX negative fibers in the muscle from the heterozygous animals.

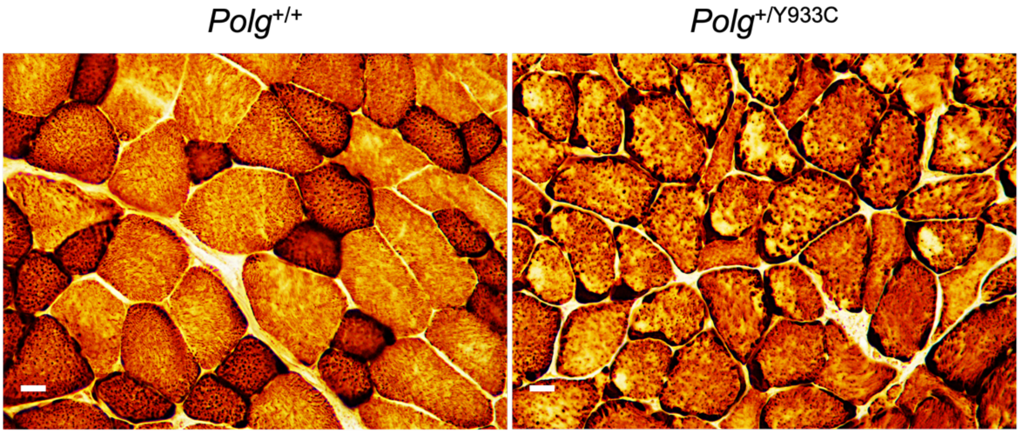

Figure 4.9. Double COX/SDH staining of skeletal muscle from 24-month-old animals. Representative picture showing the presence of mitochondria-depleted fibers in the *Polg*$^{+/Y933C}$ mouse. Scale bars, 20 μm.

4.3.3. Histological analysis of other tissues of *Polg*$^{+/Y933C}$ mice

I next analysed other high-energy tissue types from *Polg*$^{+/Y933C}$ mice and WT littermates.

No alterations were found in the kidneys of 5- and 24-month-old *Polg*$^{+/Y933C}$ compared to WT littermates (Figure 4.10).

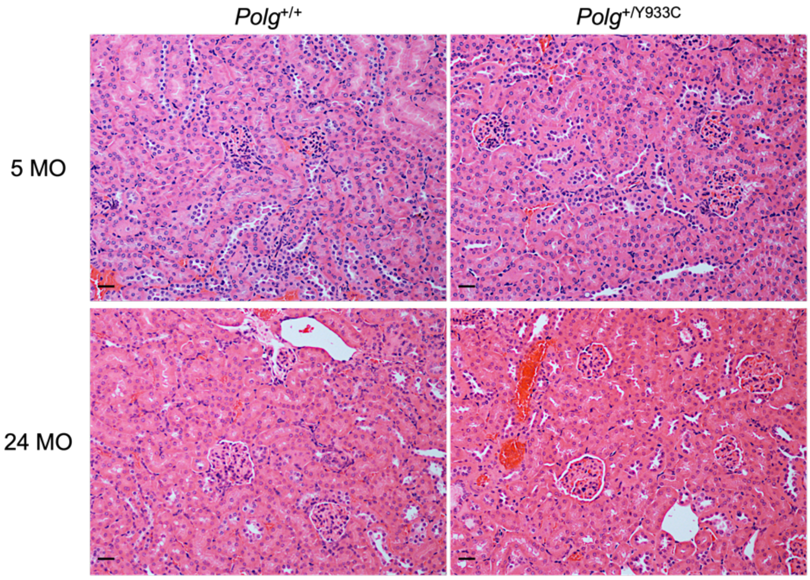

Figure 4.10. Histological analysis of kidney. Representative H&E staining of kidney sections of 5-month-old and 24-month-old WT and *Polg*$^{+/Y933C}$ animals. Scale bars, 40 μm.

Similarly, we did not observe any differences in heart sections from 5-month-old WT and *Polg*$^{+/Y933C}$ animals (Figure 4.11). At 24 months of age, both WT and heterozygous heart showed amyloidosis with no obvious difference between the two genotypes (Figure 4.11).

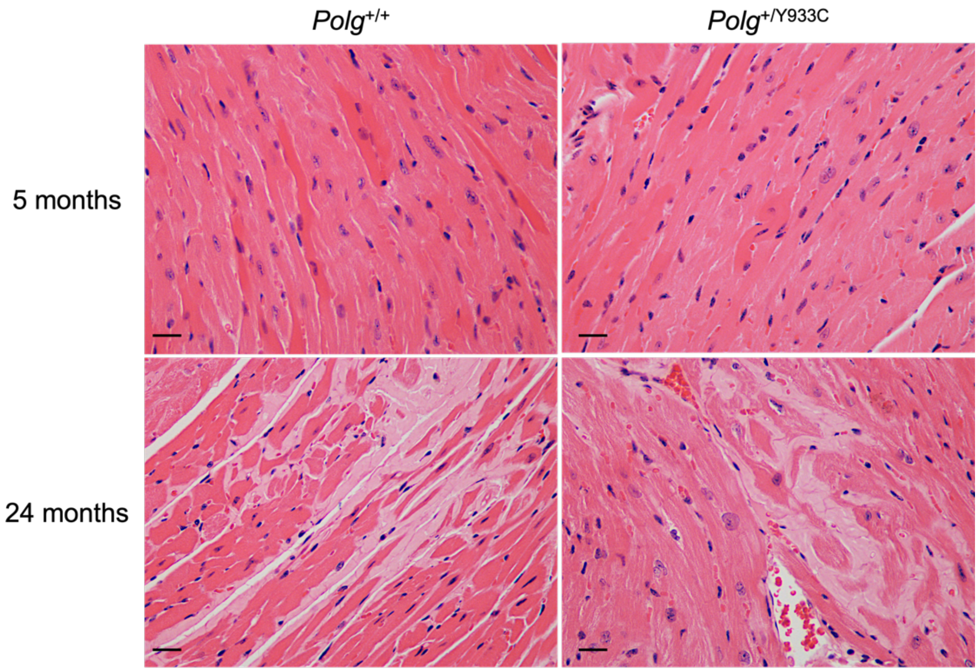

Figure 4.11. Histological analysis of heart. Representative H&E pictures of heart sections of 5-month-old and 24-month-old WT and *Polg*$^{+/Y933C}$ mice. Scale bars, 20 μm.

Finally, H&E staining of liver sections did not show any obvious differences between WT and *Polg*$^{+/Y933C}$ at 5 months of age (Figure 4.12). Instead, liver sections from older *Polg*$^{+/Y933C}$ mice showed increased steatosis and inflammatory cells around the vessels compared to the WT littermates (Figure 4.12).

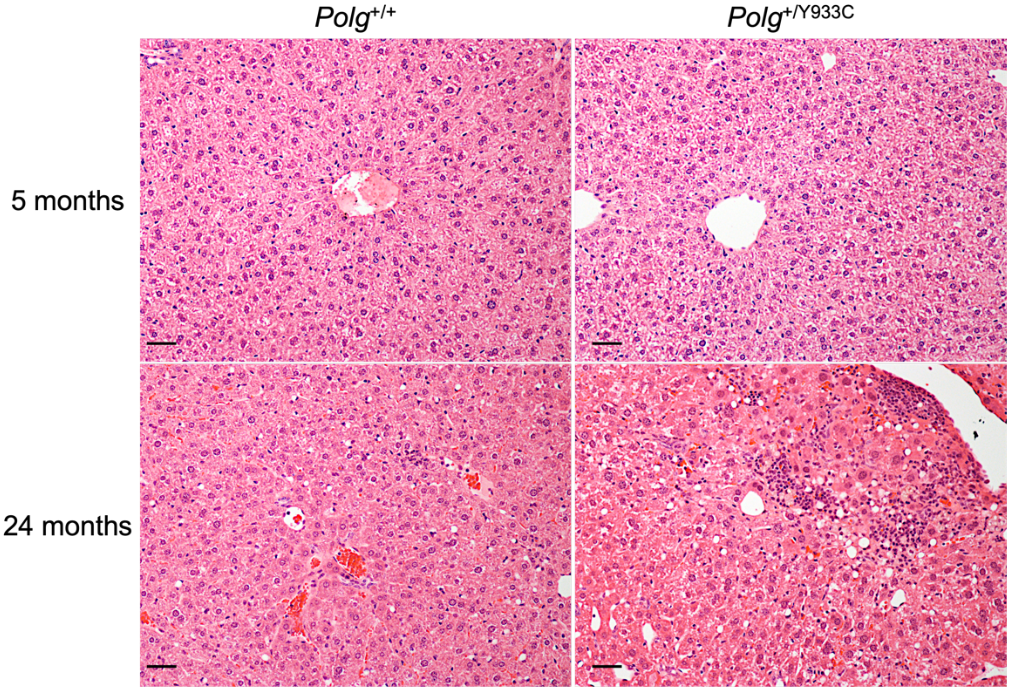

Figure 4.12 Histological analysis of liver. H&E pictures of liver sections of 5-month-old and 24-month-old WT and *Polg*$^{+/Y933C}$ mice. Note the increased steatosis and presence of inflammatory cells in the liver of 24-month-old mouse. Scale bars, 40 µm.

Altogether, these results indicate that the *Polg* Y933C mutation has little impact on the morphology of 5-month-old mouse tissues. However, several age-dependent alterations were detected at later stages, indicating a slowly progressive phenotype.

4.4. Molecular analyses of tissues from *Polg*$^{+/Y933C}$ mice.

4.4.1. *Polg*$^{+/Y933C}$ mice do not display mtDNA depletion

Since mutations in *POLG* are associated with a reduction of mtDNA copy number in human patients, I next investigated the mtDNA content in brain, skeletal muscle, and liver from both *Polg*$^{+/Y933C}$ versus WT littermates, at 5 and 24 months of age. mtDNA copy number was not significantly reduced in any of the tissues analyzed at any age (Figure 4.13).

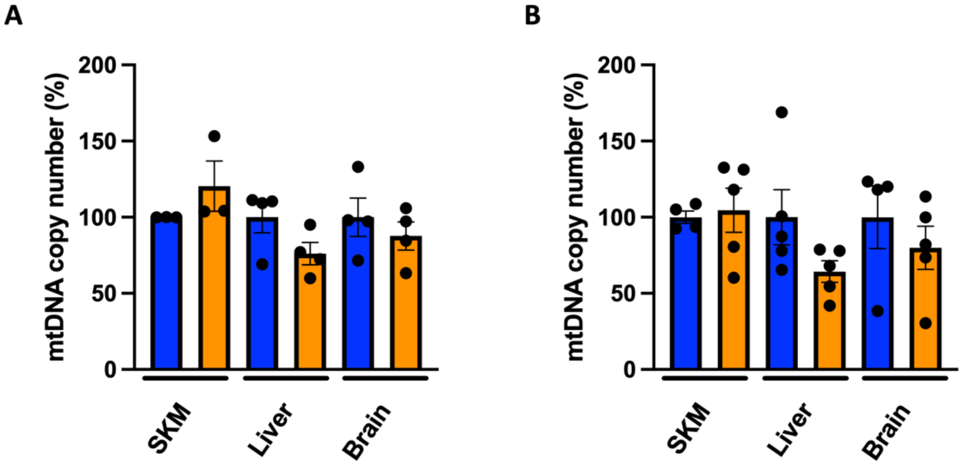

Figure 4.13. mtDNA levels in the different tissues of *Polg*$^{+/Y933C}$. Real-time qPCR quantification of mtDNA content in skeletal muscle (SKM), liver and brain of 5-month-old (A) and 24-month-old (B) WT and *Polg*$^{+/Y933C}$ animals. Data are presented as mean ±SEM. Each symbol represents a biological replicate.

4.4.2. Multiple mtDNA deletions are not detected in *Polg*$^{+/Y933C}$ mice

POLG mutations are also associated with multiple deletions of mtDNA in human patients. I thus examined the presence of such deletions in several tissues of *Polg*$^{+/Y933C}$ mice using long range PCR. Analysis of liver, skeletal muscle and brain revealed absence of mtDNA deletions in samples from 5-month-old *Polg*$^{+/Y933C}$ mice (Figure 4.14A). Although deletions of mtDNA were clearly detected in one sample, they were absent in the skeletal muscles of aged 24-month-old Polg$^{+/Y933C}$ mice (Figure 4.14B).

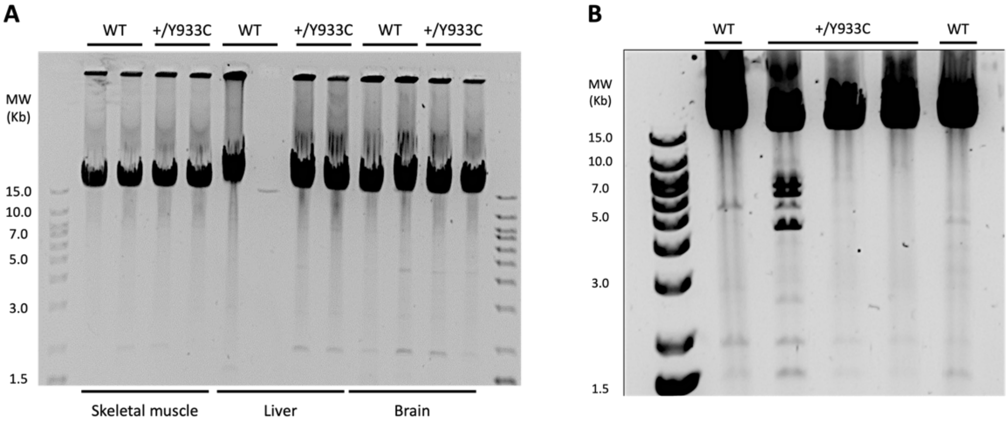

Figure 4.14. Investigation of mtDNA deletions in tissues of *Polg*$^{+/Y933C}$ mice. (A) Long-range PCR performed in DNA isolated from skeletal muscle, liver, and brain of 5-month-old WT and *Polg*$^{+/Y933C}$ animals. (B) Long-range PCR performed in DNA isolated from skeletal muscle of 24-month-old WT and *Polg*$^{+/Y933C}$ mice. Note the presence of multiple deletions in one *Polg*$^{+/Y933C}$ skeletal muscle sample. Primers amplifying a fragment of 15,781 bp of the mtDNA. Each lane represents a sample from an individual mouse. The bands were visualized by SYBR^{TM} safe staining.

4.5. *In vitro* characterization of mPOLγA mutant protein on mtDNA replication

To analyse the mechanistic consequences of the mutant POLγA Y933C on mtDNA replication and to compare it with the human counterpart, we expressed and purified both human (h) and mouse (m) WT (hPOLγA and mPOLγA) and mutant (hPOLγA^{Y955C} and mPOLγA^{Y933C}) as recombinant proteins. We then used such purified systems to study specific functions of POLγA, including DNA binding and polymerase activity.

4.5.1. Both mPOLγA^{Y933C} and hPOLγA^{Y955C} have similar affinities to DNA template

We used an Electrophoresis Mobility Shift Assay (EMSA) to measure the binding of either mPOLγA or hPOLγA to DNA in the presence of the accessory subunit POLγB (POLγA-B2). The binding of the holoenzyme complex POLγA-B2 to the DNA template causes a shift during electrophoresis, enabling the quantification of the portion of the holoenzyme that binds to the template. To fully shift the template, we found that 7.6 nM of either mPOLγA^{Y933C}-B2 or mPOLγA^{WT}-B2 was required (Figure 4.15A). Calculation of the dissociation constant for DNA binding, Kd(DNA), which measures the affinity of the protein to DNA, revealed no difference between the two holoenzymes. For mPOLγA^{WT}-B2, the Kd(DNA) was determined to be 1.3 nM ± 0.1, while for mPOLγA^{Y933C}-B2, the Kd(DNA) was 1.1 nM ± 0.1 (Figure 4.15B). Similarly, we observed no difference in the DNA binding affinity between hPOLγA^{Y955C}-B2 and hPOLγA^{WT}-B2. The kd(DNA) values were determined to be 1.0 nM ± 0.1 for hPOLγA^{WT}-B2 and 1.4 nM ± 0.1 for hPOLγA^{Y955C}-B2 (Figure 4.15A and 4.15B).

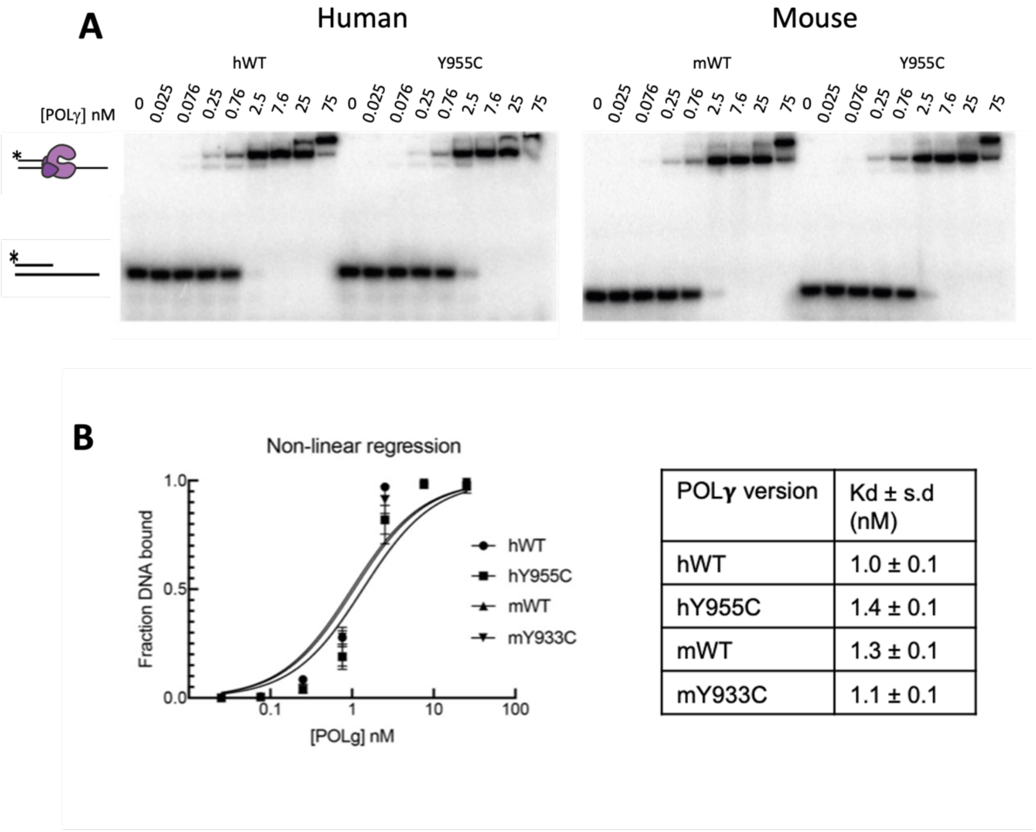

POLγ version	Kd ± s.d (nM)
hWT	1.0 ± 0.1
hY955C	1.4 ± 0.1
mWT	1.3 ± 0.1
mY933C	1.1 ± 0.1

Figure 4.15. *In vitro* characterization of hPOLγA^{Y955C} and mPOLγA^{Y933C}. (A) Electrophoretic mobility shift assay (EMSA) using WT and mutant POLγA with the addition of POLγB to estimate affinity to a DNA template. Each lane contains 10 fmol of DNA substrate and the indicated amount of POLγ holoenzyme (1 POLγA: 2 POLγB). The WT and mutant holoenzymes show similar DNA binding affinity. (B) Binding ratio of hPOLγA^{WT}, hPOLγA^{Y955C}, mPOLγA^{WT} and mPOLγA^{Y933C} with addition of POLγB, across increasing concentrations of POLγA-B2. Binding ratio was calculated as bound/(bound+unbound). Data are presented as mean ±SD. A nonlinear regression line was calculated for all the four holoenzymes.

4.5.2. mPOLγA^{Y933C} and hPOLγA^{Y955C} display impaired DNA synthesis in ssDNA templates

We performed a DNA synthesis assay using a long circular ssDNA template of 3,000 nucleotides annealed with a short 5' radiolabelled primer (Figure 4.16A) and evaluated polymerization of the second strand in presence of different amounts of dNTPs - 1, 10, 30 and 100 μM (Figure 4.16B). In this assay, when using either mPOLγA^{Y933C} or hPOLγA^{Y955C}, the synthesis of the second strand was impaired, even at high (100 μM) dNTP concentration. This concentration is significantly higher than the levels of dNTPs typically found in cells, which range from 1 to 10 μM in resting cells.

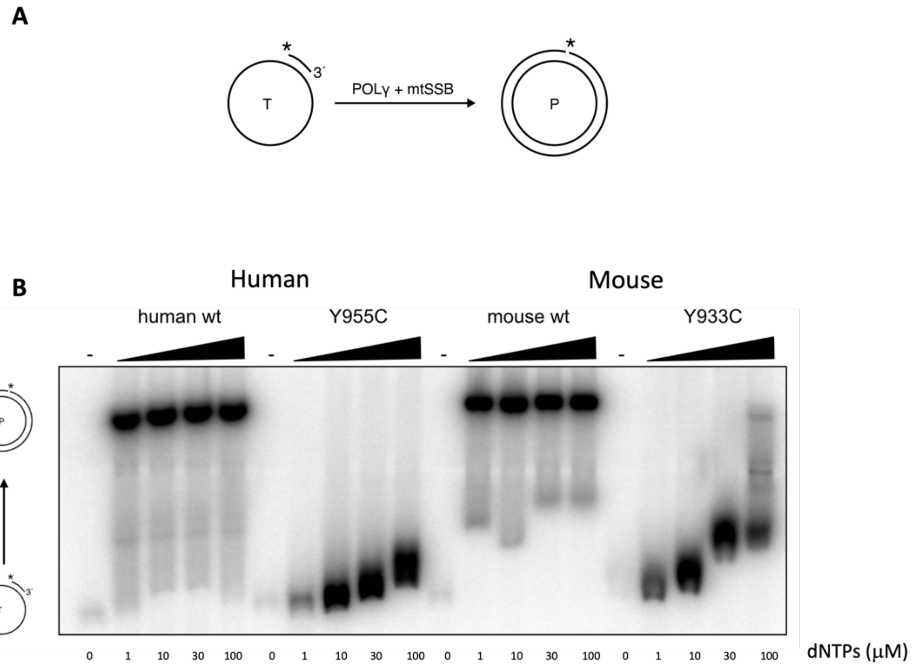

Figure 4.16. Analysis of hPOLγA^{Y955C} and mPOLγA^{Y933C} polymerase activity in long single-stranded templates. (A) Schematic representation of the second-strand synthesis. This assay evaluates the ability of the DNA polymerase to synthesize long stretches of DNA by synthesizing the second strand of a single-stranded template hybridized with a 5′ radiolabelled primer. POLγB and mtSSB are added to the reaction. (B) Second-strand synthesis assay using hPOLγA^{WT}, hPOLγA^{Y955C}, mPOLγA^{WT} and mPOLγA^{Y933C} to assess polymerase activity using long DNA templates. The reactions include POLγA-B2 and mtSSB and were incubated in the presence of different amounts of dNTPs, as indicated at the bottom of the blot. hPOLγA^{Y955C} and mPOLγA^{Y933C} clearly exhibit impaired DNA synthesis under increasing concentrations of dNTPs.

4.5.3. Both mPOLγA^{Y933C} and hPOLγA^{Y955C} have a dominant negative effect on the replisome and cannot support DNA synthesis on dsDNA templates.

Next, to monitor the effects of the Y933C mutation on replication of dsDNA, we used a template containing an about 4 kb long dsDNA region with a free 3′-end acting as a primer. This rolling circle replication assay is performed in the context of the minimal *in vitro* replisome, with addition of the TWINKLE DNA helicase, required to unwind the DNA, and mtSBB to stimulate the reaction. This reaction is also dependent on POLγB and once initiated, very long stretches of DNA can be formed (Figure 4.17A). In contrast to the WT polymerases, neither mPOLγA^{Y933C}

nor hPOLγA^{Y955C} could effectively support DNA synthesis on the dsDNA template in the presence of TWINKLE and mtSSB (Figure 4.17B; lanes 4-6 for hPOLγA^{Y955C}, lanes 22-24 for mPOLγA^{Y933C}).

The dominant effect of the Y933C mutation could be explained by competition with the WT POLγA for access to the primer template. We examined this hypothesis by gradually increasing the molar ratio of the mutant protein relative to the WT one. In a competitive situation, we would expect a decrease in DNA synthesis at higher concentration of the mutant protein relative to the WT one. Indeed, in the presence of higher mutant protein concentrations, we observed a strong reduction in DNA synthesis, supporting the idea of competition of the DNA template between the WT and the mutant proteins (Figure 4.17B; lanes 7-18 for hPOLγA^{Y955C}, lanes 25-36 for mPOLγA^{Y933C}).

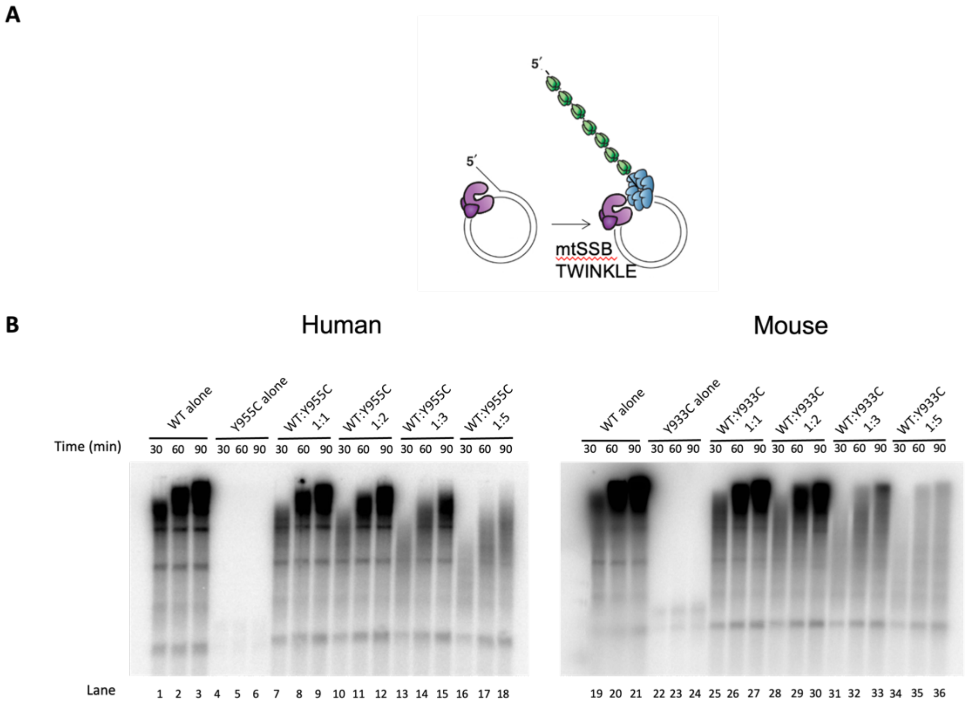

Figure 4.17. Effects of the Y955C and Y933C mutations in the context of the mitochondrial replisome. (A) Schematic representation of the rolling circle *in vitro* replication assay. The template consists of an incomplete double stranded DNA template with a mismatch on the 5′ of the incomplete strand. In the presence of TWINKLE and mtSSB, POLγA-B2 can polymerase long stretches of DNA using the 3′-end of the incomplete strand. (B) Rolling circle *in vitro* replication assay using hPOLγA^{WT} (lanes 1-3), hPOLγA^{Y955C} (lanes 4-6), mPOLγA^{WT} (lanes 19-21) or mPOLγA^{Y933C} (lanes 22-24) to assess polymerase activity in the context of the minimal mitochondrial replisome. The reactions were incubated at the indicated times (top).

A competition experiment was carried out to show the dominant negative effect of the Y955C mutation (lanes 7-18) and the Y933C mutation (lanes 25-36). In this experiment we used a constant amount of POLγA^{WT} but increasing amounts of the mutant version. The reactions were incubated at the indicated times (top).

Chapter 5

Discussion and future directions

5. Discussion and future directions

Mitochondrial disorders are devastating conditions, particularly in infants and children, for which no effective cure is currently available. Leigh disease, also known as subacute necrotizing encephalomyelopathy, is a neuropathological condition characterized by multiple symmetrical foci of incomplete necrotic lesions in various brain regions. Typically appearing in infancy or early childhood, Leigh disease manifests with psychomotor regression, swallowing difficulties, respiratory irregularities, ocular motor abnormalities, and more, often leading to death within two years from presentation. The disease common denominator is an impairment of cell bioenergetics, primarily linked to mitochondrial metabolism. In chapter three I investigated the therapeutic outcomes of gene therapy using a scAAV9-h*NDUFS4* viral vector in a mouse model of Leigh syndrome, the *Ndufs4*$^{-/-}$ mouse. This mouse model lacks NDUFS4, an essential subunit of Complex I, causing severely impaired activity and assembly in the knockout mouse tissues and in the patients.

A single intravenous (i.v.) injection of scAAV9-h*NDUFS4* in *Ndufs4*$^{-/-}$ mice at P1 showed that the viral particles cross the blood-brain barrier driving the expression of the recombinant protein in the brain and other organs. The expression of NDUFS4 significantly prolonged the lifespan of the *Ndufs4*$^{-/-}$ mice up to 100 days after birth, while the untread *Ndufs4*$^{-/-}$ littermates had a survival median of 45 days. However, the clinical conditions of these animals deteriorated rapidly, and I had to euthanize them when the loss of body weight exceeded 15%. The reasons for this worsening are unclear, as the recombinant protein was still detected in various brain regions. A possible explanation is that the viral copy number detected in the brains was still relatively low, (1-2 copies per cell), despite the high dosage of the treatment (10^{11} viral particle). This suggests that the distribution of the human NDUFS4 protein was still uneven, and failed to sufficiently rescue the high energy demands of critical brain areas. The interpretation is supported by the presence of a substantial amount of the 830-kDa subassembly band in BNGE in treated mice. Over time, the cells that do not express NDUFS4 can undergo neurodegeneration, which is indeed observed in post-mortem tissues from these animals.

I then adopted a protocol which includes the double administration of recombinant scAAV9-h*NDUFS4*, by both i.v. and i.c.v. injections at P1 (Di Meo et al., 2017). Four out of five doubly treated animals lived at least 6 months, gained weight similarly to the wild-type littermates, and their locomotor skills and coordination were relatively well preserved. The post-mortem analysis of their brains showed widespread expression of NDUFS4 in several cerebral areas, preservation of the morphology and normalization of Complex I activity and assembly. Importantly, the additional i.c.v. administration of scAAV9-h*NDUFS4* resulted in a much higher virion copy number per cell than the only i.v. injection (7 versus 1) warranting a more even distribution of the therapeutic gene and its long-standing expression. One mouse survived only 85 days after the double treatment. Neuropathological analysis revealed lesions similar to those observed in animals treated with the i.v. injection only. This outcome highlights the technical challenges of i.v. or i.c.v. administration of the vector, and the potential threat of some genetic variants that could interfere with the effective complementation of the therapy. Some animals may be resistant to the therapeutic effect of the gene therapy approach, resulting in outcomes that fall below the desired goal of a radical and long-standing cure *in vivo* for OXPHOS-related gene defects. Nevertheless, further investigations will be needed to fully prove the potential translatability of scAAV9-based therapy, for instance by deferring the treatment to the prodromal phase of the disease in mice, which is more reflective of the real situation in children with Leigh disease, as their diagnosis is rarely available at birth. Additional future experiments will investigate the applicability of scAAV9-based gene therapy to other nuclear-encoded genes known to be responsible of Leigh disease. Alternative strategies include the direct administration of *Ndufs4* RNA, given the important results obtained by an approach termed selective endogenous encapsidation for cellular delivery. This technique exploits the capacity of some retroviral-like proteins to secrete their own RNA, opening the possibility to exploit them to deliver functional mRNA cargos to mammalian cells (Segel et al., 2021).

The results presented in the first part of this thesis indicate that AAV-based gene therapy is highly effective in improving the clinical and biochemical phenotype of Ndufs4-/- mice. However, the translation of this approach to the clinics still faces several challenges. First, Leigh syndrome is genetically highly heterogeneous and can be caused by mutations in over 75 genes. In principle, according to the current regulations, each gene therapy product should be tested independently for efficacy, safety and biodistribution. Each of these steps is time-consuming, highly expensive, and basically unaffordable. The development of centralized platforms aimed at optimizing the manufacture and testing, and the possibility of considering each drug independent of the gene product carried by each vector (ie.: considering only the vector features, including serotype, promoter, polyA etc…) could be possible solutions.

A second problem is related to the necessity of reaching as many cells as possible for cell-autonomous diseases. Our data indicate that efficient rescue of Ndufs4$^{-/-}$ phenotype is obtained only if the defect is corrected in virtually all the cells. This is an extraordinary challenge especially in the brain.

Finally, several lines of evidence in the literature and the recent experience in clinical trials indicate that toxicity may be different between models and humans. For instance, liver and cardiotoxicity have been reported in trials on Duchenne muscle dystrophy and myotubular myopathy and not observed in the preclinical experiments (Ling et al., 2023). The doses currently used in trials are very high. This, besides being a challenge for manufacture, increases the possibility of side effects. The development of new, more effective serotypes and optimized expression cassettes will be essential to overcome these problems.

The development of more faithful animal models and improved design of preclinical trials are thus required to move to the trials in humans. Our attempts to generate a panel of knockin mouse models by CRISPR/Cas9 representing all the major mutations described in POLG patients is an example of this effort (see below). However, it should be mentioned that mouse models for mitochondrial diseases have several limitations, as they rarely reproduce the symptoms of the human syndrome, despite often reproducing the biochemical and molecular defects.

Overall, if these preclinical experiments on mice will be successful, the next step to follow would be the translation of these procedures to patients, which is our goal for the next few years.

Mutations in *POLG* are a common cause of a spectrum of mitochondrial diseases. The substantial lack of relevant *in vivo* models has hampered our understanding of the pathogenesis of *POLG*-related disorders. Before the start of my PhD, we generated a *POLG* knockin mouse model, corresponding to the human Y955C mutation, the most common dominant *POLG* mutation. The human POLγA Y955 is evolutionarily conserved from chimpanzee to fruit fly, including mice. The high evolutionary conservation among species further supports the importance of the residue Y955 in POLγA function and upholds the pathogenicity of mutations affecting it in human patients (Camps et al., 2007). In chapter 4, I described:

1) The *in vivo* characterization of the *Polg*$^{+/Y933C}$ mouse model.

2) The *in vitro* characterization of the mouse Y933C and the human Y955C mutations using purified recombinant protein version of POLγA.

The human *POLG* Y955C mutation was only found in heterozygous patients (Human DNA POLγA Mutation Database http://tools.niehs.nih.gov/polg/). Accordingly, crossing heterozygous *Polg*$^{+/Y933C}$ mutant mice revealed complete embryonic lethality of *Polg*$^{Y933C/Y933C}$ mutants. Thus, the mouse *Polg*^{Y933C} replicate the dominant inheritance pattern seen in humans.

Although the *Polg*$^{+/Y933C}$ mice did not show significant phenotypic alterations in terms of exercise intolerance and impaired motor coordination, histological analysis revealed some pathological changes in brain, liver, and skeletal muscle of aged mice. In brain, vacuolation was observed in the white matter of the cerebellum and brainstem of 24-month-old heterozygous mice, along with an increased number of activated microglial cells, suggesting an inflammatory process and ongoing neurodegeneration. Histological analysis of liver sections revealed increased steatosis and inflammatory cells around the vessels, indicating potential liver dysfunction. Double COX/SDH staining of skeletal muscle sections from *Polg*$^{+/Y933C}$ animals revealed the presence of several mitochondria-depleted fibers. However, the presence of COX-negative fibers, which are commonly observed in muscle biopsies from POLG patients, was not detected in the skeletal muscle of *Polg*$^{+/Y933C}$.

We did not observe mtDNA depletion or presence of multiple mtDNA deletions in the tissues of *Polg*$^{+/Y933C}$ mice. However, it has been previously reported that multiple deletions are rarely observed in mice (Tyynismaa et al., 2005), suggesting a stricter control of mtDNA quality in mice compared to humans.

In conclusion, our *in vivo* characterization indicates that the POLγA Y933C mutation causes a mild, late onset phenotype in mice. In future studies, it will be valuable to use some stressors to potentially induce a more severe phenotype. POLγB has been shown to stabilize POLγA in mice (Pinheiro et al., 2021). Crossing the Y933C with *P*olg*2*$^{+/-}$ mice may unravel new phenotypes. Additional interventions could be based on the use of pharmacological agents. For instance, LPS, a known inducer of fever, often inducing the disease in children with mitochondrial disease, will be tested. Notably, my in vitro data clearly indicate that the protein carrying the Y933C mutation has impaired DNA synthesis, which is not rescued by increased dNTPs concentrations. In contrast, DNA binding activity and interaction with POLγB are not impaired. Mouse cells, therefore, must cope with this mutation differently than their human counterparts, possibly by compensating for the defect in some way. Identifying the compensatory mechanism may open new avenues for the treatment of POLG-related disorders.

In addition, considering the wide spectrum of *POLG*-related disorders, we have now generated, by CRISPR/Cas9 genome editing, other knock-in mouse models reproducing the most common human pathogenic variants, including the recessive mutations G848S, W748S, and R302C. The *Polg*$^{W726S/W726S}$ mouse, carrying a mutation equivalent to the human W748S recessive variant, showed a mild myopathic phenotype. This is in contrast to the severe encephalomyopathies observed in patients. To more accurately replicate the human disease genotypes, we are in the process of creating compound heterozygous mice. It is noteworthy that most Alpers Huttenlocher syndrome patients possess either the W748S or A467T mutation alongside another *POLG* mutation, typically the G848S variant. Therefore, we are crossbreeding *Polg*$^{+/W726S}$ and *Polg*$^{+/A449T}$ mice with *Polg*$^{+/G826S}$ counterparts. We have successfully generated *Polg*$^{A449T/G826S}$ compound heterozygotes, instead the *Polg*$^{W726S/G826S}$ have not been born yet, which suggest that they are embryonic lethal. Initial observations suggest that the *Polg*$^{A449T/G826S}$ display decreased spontaneous activity in comparison to their WT siblings. It is important to note that the G826S mutation in mice is embryonic lethal in its homozygous form.

The identification of phenotypes similar to the human syndrome is thus challenging as the POLG mutants seem to be either embryonic lethal or show no clinical phenotype. However, the first step will be to carefully analyze the molecular phenotype of these models. MtDNA instability is a hallmark of POLG-related disorders and the presence of alterations in mtDNA copy number or of multiple deletions would be essential to test pharmacological and/or gene therapy approaches.

6. References

ALLEN, J. F. 2015. Why chloroplasts and mitochondria retain their own genomes and genetic systems: Colocation for redox regulation of gene expression. *Proc Natl Aca Sci the U S A,* 112, 10231-8.

ALLEN, J. F. 2017. The CoRR hypothesis for genes in organelles. J Theor Biol, 434, 50-57.

AMIOTT, E. A., & JAEHNING, J. A. 2006. Mitochondrial Transcription Is Regulated via an ATP "Sensing" Mechanism that Couples RNA Abundance to Respiration. *Mol Cell,* 22, 329-38.

ANDERSSON, S. G. E., ZOMORODIPOUR, A., ANDERSSON, J. O., SICHERITZ PONTÉN, T., ALSMARK, U. C. M., PODOWSKI, R. M., NÄSLUND, A. K., ERIKSSON, A., WINKLER, H. H., & KURLAND, C. G. 1998. The genome sequence of Rickettsia prowazekii and the origin of mitochondria. *Nature,* 396, 133-40.

BAERTLING, F., RODENBURG, R. J., SCHAPER, J., SMEITINK, J. A., KOOPMAN, W. J., MAYATEPEK, E., & MORAVA, V. 2013. A guide to diagnosis and treatment of Leigh syndrome. *J Neurol Neurosurg Psychiatry,* 85, 257-65.

BALDO, M. S., & VILARINHO, L. 2020. Molecular basis of Leigh syndrome: a current look. *Orphanet J Rare Dis,* 15, 31.

BARTLETT, J. S., WILCHER, R., & SAMULSKI, R. J. 2000. Infectious Entry Pathway of Adeno-Associated Virus and Adeno-Associated Virus Vectors. *J Virol,* 74, 2777-85.

BAUM, C., SCHAMBACH, A., BOHNE, J., & GALLA, M. 2006. Retrovirus Vectors: Toward the Plentivirus? *Mol Ther, 13,* 1050-63.

BESSIS, N., GARCÍA-COZAR, F., & MC, B. 2004. Immune responses to gene therapy vectors: influence on vector function and effector mechanisms. *Gene Ther,* 11, S10-7.

BIBB, M. J., VAN ETTEN, R. A., WRIGHT, C. T., WALBERG, M. W., & CLAYTON, D. A 1981. Sequence and gene organization of mouse mitochondrial DNA. *Cell,* 26, 167-80.

BOCZONADI, V., MEYER, K., GONCZAROWSKA-JORGE, H., GRIFFIN, H., ROOS, A., BARTSAKOULIA, M., BÁNSÁGI, B., RICCI, G., PALINKAS, F., ZAHEDI, R. P., BRUNI, F., KASPAR, B. K., LOCHMÜLLER, H., BOYCOTT, K. M., MÜLLER, J. S., & HORVATH, R. 2018. Mutations in glycyl-tRNA synthetase impair mitochondrial metabolism in neurons. *Hum Mol Genet,* 27, 2187-2204.

BONORA, M., PATERGNANI, S., RIMESSI, A., DE MARCHI, E., SUSKI, J. M., BONONI, A., GIORGI, C., MARCHI, S., MISSIROLI, S., POLETTI, F., WIECKOWSKI, M. R. & PINTON, P. 2012. ATP synthesis and storage. Purinergic Signal, 8, 343-57.

BRAND, M. D., & ESTEVES, T. C. 2005. Physiological functions of the mitochondrial uncoupling proteins UCP2 and UCP3. *Cell Metab,* 2, 85-93.

BUGIANI, M., INVERNIZZI, F., ALBERIO, S., BRIEM, E., LAMANTEA, E., CARRARA, F., MORONI, I., FARINA, L., SPADA, M., DONATI, M. A., UZIEL, G. & ZEVIANI, M. 2004. Clinical and molecular findings in children with complex I deficiency. *Biochim Biophys Acta,* 1659, 136-47.

BUGIARDINI, E., POOLE, O. V., MANOLE, A., PITTMAN, A. M., HORGA, A., HARGREAVES, I., WOODWARD, C. E., SWEENEY, M. G., HOLTON, J. L., TAANMAN, J. W., PLANT, G. T., POULTON, J., ZEVIANI, M., GHEZZI, D., TAYLOR, J., SMITH, C., FRATTER, C., KANIKANNAN, M. A., PARAMASIVAM, A., THANGARAJ, K., SPINAZZOLA, A., HOLT, I. J., HOULDEN, H., HANNA, M. G., & PITCEATHLY, R. D. S. 2017. Clinicopathologic and molecular spectrum of RNASEH1-related mitochondrial disease. *Neurol Genet,* 3, e149.

BUTOVSKY, O., & WEINER, H. L. 2018. Microglial signatures and their role in health and disease. *Nat Rev Neurosci,* 19, 622-635.

CAMPS, M., HERMAN, A., LOH, E. & LOEB, L. A. 2007. Genetic constraints on protein evolution. *Crit Rev Biochem Mol Biol,* 42, 313-26.

CANNON, B., & NEDERGAARD, J. 2004. Brown Adipose Tissue: Function and Physiological Significance. *Physiol Rev,* 84, 277-359.

CAVALIER-SMITH, T. 1987. The Origin of Eukaryote and Archaebacterial Cells. Ann N Y Acad Sci, 503, 17-54.

CERUTTI, R., PIRINEN, E., LAMPERTI, C., MARCHET, S., SAUVE, A. A., LI, W., LEONI, V., SCHON, E. A., DANTZER, F., AUWERX, J., VISCOMI, C., & ZEVIANI, M. 2014. NAD+-Dependent Activation of Sirt1 Corrects the Phenotype in a Mouse Model of Mitochondrial Disease. *Cell Metab,* 19, 1042-9.

CHACIŃSKA, A., KOEHLER, C. M., MILENKOVIC, D., LITHGOW, T., & PFANNER, N. 2009. Importing Mitochondrial Proteins: Machineries and Mechanisms. *Cell,* 138, 628-44.

CHAN, S. S., NAVIAUX, R. K., BASINGER, A., CASAS, K., & COPELAND, W. C. 2009. De novo mutation in POLG leads to haplotype insufficiency and Alpers syndrome. *Mitochondrion,* 9, 340-345.

CHAN, K. Y., JANG, M. J., YOO, B. H., GREENBAUM, A., RAVI, N., WU, W., SÁNCHEZ-GUARDADO, L. S., LOIS, C., MAZMANIAN, S. K., DEVERMAN, B. E., & GRADINARU, V. 2017. Engineered AAVs for efficient noninvasive gene delivery to the central and peripheral nervous systems. *Nat Neurosci,* 20, 1172-1179.

CHIABRANDO, D., VINCHI, F., FIORITO, V., MERCURIO, S. & TOLOSANO, E. 2014. Heme in pathophysiology: a matter of scavenging, metabolism and trafficking across cell membranes. Front Pharmacol, 5, 61.

CHINNERY, P. F., & ZEVIANI, M. 2008. 155th ENMC workshop: Polymerase gamma and disorders of mitochondrial DNA synthesis, 21–23 September 2007, Naarden, The Netherlands. Neuromuscular Disorders.

CHINNERY, P. F., ELLIOTT, H. R., HUDSON, G., SAMUELS, D. C., & RELTON, C. L. 2012. Epigenetics, epidemiology and mitochondrial DNA diseases. *Int J Epidemiol,* 41, 177-87.

CIVILETTO, G., DOĞAN, K. A., CERUTTI, R., FAGIOLARI, G., MOGGIO, M., LAMPERTI, C., BENINCÁ, C., VISCOMI, C., & ZEVIANI, M. 2018. Rapamycin rescues mitochondrial myopathy via coordinated activation of autophagy and lysosomal biogenesis. *EMBO Mol Med,* 10, e8799.

D'SOUZA, A. R., & MINCZUK, M. 2018. Mitochondrial transcription and translation: overview. *Essays Biochem,* 62, 309-320.

DEBALSI, K. L., LONGLEY, M. J., HOFF, K. E., & COPELAND, W. C. 2017. Synergistic Effects of the in cis T251I and P587L Mitochondrial DNA Polymerase γ Disease Mutations. *J Biol Chem,* 292, 4198-4209.

DEBRAY, F. G., MORIN, C., JANVIER, A., VILLENEUVE, J., MARANDA, B., LAFRAMBOISE, R., LACROIX, J., DÉCARIE, J., ROBITAILLE, Y., LAMBERT, M., ROBINSON, B. H., & MITCHELL, G. A. 2011. LRPPRC mutations cause a phenotypically distinct form of Leigh syndrome with cytochrome c oxidase deficiency. *J Med Genet,* 48, 183-9.

DI MEO, I., LAMPERTI, C., & TIRANTI, V. 2015. Mitochondrial diseases caused by toxic compound accumulation: from etiopathology to therapeutic approaches. *EMBO Mol Med,* 7, 1257-1266.

DI MEO, I., MARCHET, S., LAMPERTI, C., ZEVIANI, M., & VISCOMI, C. 2017. AAV9 based gene therapy partially ameliorates the clinical phenotype of a mouse model of Leigh syndrome. *Gene Ther,* 24, 661-667.

DIMAURO, S., & DAVIDZON, G. 2005. Mitochondrial DNA and disease. *Ann Med,* 37, 222-32.

DODA, J. N., WRIGHT, C. T. & CLAYTON, D. A. 1981. Elongation of displacement loop strands in human and mouse mitochondrial DNA is arrested near specific template sequences. Proc Natl Acad Sci U S A, 78, 6116-20.

DONG, J. Y., FAN, P., & FRIZZELL, R. A. 1996. Quantitative Analysis of the Packaging Capacity of Recombinant Adeno-Associated Virus. *Hum Gene Ther,* 7, 2101-12.

DRÖGE, W. 2002. Free Radicals in the Physiological Control of Cell Function. *Physiol Rev,* 82, 47-95.

DUAN, D., SHARMA, P., YANG, J., YUE, Y., DUDUS, L., ZHANG, Y., FISHER, K. J., & ENGELHARDT, J. F. 1998. Circular Intermediates of Recombinant Adeno-Associated Virus Have Defined Structural Characteristics Responsible for Long-Term Episomal Persistence in Muscle Tissue. *J Virol,* 72, 8568-77.

DZBEK, J. & KORZENIEWSKI, B. 2008. Control over the contribution of the mitochondrial membrane potential (DeltaPsi) and proton gradient (DeltapH) to the protonmotive force (Deltap). In silico studies. J Biol Chem, 283, 33232-9.

EGGEN, B. J. L., RAJ, D., HANISCH, U., & BODDEKE, H. 2013. Microglial Phenotype and Adaptation. *J Neuroimmune Pharmacol,* 8, 807-23.

EMBLEY, T. M., & MARTIN, W. 2006. Eukaryotic evolution, changes and challenges. *Nature,* 440, 623-30.

ERNSTER, L., & SCHATZ, G. 1981. Mitochondria: a historical review. *J Cell Biol,* 91, 227s-255s.

FALKENBERG, M., LARSSON, N., & GUSTAFSSON, C. M. 2007. DNA Replication and Transcription in Mammalian Mitochondria. *Annu Rev Biochem,* 76, 679-99.

FERRARI, F. K., SAMULSKI, T. V., SHENK, T., & SAMULSKI, R. J. 1996. Second-strand synthesis is a rate-limiting step for efficient transduction by recombinant adeno-associated virus vectors. *J Virol,* 70, 3227-34.

FERRARI, G., LAMANTEA, E., DONATI, A., FILOSTO, M., BRIEM, E., CARRARA, F., PARINI, R., SIMONATI, A., SANTER, R., & ZEVIANI, M. 2005. Infantile hepatocerebral syndromes associated with mutations in the mitochondrial DNA polymerase- A. *Brain,* 128, 723-31.

FINKEL, T., & HOLBROOK, N. J. 2000. Oxidants, oxidative stress and the biology of ageing. *Nature,*408, 239-47.

FISHER, K. J., KELLEY, W. M., BURDA, J. F., & WILSON, J. M. 1996. A Novel Adenovirus—Adeno-Associated Virus Hybrid Vector That Displays Efficient Rescue and Delivery of the AAV Genome. *Hum Gene Ther,* 7, 2079-87.

FIX, A. S., ROSS, J. F., STITZEL, S. R., & SWITZER, R. C. 1996. Integrated Evaluation of Central Nervous System Lesions: Stains for Neurons, Astrocytes, and Microglia Reveal the Spatial and Temporal Features of MK-801-induced Neuronal Necrosis in the Rat Cerebral Cortex. *Toxicol Pathol,* 24, 291-304.

FREY, T., & MANNELLA, C. A. 2000. The internal structure of mitochondria. *Trends Biochem Sci,* 25, 319-24.

FUSTÉ, J. M., WANROOIJ, S., JEMT, E., GRANYCOME, C., CLUETT, T. J., SHI, Y., ATANASSOVA, N., HOLT, I., GUSTAFSSON, C. M., & FALKENBERG, M. 2010. Mitochondrial RNA Polymerase Is Needed for Activation of the Origin of Light-Strand DNA Replication. *Mol Cell,* 37, 67-78.

FUSTÉ, J. M., SHI, Y., WANROOIJ, S., ZHU, X., JEMT, E., PERSSON, R., SABOURI, N., GUSTAFSSON, C. M., & FALKENBERG, M. 2014. In Vivo Occupancy of Mitochondrial Single-Stranded DNA Binding Protein Supports the Strand Displacement Mode of DNA Replication. *PLoS Genet,* 10, e1004832.

GHEZZI, D., & ZEVIANI, M. 2018. Human diseases associated with defects in assembly of OXPHOS complexes. *Essays Biochem,* 62, 271-286.

GIORDANO, C., MONTOPOLI, M., PERLI, E., ORLANDI, M., FANTIN, M., ROSS CISNEROS, F. N., CAPARROTTA, L., MARTINUZZI, A., RAGAZZI, E., GHELLI, A., SADUN, A. A., D’AMATI, G., & CARELLI, V. 2010. Oestrogens ameliorate mitochondrial dysfunction in Leber’s hereditary optic neuropathy. *Brain,* 134, 220-34.

GIORDANO, C., IOMMARINI, L., GIORDANO, L., MARESCA, A., PISANO, A., VALENTINO, M. L., CAPORALI, L., LIGUORI, R., DECEGLIE, S., ROBERTI, M., FANELLI, F., FRACASSO, F., ROSS-CISNEROS, F. N., D'ADAMO, P., HUDSON, G., PYLE, A., YU- WAI-MAN, P., CHINNERY, P. F., ZEVIANI, M., SALOMAO, S. R., BEREZOVSKY, A., BELFORT, R., JR., VENTURA, D. F., MORAES, M., MORAES FILHO, M., BARBONI, P., SADUN, F., DE NEGRI, A., SADUN, A. A., TANCREDI, A., MANCINI, M., D'AMATI, G., LOGUERCIO POLOSA, P., CANTATORE, P. & CARELLI, V. 2014. Efficient mitochondrial biogenesis drives incomplete penetrance in Leber's hereditary optic neuropathy. Brain, 137, 335-53.

GORMAN, G., CHINNERY, P. F., DIMAURO, S., HIRANO, M., KOGA, Y., MCFARLAND, R., SUOMALAINEN, A., THORBURN, D. R., ZEVIANI, M., & TURNBULL, D. M. 2016. Mitochondrial diseases. *Nat Rev Dis Primers,* 2, 16080.

GREEN, D. R., & REED, J. C. 1998. Mitochondria and Apoptosis. *Science,* 281, 1309-12.

GUSTAFSSON, C. M., FALKENBERG, M., & LARSSON, N. 2016. Maintenance and Expression of Mammalian Mitochondrial DNA. *Annu Rev Biochem,* 85, 133-60.

HAKONEN, A. H., HEISKANEN, S., JUVONEN, V., LAPPALAINEN, I., LUOMA, P., RANTAMÄKI, M., VAN GOETHEM, G., LÖFGREN, A., HACKMAN, P., PAETAU, A., KAAKKOLA, S., MAJAMAA, K., VARILO, T., UDD, B., KÄÄRIÄINEN, H., BINDOFF, L. A., & SUOMALAINEN, A. 2005. Mitochondrial DNA Polymerase W748S Mutation: A Common Cause of Autosomal Recessive Ataxia with Ancient European Origin. *Am J Hum Genet,* 77, 430-41.

HANCE, N., EKSTRAND, M. I., & TRIFUNOVIĆ, A. 2005. Mitochondrial DNA polymerase gamma is essential for mammalian embryogenesis. *Hum Mol Genet,* 14, 1775-83.

HENGARTNER, M. O. 2000. The biochemistry of apoptosis. *Nature,* 407, 770-6. KROEMER, G., GALLUZZI, L., & BRENNER, C. 2007. Mitochondrial Membrane Permeabilization in Cell Death. *Physiol Rev,* 87, 99-163.

HOLMES, J. B., AKMAN, G., WOOD, S., SAKHUJA, K., CERRITELLI, S. M., MOSS, C. F., BOWMAKER, M., JACOBS, H. T., CROUCH, R. J., & HOLT, I. 2015. Primer retention owing to the absence of RNase H1 is catastrophic for mitochondrial DNA replication. *Proc Natl Acad Sci U S A,* 112, 9334-9.

HOLT, I., HARDING, A. E., & MORGAN-HUGHES, J. A. 1988. Deletions of muscle mitochondrial DNA in patients with mitochondrial myopathies. *Nature,* 25, 717-9.

HOLT, I., LORIMER, H. E., & JACOBS, H. T. 2000. Coupled Leading- and Lagging Strand Synthesis of Mammalian Mitochondrial DNA. *Cell,* 100, 515-24.

HOPPINS, S., LACKNER, L. L., & NUNNARI, J. 2007. The Machines that Divide and Fuse Mitochondria. *Annu Rev Biochem,* 76, 751-80.

HORDEAUX, J., YUAN, Y., CLARK, P. M., WANG, Q., MARTINO, R., SIMS, J. J., BELL, P., RAYMOND, A., STANFORD, W. L., & WILSON, J. M. 2019. The GPI-Linked Protein LY6A Drives AAV-PHP.B Transport across the Blood-Brain Barrier. *Mol Ther,* 27, 912-921.

HUANG, J., LI, X., COELHO-DOS-REIS, J. G. A., WILSON, J. M., & TSUJI, M. 2014. An AAV Vector-Mediated Gene Delivery Approach Facilitates Reconstitution of Functional Human CD8+ T Cells in Mice. *PLoS ONE,* 9, e88205.

JAIN, I. H., ZAZZERON, L., GOLI, R., ALEXA, K., SCHATZMAN-BONE, S., DHILLON, H., GOLDBERGER, O., PENG, J., SHALEM, O., SANJANA, N. E., ZHANG, F., GOESSLING, W., ZAPOL, W. M., & MOOTHA, V. K. 2016. Hypoxia as a therapy for mitochondrial disease. *Science,* 352, 54-61.

JAIN, I. H., ZAZZERON, L., GOLDBERGER, O., MARUTANI, E., WOJTKIEWICZ, G. R., AST, T., WANG, H., SCHLEIFER, G., СТЕПАНОВА, BREPOELS, K., SCHOONJANS, L., CARMELIET, P., GALKIN, A., ICHINOSE, F., ZAPOL, W. M., & MOOTHA, V. K. 2019. Leigh Syndrome Mouse Model Can Be Rescued by Interventions that Normalize Brain Hyperoxia, but Not HIF Activation. *Cell Metab,* 30, 824-832.e3.

KAGUNI, L. S. 2004. DNA Polymerase γ, The Mitochondrial Replicase. *Annu Rev Biochem,* 73, 293-320.

KASIVISWANATHAN, R., LONGLEY, M. J., CHAN, S. S., & COPELAND, W. C. 2009. Disease Mutations in the Human Mitochondrial DNA Polymerase Thumb Subdomain Impart Severe Defects in Mitochondrial DNA Replication. *J Biol Chem,* 284, 19501-10.

KAY, M. A., GLORIOSO, J. C., & NALDINI, L. 2001. Viral vectors for gene therapy: the art of turning infectious agents into vehicles of therapeutics. *Nat Med,* 7, 33-40.

KETTENMANN, H., HANISCH, U., НОДА, & VERKHRATSKY, A. 2011. Physiology of Microglia. *Physiol Rev,* 91, 461-553.

KOENE, S., RODENBURG, R. J., VAN DER KNAAP, M. S., WILLEMSEN, M., SPERL, W., LAUGEL, V., ØSTERGAARD, E., TARNOPOLSKY, M. A., MARTÍN, M., NESBITT, V., FLETCHER, J. M., EDVARDSON, S., PROCACCIO, V., SLAMA, A., VAN DEN HEUVEL, L., & SMEITINK, J. A. 2012. Natural disease course and genotype-phenotype correlations in Complex I deficiency caused by nuclear gene defects: what we learned from 130 cases. *J Inherit Metab Dis,* 35, 737-747.

KORHONEN, J., PHAM, X. H., PELLEGRINI, M., & FALKENBERG, M. 2004. Reconstitution of a minimal mtDNA replisome in vitro. *EMBO J,* 23, 2423-2429.

KOSHIBA, T., DETMER, S. A., KAISER, J. T., CHEN, H., MCCAFFERY, J. M., & CHAN, D. C. 2004. Structural Basis of Mitochondrial Tethering by Mitofusin Complexes. *Science,* 305, 858-62.

KRUSE, S. E., WATT, W. C., MARCINEK, D. J., KAPUR, R. P., SCHENKMAN, K. A., & PALMITER, R. D. 2008. Mice with Mitochondrial Complex I Deficiency Develop a Fatal Encephalomyopathy. *Cell Metab,* 7, 312-20.

KU, C., NELSON-SATHI, S., ROETTGER, M., SOUSA, F. L., LOCKHART, P. J., BRYANT, D., HAZKANI-COVO, E., MCINERNEY, J. O., LANDAN, G., & MARTIN, W. 2015. Endosymbiotic origin and differential loss of eukaryotic genes. *Nature,* 524, 427-32.

KUNJI, E. R. S. 2004. The role and structure of mitochondrial carriers. *FEBS Lett,* 564, 239-44.

KUNJI, E. R., ALEKSANDROVA, A., KING, M. S., MAJD, H., ASHTON, V. L., CERSON, E., SPRINGETT, R., KIBALCHENKO, M., TAVOULARI, S., CRICHTON, P. G. & RUPRECHT, J. J. 2016. The transport mechanism of the mitochondrial ADP/ATP carrier. Biochim Biophys Acta, 1863, 2379-93.

LANE, N., & MARTIN, W. 2010. The energetics of genome complexity. *Nature,* 467, 929-34.

LEIGH, D. 1951. Subacute necrotizing encephalomyelopathy in an infant. *J Neurol Neurosurg Psychiatry,* 14, 216-21.

LING, Q., HERSTINE, J. A., BRADBURY, A. M., & GRAY, S. J. 2023. AAV-based in vivo gene therapy for neurological disorders. *Nature Reviews Drug Discovery,* 22, 789-806.

LUFT, R., IKKOS, D., PALMIERI, G. M. A., ERNSTER, L., & AFZELIUS, B. A. 1962. A case of severe hypermetabolism of nonthyroid origin with a defect in the maintenance of mitochondrial respiratory control: a correlated clinical, biochemical, and morphological study. *J Clin Invest,* 41, 1776-804.

LUOMA, P., MELBERG, A., RINNE, J. O., KAUKONEN, J., NUPPONEN, N. N., CHALMERS, R. M., OLDFORS, A., RAUTAKORPI, I., PELTONEN, L., MAJAMAA, K., SOMER, H., & SUOMALAINEN, A. 2004. Parkinsonism, premature menopause, and mitochondrial DNA polymerase γ mutations: clinical and molecular genetic study. *Lancet,* 364, 875-82.

MAIO, N. & ROUAULT, T. A. 2015. Iron-sulfur cluster biogenesis in mammalian cells: New insights into the molecular mechanisms of cluster delivery. Biochim Biophys Acta, 1853, 1493-512.

MCCARRON, J. G., WILSON, C., SANDISON, M. E., OLSON, M. L., GIRKIN, J. M., SAUNTER, C. & CHALMERS, S. 2013. From structure to function: mitochondrial morphology, motion and shaping in vascular smooth muscle. J Vasc Res, 50, 357-71.

MEDINA, L., CHI, T. L., DEVIVO, D. C., & HILAL, S. K. 1990. MR findings in patients with subacute necrotizing encephalomyelopathy (Leigh syndrome): correlation with biochemical defect. *AJNR Am J Neuroradiol,* 11, 379–84.

MITCHELL, P. 1961. Coupling of Phosphorylation to Electron and Hydrogen Transfer by a Chemi-Osmotic type of Mechanism. *Nature,* 191, 144-8.

MONTOYA, J., CHRISTIANSON, T., LEVENS, D., RABINOWITZ, M. & ATTARDI, G. 1982. Identification of initiation sites for heavy-strand and light-strand transcription in human mitochondrial DNA. *Proc Natl Acad Sci U S A,* 79, 7195-9.

MORENBERG MD. The reactive astrocyte. In: Aschner M, Costa LG, eds. The Role of Glia in Neurotoxicity. Boca Raton, FL: CRC Press; 2005:73–92.

NALDINI, L. 2011. Ex vivo gene transfer and correction for cell-based therapies. *Nat Rev Genet,* 12, 301-15.

NALDINI, L. 2015. Gene therapy returns to centre stage. *Nature,* 15, 351-60.

NARENDRA, D. P., TANAKA, A., SUEN, D. F., & YOULE, R. J. 2008. Parkin is recruited selectively to impaired mitochondria and promotes their autophagy. *J Cell Biol,* 183, 795-803.

NEEVE, V. C., SAMUELS, D. C., BINDOFF, L. A., VAN DEN BOSCH, B., VAN GOETHEM, G., SMEETS, H., LOMBÈS, A., JARDEL, C., HIRANO, M., DIMAURO, S., DE VRIES, M., SMEITINK, J. A., SMITS, B. W., DE COO, I., SAFT, C., KLOPSTOCK, T., KEILING, B. C., CZERMIN, B., ABICHT, A., LOCHMÜLLER, H., HUDSON, G., GORMAN, G. G., TURNBULL, D. M., TAYLOR, R. W., HOLINSKI-FEDER, E., CHINNERY, P. F., & HORVATH, R. 2012. What is influencing the phenotype of the common homozygous polymerase-γ mutation p.Ala467Thr? *Brain,* 135, 3614-26.

NEUPERT, W. & HERRMANN, J. M. 2007. Translocation of proteins into mitochondria. *Annu Rev Biochem,* 76, 723-49.

NICHOLLS, T. J., & MINCZUK, M. 2014. In D-loop: 40 years of mitochondrial 7S DNA. *Exp Geront,* 56, 175-81.

NISHINO, I., SPINAZZOLA, A., & HIRANO, M. 1999. Thymidine Phosphorylase Gene Mutations in MNGIE, a Human Mitochondrial Disorder. *Science,* 283, 689-92.

NURMINEN, A., FARNUM, G. A., & KAGUNI, L. S. 2017. Pathogenicity in POLG syndromes: DNA polymerase gamma pathogenicity prediction server and database. *BBA Clin,* 7, 147-156.

O'CALLAGHAN, J. P., & SRIRAM, K. 2005. Glial fibrillary acidic protein and related glial proteins as biomarkers of neurotoxicity. *Expert Opin Drug Saf,* 4, 433-42.

OGILVIE, I., KENNAWAY, N. G., & SHOUBRIDGE, E. A. 2005. A molecular chaperone for mitochondrial complex I assembly is mutated in a progressive encephalopathy. *J Clin Invest,* 115, 2784-92.

OJALA, D., MONTOYA, J., & ATTARDI, G. 1981. tRNA punctuation model of RNA processing in human mitochondria. *Nature,* 290, 470-4.

OLÁHOVÁ, M., HARDY, S. A., HALL, J., YARHAM, J. W., HAACK, T. B., WILSON, W. C., ALSTON, C. L., HE, L., AZNAURYAN, E., BROWN, R., BROWN, G. K., MORRIS, A. A. M., MUNDY, H., BROOMFIELD, A., BARBOSA, I. A., SIMPSON, M. A., DESHPANDE, C., MOESLINGER, D., KOCH, J., STETTNER G. M., BONNEN, P. E., PROKISCH, H., LIGHTOWLERS, R. N., MCFARLAND, R., CHRZANOWSKA-LIGHTOWLERS, Z. M. A., & TAYLOR, R. W. 2015. LRPPRC mutations cause early-onset multisystem mitochondrial disease outside of the French-Canadian population. *Brain,* 138, 3503-3519.

OSAWA, S., JUKES, T. H., WATANABE, K., & MUTO, A. 1992. Recent evidence for evolution of the genetic code. *Microbiol Rev,* 56, 229-64.

PAGLIARINI, D. J. & RUTTER, J. 2013. Hallmarks of a new era in mitochondrial biochemistry. Genes Dev, 27, 2615-27.

PAGNAMENTA, A. T., TAANMAN, J., WILSON, C., ANDERSON, N. E., MAROTTA, R., DUNCAN, A., BITNER-GLINDZICZ, M., TAYLOR, R. W., LASKOWSKI, A., THORBURN, D. R., & RAHMAN, S. 2006. Dominant inheritance of premature ovarian failure associated with mutant mitochondrial DNA polymerase gamma. *Hum Reprod,* 21, 2467-73.

PALADE, G. E. 1953. AN ELECTRON MICROSCOPE STUDY OF THE MITOCHONDRIAL STRUCTURE. *J Histochem and Cytochem,* 1, 188-211.

PAPA, S., DE RASMO, D., SCACCO, S., SIGNORILE, A., TECHNIKOVA-DOBROVA, Z., PALMISANO, G., SARDANELLI, A. M., PAPA, F., PANELLI, D., SCARINGI, R., & SANTERAMO, A. 2008. Mammalian complex I: A regulable and vulnerable pacemaker in mitochondrial respiratory function. *Biochim Biophys Acta,* 1777, 719-28.

PAYNE, B., WILSON, I. J., YU-WAI-MAN, P., COXHEAD, J., DEEHAN, D. J., HORVATH, R., TAYLOR, R. W., SAMUELS, D. C., SANTIBANEZ-KOREF, M., & CHINNERY, P. F. 2012. Universal heteroplasmy of human mitochondrial DNA. *Hum Mol Genet,* 22, 384-90.

PICKETT, S. J., GRADY, J. P., NG, Y. S., GORMAN, G., SCHAEFER, A. M., WILSON, I. J., CORDELL, H. J., TURNBULL, D. M., TAYLOR, R. W., & MCFARLAND, R. 2018. Phenotypic heterogeneity in m.3243A>G mitochondrial disease: The role of nuclear factors. *Ann Clin and Transl Neurol,* 5, 333-345.

PINCUS, J. H. 1972. Subacute necrotizing encephalomyelopathy (Leigh's disease): a consideration of clinical features and etiology. *Dev Med Child Neurol,* 14, 87–101.

SILVA-PINHEIRO, P., PARDO-HERNÁNDEZ, C., REYES, A., TILOKANI, L., MISHRA, A., CERUTTI, R., LI, S., ROZSIVALOVA, D. H., VALENZUELA, S., DOĞAN, K. A., PETER, B., FERNÁNDEZ-SILVA, P., TRIFUNOVIĆ, A., PRUDENT, J., MINCZUK, M., BINDOFF, L. A., MACAO, B., ZEVIANI, M., FALKENBERG, M., & VISCOMI, C. 2021. DNA polymerase gamma mutations that impair holoenzyme stability cause catalytic subunit depletion. *Nucleic Acids Res,* 49, 5230-5248.

POLYÁK, E., OSTROVSKY, J., PENG, M., DINGLEY, S. D., TSUKIKAWA, M., KWON, Y. J., MCCORMACK, S. E., BENNETT, M. J., XIAO, R., SEILER, C., ZHANG, Z., & FALK, M. J. 2018. N-acetylcysteine and vitamin E rescue animal longevity and cellular oxidative stress in pre-clinical models of mitochondrial complex I disease. *Mol Genet Metab,* 123, 449-462.

PONAMAREV, M. V., LONGLEY, M. J., NGUYEN, D. C., KUNKEL, T. A., & COPELAND, W. C. 2002. Active Site Mutation in DNA Polymerase γ Associated with Progressive External Ophthalmoplegia Causes Error-prone DNA Synthesis. *J Biol Chem,* 277, 15225-8.

QUINTANA, A., KRUSE, S. E., KAPUR, R. P., SANZ, E., & PALMITER, R. D. 2010. Complex I deficiency due to loss of Ndufs4 in the brain results in progressive encephalopathy resembling Leigh syndrome. *Proc Natl Acad Sci U S A,* 107, 10996-1001.

RAHMAN, S., BLOK, R. B., DAHL, H. H. M., DANKS, D. M., KIRBY, D. M., CHOW, C. W., CHRISTODOULOU, J., & THORBURN, D. R. 1996. Leigh syndrome: Clinical features and biochemical and DNA abnormalities. *Ann Neurol,* 39, 343-51.

RAHMAN, S. 2012. Mitochondrial disease and epilepsy. *Dev Med Child Neurol,* 54, 397-406.

RAHMAN, S., & COPELAND, W. C. 2018. POLG-related disorders and their neurological manifestations. *Nat Rev Neurol,* 15, 40-52.

RAJAKULENDRAN, S., PITCEATHLY, R. D. S., TAANMAN, J., COSTELLO, H., SWEENEY, M. G., WOODWARD, C. E., JAUNMUKTANE, Z., HOLTON, J. L., JACQUES, T. S., HARDING, B., FRATTER, C., HANNA, M. G., & RAHMAN, S. 2016. A Clinical, Neuropathological and Genetic Study of Homozygous A467T POLG-Related Mitochondrial Disease. *PLoS ONE,* 11, e0145500.

REYES, A., KAZAK, L., WOOD, S., YASUKAWA, T., JACOBS, H. T., & HOLT, I. 2013. Mitochondrial DNA replication proceeds via a 'bootlace' mechanism involving the incorporation of processed transcripts. *Nucleic Acids Res,* 41, 5837-50.

RICHTER-DENNERLEIN, R., OELJEKLAUS, S., LORENZI, I., RONSÖR, C., BARETH, B., SCHENDZIELORZ, A. B., WANG, C., WARSCHEID, B., REHLING, P., & DENNERLEIN, S. 2016. Mitochondrial Protein Synthesis Adapts to Influx of Nuclear-Encoded Protein. *Cell,* 167, 471-83.

ROBBERSON, D. L., & CLAYTON, D. A. 1972. Replication of Mitochondrial DNA in Mouse L Cells and Their Thymidine Kinase - Derivatives: Displacement Replication on a Covalently-Closed Circular Template. *Proc Natl Acad Sci U S A,* 69, 3810-4.

ROBBERSON, D. L., KASAMATSU, H., & VINOGRAD, J. 1972. Replication of Mitochondrial DNA. Circular Replicative Intermediates in Mouse L Cells. *Proc Natl Acad Sci U S A,* 69, 737-41.

SACCONE, C., DE GIORGI, C., GISSI, C., PESOLE, G., & REYES, A. 1999. Evolutionary genomics in Metazoa: the mitochondrial DNA as a model system. *Gene,* 238, 195-209.

SAGAN, L. 1967. On the origin of mitosing cells. *J Theor Biol,* 14, 255-74.

SARASTE, M. 1999. Oxidative Phosphorylation at the fin de siècle. *Science,* 283, 1488-93.

SARZI, E., SEVENO, M., PIRO-MÉGY, C., ELZIÈRE, L., QUILÈS, M., PÉQUIGNOT, M. O., MÜLLER, A., HAMEL, C., LENAERS, G., & DELETTRE, C. 2018. OPA1 gene therapy prevents retinal ganglion cell loss in a Dominant Optic Atrophy mouse model. *Scientific Reports,* 8, 2468.

SEGEL, M. J., LASH, B., SONG, J., LADHA, A., LIU, C. C., JIN, X., MEKHEDOV, S., MACRAE, R. K., KOONIN, E. V., & ZHANG, F. 2021. Mammalian retrovirus-like protein PEG10 packages its own mRNA and can be pseudotyped for mRNA delivery. *Science,* 373, 882-889.

SIEGMUND, S., YANG, H., SHARMA, R., JAVORS, M. A., SKINNER, O. S., MOOTHA, V. K., HIRANO, M., & SCHON, E. A. 2017. Low-dose rapamycin extends lifespan in a mouse model of mtDNA depletion syndrome. *Hum Mol Gen,* 26, 4588-4605.

SIEKEVITZ, P. 1957. Powerhouse of the Cell. Scientific American.

SCHELL, J. C., OLSON, K. A., JIANG, L., HAWKINS, A. B., VAN VRANKEN, J. G., XIE, J., EGNATCHIK, R. A., EARL, E. G., DEBERARDINIS, R. J., & RUTTER, J. 2014. A Role for the Mitochondrial Pyruvate Carrier as a Repressor of the Warburg Effect and Colon Cancer Cell Growth. *Mol Cell,* 56, 400-413.

SILVA-PINHEIRO, P., CERUTTI, R., LUNA-SÁNCHEZ, M., ZEVIANI, M., & VISCOMI, C. 2020. A Single Intravenous Injection of AAV-PHP.B-hNDUFS4 Ameliorates the Phenotype of Ndufs4 Mice. *Mol Ther Methods Clin Dev,* 17, 1071-1078.

SOFOU, K., DE COO, I., ISOHANNI, P., ØSTERGAARD, E., NAESS, K., DE MEIRLEIR, L., TZOULIS, C., UUSIMAA, J., DE ANGST, I. B., LÖNNQVIST, T., PIHKO, H., MANKINEN, K., BINDOFF, L. A., TULINIUS, M., & DARÍN, N. 2014. A multicenter study on Leigh syndrome: disease course and predictors of survival. *Orphanet J Rare Dis,* 9, 52.

SONNTAG, F., SCHMIDT, K., & KLEINSCHMIDT, J. A. 2010. A viral assembly factor promotes AAV2 capsid formation in the nucleolus. *Proc Natl Acad Sci U S A,* 107, 10220-5.

SPELBRINK, J. N. 2010. Functional organization of mammalian mitochondrial DNA in nucleoids: History, recent developments, and future challenges. *IUBMB Life,* 62, 19-32.

SPINAZZOLA, A., & ZEVIANI, M. 2009. Disorders from perturbations of nuclear mitochondrial intergenomic cross-talk. *J Intern Med,* 265, 174-92.

STENTON, S. L., & PROKISCH, H. 2018. Advancing genomic approaches to the molecular diagnosis of mitochondrial disease. *Essays Biochem,* 62, 399-408.

STENTON, S. L., & PROKISCH, H. 2020. Genetics of mitochondrial diseases: Identifying mutations to help diagnosis. *EBioMedicine,* 56, 102784.

STEWART, J. B., & CHINNERY, P. F. 2015. The dynamics of mitochondrial DNA heteroplasmy: implications for human health and disease. *Nat Rev Genet,* 16, 530-542.

STEWART, J. B., & CHINNERY, P. F. 2020. Extreme heterogeneity of human mitochondrial DNA from organelles to populations. *Nat Rev Genet,* 22, 106-118.

TAANMAN, J. 1999. The mitochondrial genome: structure, transcription, translation and replication. *Biochim Biophys Acta,* 1410, 103-23.

TATUCH Y., CHRISTODOULOU J., FEIGENBAUM A., CLARKE J. T., WHERRET J., SMITH C., RUDD N., PETROVA-BENEDICT R., & ROBINSON B. H. 1992. Heteroplasmic mtDNA mutation (T----G) at 8993 can cause Leigh disease when the percentage of abnormal mtDNA is high. *Am J Hum Genet,* 50, 852-8.

THORBURN, D. R. 2004. Mitochondrial disorders: Prevalence, myths and advances. *J Inherit Metab Dis,* 27, 349-62.

TORRES-TORRONTERAS, J., CABRERA-PÉREZ, R., VILA-JULIÀ, F., VISCOMI, C., CÁMARA, Y., HIRANO, M., ZEVIANI, M., & MARTÍ, R. 2018. Long-Term Sustained Effect of Liver-Targeted Adeno-Associated Virus Gene Therapy for Mitochondrial Neurogastrointestinal Encephalomyopathy. *Hum Gene Ther,* 29, 708-718.

TRIFUNOVIĆ, A., WREDENBERG, A., FALKENBERG, M., SPELBRINK, J. N., ROVIO, A. T., BRUDER, C. E., BOHLOOLY-Y, M., GIDLÖF, S., OLDFORS, A., WIBOM, R., TÖRNELL, J., JACOBS, H. T., & LARSSON, N. 2004. Premature ageing in mice expressing defective mitochondrial DNA polymerase. *Nature,* 429, 417-23.

TYYNISMAA, H., MJØSUND, K. P., WANROOIJ, S., LAPPALAINEN, I., YLIKALLIO, E., JALANKO, A., SPELBRINK, J. N., PAETAU, A., & SUOMALAINEN, A. 2005. Mutant mitochondrial helicase Twinkle causes multiple mtDNA deletions and a late-onset mitochondrial disease in mice. *Proc Natl Acad Sci U S A,* 102, 17687-92.

UUSIMAA, J., GOWDA, V., MCSHANE, A., SMITH, C., EVANS, J., SHRIER, A., NARASIMHAN, M., O'ROURKE, A., RAJABALLY, Y., HEDDERLY, T., COWAN, F., FRATTER, C., & POULTON, J. 2013. Prospective study of *POLG* mutations presenting in children with intractable epilepsy: Prevalence and clinical features. *Epilepsia,* 54, 1002-1011.

VAN DEN AMEELE, J., LI, A. Y. Z., MA, H., & CHINNERY, P. F. 2020. Mitochondrial heteroplasmy beyond the oocyte bottleneck. *Semin Cell Dev Biol,* 97, 156-166.

VAN GOETHEM, G., DERMAUT, B., LÖFGREN, A., MARTIN, J. J., & VAN BROECKHOVEN, C. 2001. Mutation of POLG is associated with progressive external ophthalmoplegia characterized by mtDNA deletions. *Nat Genetic,* 28, 211-2.

VENDELIN, M., BÉRAUD, N., GUERRERO, K., ANDRIENKO, T., KUZNETSOV, A. V., OLIVARES, J., KAY, L., & SAKS, V. 2005. Mitochondrial regular arrangement in muscle cells: a “crystal-like” pattern. *Am J Physiol Cell Physiol,* 288, C757-67.

VISCOMI, C., BOTTANI, E., CIVILETTO, G., CERUTTI, R., MOGGIO, M., FAGIOLARI, G., SCHON, E. A., LAMPERTI, C., & ZEVIANI, M. 2011. In Vivo Correction of COX Deficiency by Activation of the AMPK/PGC-1α Axis. *Cell Metab,* 14, 80-90.

VISCOMI, C., & ZEVIANI, M. 2017. MtDNA-maintenance defects: syndromes and genes. *J Inherit Metab Dis,* 40, 587-599.

VISCOMI, C., & ZEVIANI, M. 2020. Strategies for fighting mitochondrial diseases. *J Intern Med,* 287, 665-684.

WALKER, J. E. 2013. The ATP synthase: the understood, the uncertain and the unknown. Biochem Soc Trans, 41, 1-16.

WALLACE, D. C., SINGH, G., LOTT, M. T., HODGE, J. A., SCHURR, T. G., LEZZA, A. M. S., ELSAS, L. J., & NIKOSKELAINEN, E. 1988. Mitochondrial DNA Mutation Associated with Leber’s Hereditary Optic Neuropathy. *Science,* 242, 1427-30.

WALLACE, D. C. 1999. Mitochondrial disease in man and mouse. *Science,* 283, 1482-8.

WANG, Z., HI, M., LI, J., SUN, L., ZHANG, J., & XIAO, X. 2003. Rapid and highly efficient transduction by double-stranded adeno-associated virus vectors in vitro and in vivo. *Gene Ther,* 10, 2105-11.

WANG, D., TAI, P. W. L., & GAO, G. 2019. Adeno-associated virus vector as a platform for gene therapy delivery. *Nat Rev Drug Discov,* 18, 358-378.

WANROOIJ, S., FUSTÉ, J. M., FARGE, G., SHI, Y., GUSTAFSSON, C. M., & FALKENBERG, M. 2008. Human mitochondrial RNA polymerase primes lagging-strand DNA synthesis in vitro. *Proc Natl Acad Sci U S A,* 105, 11122-7.

WEI, W., & CHINNERY, P. F. 2020. Inheritance of mitochondrial DNA in humans: implications for rare and common diseases. *J Intern Med,* 287, 634-644.

WIEDEMANN, N., FRAZIER, A. E., & PFANNER, N. 2004. The Protein Import Machinery of Mitochondria. *J Biol Chem,* 279, 14473-6.

WONG, L. J., NAVIAUX, R. K., BRUNETTI-PIERRI, N., ZHANG, Q., SCHMITT, R., TRUONG, C. K.,MILONE, M., COHEN, B. H., WICAL, B., GANESH, J., BASINGER, A., BURTON, B. K., SWOBODA, K. J., GILBERT, D. L., VANDERVER, A., SANETO, R. P., MARANDA, B., ARNOLD, G., ABDENUR, J. E., WATERS, P. J., & COPELAND, W. C. 2008. Molecular and clinical genetics of mitochondrial diseases due to POLG mutations. *Hum Mut,* 29, E150-72.

WOODBRIDGE, P., LIANG, C., DAVIS, R. L., VANDEBONA, H., & SUE, C. M. 2013. POLG mutations in Australian patients with mitochondrial disease. *Intern Med J,* 43, 150-6.

YANG, D., OYAIZU, Y., OYAIZU, H., OLSEN, G. J., & WOESE, C. R. 1985. Mitochondrial origins. *Proc Natl Acad Sci USA,* 82, 4443-7.

YIN, H., XUE, W., CHEN, S., BOGORAD, R. L., BENEDETTI, E., GROMPE, M., KOTELIANSKY, V., SHARP, P. A., JACKS, T., & ANDERSON, D. G. 2014. Genome editing with Cas9 in adult mice corrects a disease mutation and phenotype. *Nat Biotechnol,* 32, 551-3.

ZEVIANI, M., SERVIDEI, S., GELLERA, C., BERTINI, E., DIMAURO, S. & DIDONATO, S. 1989. An autosomal dominant disorder with multiple deletions of mitochondrial DNA starting at the D-loop region. Nature, 339, 309-11.